Turbulent Intermittency in the Lagrangian-Averaged Alpha Model

by

Jonathan David Pietarila Graham

B.S. with honors, Oklahoma State University, 1993

A thesis submitted to the

Faculty of the Graduate School of the

University of Colorado in partial fulfillment

of the requirements for the degree of

Masters of Science

Department of Applied Mathematics

2005

This thesis entitled:
Turbulent Intermittency in the Lagrangian-Averaged Alpha Model
written by Jonathan David Pietarila Graham
has been approved for the Department of Applied Mathematics

Annick Pouquet

Keith Julien

Kamran Mohseni

Pablo Mininni

Date

The final copy of this thesis has been examined by the signatories, and we find that both the content and the form meet acceptable presentation standards of scholarly work in the above mentioned discipline.

Pietarila Graham, Jonathan David (M.S., Applied Mathematics)

Turbulent Intermittency in the Lagrangian-Averaged Alpha Model

Thesis directed by Affiliate Professor Annick Pouquet

The range of interacting scales encountered in fluid and magnetofluid flow problems of geophysical and astrophysical interest is well beyond expected computer resolutions in the next several decades. For this reason, closure schemes are employed to model in a computation the effect on the larger scales of those scales that are too small to be resolved. One such closure is called the "Lagrangian-averaged alpha model" or simply the "alpha model." The alpha model differs from large eddy simulations (LES) in that it preserves the invariants (under a different norm) of a given flow. Testing of this method, at least for non-conductive flows, has been extensive, but so far an evaluation of intermittency via high-order statistics has not been done because of lack of resolution.

The intermittent, or bursty, nature of turbulence is an enhancement of the likelihood of rare and extreme events. It is an essential feature of turbulence and it signifies a departure from self-similarity. Intermittency is typically measured as anomalous scaling of structure functions and these statistics require high resolution. For this reason, our simulations are carried out for two-dimensional magnetohydrodynamics (2D-MHD) which is known to have a direct energy cascade to small scales and to be intermittent (as is the three-dimensional (3D) case). As shown by previous tests [55] the alpha model accurately reproduces large-scale spectra, and, in the absence of forcing, time evolution of the energies and large-wavelength components of the field. We find that intermittency is reproduced by the alpha model as represented by the high-order structure functions (up to order 5 or 6). The results for velocity fields are found to be even more accurate than for magnetic fields and a proposal for improvement of the latter is made.

Dedication

To my wife.

Acknowledgements

First and foremost I would like to thank my mentor, Pablo Mininni. He has shown endless patience in his guidance of me through theory, through research, and through a few difficult revisions of this text. Without his efforts this work would not be. Secondly, I wish to thank my advisor, Annick Pouquet for her faith in me, for giving me this research position, and for reminding me to always question. I would also like to thank Keith Julien and Kamran Mohseni and, in fact, the entire committee for their time and efforts reading the manuscript, hearing my defense, and suffering through frequent, but necessary, reschedulings. I would also like to thank Karen Hawley for the arrangements of those frequent reschedulings.

On a more personal note I would like to thank my mother for encouraging me to go back to school and reminding me that in the long run this will be worth it. To my wife, Anna, thank you.

Computer time was provided by NCAR. The NSF grant CMG-0327888 at NCAR supported this work and is gratefully acknowledged.

Contents

Chapter

Tables

Table

Figures

Figure

Chapter 1

Introduction

> Equations are necessary if you are doing accountancy, but they are the boring part of mathematics. Most of the interesting ideas can be conveyed by words or pictures.
>
> -Stephen Hawking

When we are young, science is a very exciting thing for most of us. Just consider the science museums for children where you get to walk around and experience the wonder of nature first hand. This excitement often only lasts a little while. For many, probably because of algebra and calculus, it is over by high school. This certainly helps reduce job-market competition (and boost self esteem) for those who enjoy the compulsive allure of equations and keeping track of all those little terms. I for one, however, agree with Stephen Hawking that the ideas can be conveyed in other ways. What may be a very handy notation for some, may obscure otherwise accessible ideas for many. At times, the notation may even obscure the ideas for many who find the notation handy. If nothing else, it can certainly reduce public interest and, therefore, public funding. I set out writing this thesis with the lofty ambition of making it accessible to a slightly wider audience than usual. But, I found it unavoidable to do anything else than include loads of equations. Like Stephen Hawking, the reader is likely to agree that they are quite boring. I have settled on the attempt to describe the main ideas in ordinary English in a few introductory sections, and, where possible therein, to use words and pictures that make the equations redundant for understanding. The reader

will have to decide if I have succeeded.

1.1 Goals

In this thesis, we will motivate the need for closure schemes in computationally modeling turbulence in fluids (and magnetofluids). We will present one such closure scheme, the Lagrangian-averaged alpha model and test its ability to model turbulence at lower resolutions than for fully resolved direct numerical simulations. More specifically, we aim to test intermittency in the alpha model by studying high-order statistics.

1.2 Outline

In Chapter 2, we provide the necessary background in the modeling of fluids. We begin by motivating the need for closure schemes to model turbulent flows. We then consider a simplistic derivation of the Navier-Stokes equations to describe fluid flow. Next, we discuss the pseudospectral method for solving fluid-flow problems on a computer. In particular, we examine a simple one-dimensional (1D) toy model for compressible flow, Burgers equation, and its numerical solution. We conclude with a derivation of the magnetohydrodynamic (MHD) equations that describe the flow of a non-relativistic conducting liquid metal and approximate the large-scale flow for a plasma like the sun. In Chapter 3, we introduce the topics of turbulence theory addressed in this thesis. We discuss energy spectra and the dissipation length from a phenomenological or dimensional-analysis point of view. Then, we consider intermittency through somewhat everyday examples and make a heuristic connection to the structure functions. Finally, we present the Lagrangian-averaged alpha model (or, simply, the alpha model) and express the possibilities it presents to give some insight into the aforementioned problems. In Chapter 4, we present the two-dimensional magnetohydrodynamic (2D-MHD) equations and our motivation for studying them in the context of intermittency. We develop the ideal invariants of the flow, the direct cas-

cade of an invariant to small scales, and the inverse cascade of an invariant to large scales. We discuss the design of both our numerical code and our experiments. We also present the results of the Lagrangian-averaged magnetohydrodynamic alpha (LAMHD-α) model compared to direct numerical solutions (DNS) in regards to reproduction of large-wavelength component behavior. In Chapter 5, we discuss our techniques in determining the inertial ranges of our experiments and comparisons of intermittency in LAMHD$-\alpha$ versus DNS via high-order statistics (the structure functions). Finally, in Chapter 6, we summarize this work and make further concluding remarks.

Chapter 2

Fluids

Many things behave like a fluid: a liquid like water or molten lead, a gas like air or Helium, or a conductive fluid (*i.e.* any fluid that conducts electricity) like molten iron or plasma in the sun and in other astrophysical objects. With modern computation, many fluid flows can be accurately modeled. It can be difficult, when watching a contemporary movie, to tell if the water we see is a real photograph of surface waves or a computer-generated one. For engineering and science, computers have also led to many advances in the modeling and understanding of fluid motions. Yet, there are many problems of interest for which we would need computing speeds that will be unattainable for decades (or longer), or we would need new techniques. Such problems can arise in very fast flows or very large flows. By the latter, we could want to model, for instance, the atmosphere or oceans of the earth, the earth's liquid metal core, the sun, or even the interstellar medium. For these problems, we run into difficulties. While we can clearly make the scale of our model very large to encompass the grandest scales of interest, we find that it must also include the relatively quite small details to be an accurate model.

2.1 Non-Mathematical Description of the Direct Cascade

To illustrate this, let us begin by examining how large scale variations excite small scale fluctuations. Consider, for example, an imaginary one-dimensional flow of an idealized fluid. Picture this fluid as a compressible gas like air and that it is all

blowing from left to right. There is no motion in the up-down nor in the in-out of the paper directions. We concern ourselves with only one kilometer of the flow and observe the speed (velocity) of the fluid at each point (see Figure 2.1, panel **(a)**). Notice that for the speeds we have chosen (in fact it is one half-period of a sinusoid), fluid in the center starts out moving much faster than at either end. As we watch the flow, the part of the fluid in the middle will begin to catch up with those on the right end.[1] This changes our picture from one where the speed slowly rises and then slowly falls to one where the speed drops off at the end very rapidly (see Figure 2.1, panel **(b)**).

It is this effect that makes fluid flow so difficult to solve. Consider solving this flow on a computer. No computer has infinite memory, so we must choose to only keep track of the speed of the fluid at some limited number of points;[2] for instance, at the seven points we have marked with dotted lines in Figure 2.1, panels **(a)** and **(b)**. As time progresses, our steep drop in speed will occur completely between two adjacent points that we have chosen to watch (see Figure 2.1, panel **c**). Now our computer model is missing the velocity gradient, an essential detail of what is going on, and, in the end, is not a very good model of reality.[3] Naturally, we might then try adding even more points to our discrete model (this is called adaptive mesh refinement). These are the new dashed lines in Figure 2.1, panel **(c)**. This solves our immediate problem, but as time goes on the change in speed of the fluid becomes steeper and steeper until we would have to watch an infinite number of points to solve the problem. This is, of course, neither possible today with a computer nor with analytical math.[4]

[1] It would eventually catch up and even pass them. This, however, involves things like shocks which we will not consider here.

[2] This process is called discretization. Think of what happened to Jeff Bridges as he entered the computer in the movie Tron.

[3] Or our imaginary, idealized flow in this case.

[4] In reality, fluids have some viscosity (the property that makes molasses run slow) which acts against this piling up becoming too steep. And, in this simple example, there is only the one point where things pile up. Successively refining resolution just there is very effective on a computer (this problem also has an analytical solution). In a churning, turbulent fluid, however, there are many, many points with steep gradients in fluid properties (*e.g.* velocity–see, for instance, Figure 4.7) and we are interested in looking at more and more turbulent flows. This means, effectively, with smaller and smaller viscosities. In the end, the effect is the same. Computer resolution severely limits the problems of interest that we

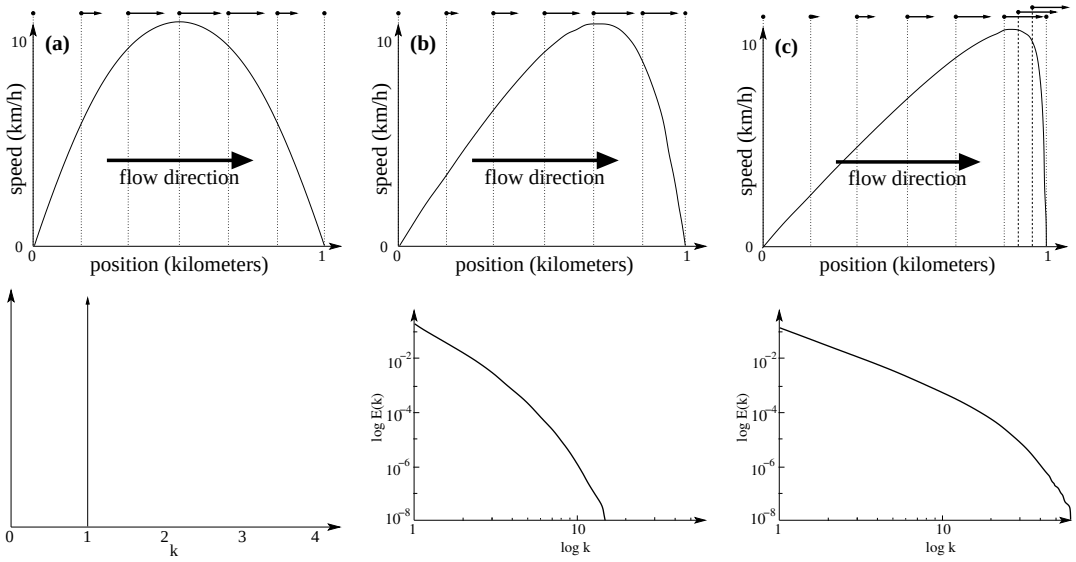

Figure 2.1: Imaginary one-dimensional flow of an idealized fluid. The flow is all left to right as indicated by the large flow direction arrow and the small flow speed arrows (atop) which indicate the 'wind' speed at selected positions. Panel **(a)** shows the situation at time, $t = 0$ seconds, panel **(b)** is at $t = 1.25$ minutes, and panel **(c)** is at $t = 2.5$ minutes. The second row depicts the energy spectra (or Fourier transforms) of the velocity profiles shown in the first row. In log-log are plotted energy versus wavenumber (inverse length).

To achieve the required resolution (evolve enough points) to model a typical atmospheric boundary layer[5] flow would require a one-hundred-million increase in computing power over today's largest computers [51]. If we assume that computer technology could continue its present rate of growth known as Moore's Law [61], that is, double every 18 months, it could take 40 years before such a computer exists! This is the central problem addressed in this thesis. Since we would rather not wait 40 years to answer our scientific questions, we would like very much to have some model that will recover some of the information of what is happening between the points. More importantly, we desire that the model will tell us what is happening at the points because of what occurs between the points. This would allow us to achieve a "closure" by evolving only the larger scales and modeling the effects of the smaller scales on them. The Lagrangian-averaged alpha model can be such a closure scheme. Of course, no model to date can tell us everything about what is happening between the points without us actually resolving it. If one could, turbulence would be a solved and understood phenomenon. So, what we will accomplish in this thesis is examine how good the alpha model is in modeling the statistics of what happens between the points.

2.2 Heuristic Description of the Direct Cascade

Burgers equation was introduced by Burgers [10] as a toy model for turbulence in 1D. We will not focus here on the similarities, and some big differences, between Burgers turbulence and Navier-Stokes turbulence. Instead, we use this comparatively simple equation as a good example of how simple advection (the movement of a fluid) causes the direct cascade of mechanical energy to smaller scales. The successive excitation of smaller and smaller scales is expressed through the advective term and the nature of its nonlinearity (see *e.g.* (2.1) or (2.7)). In one dimension this term is $u\partial_y u$ and is related

are able to model accurately.

[5] The atmospheric boundary layer is the part of the atmosphere in contact with the ground.

to the time derivative through the total derivative,

$$\frac{du}{dt} = \partial_t u + u\partial_y u = \mathcal{F}(u,t), \tag{2.1}$$

where $\mathcal{F}(u,t)$ represents all the density-normalized influences on the fluid flow. Taking $\mathcal{F}(u,t) = \nu\partial^2_{yy}u$ we have Burgers equation as the illustrative model of turbulence used in §2.1 (Figure 2.1),

$$\partial_t u + u\partial_y u = \nu\partial^2_{yy}u. \tag{2.2}$$

$u\partial_y u$ provides for coupling between spatial scales. Consider that we have for instance, $u(y,0) = \sin y$. Then $\partial_y u = \cos y$ and $u\partial_y u = \sin y \cos y = \frac{1}{2}\sin 2y$. On the next step, we will obtain more modes:

$$\sin 2y \cos y = \frac{1}{2}(\sin 3y + \sin y),$$
$$\sin 2y \cos 2y = \frac{1}{2}\sin 4y,$$

and

$$\sin y \cos 2y = \frac{1}{2}(\sin 3y - \sin y).$$

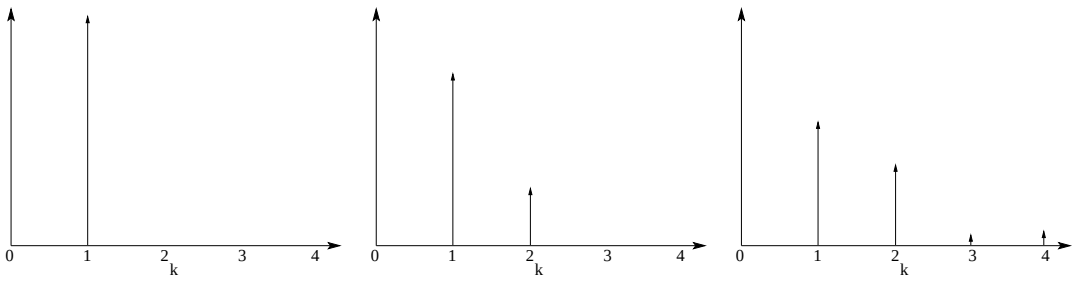

Figure 2.2: Cascade of energy to smaller scales. The vertical axis is arbitrary and not to scale. The horizontal axis is the wave-number, k ($k = 1$ corresponds to a wavelength $\lambda = 2\pi$, $k = 2$ to $\lambda = \pi$, $k = 4$ to $\lambda = \frac{\pi}{2}$, etc.). Time progress from left to right.

A spectral picture of this process (see Figure 2.2 or refer to Figure 2.1 for the cascade in our idealized example) illustrates the cascade of energy from large scales to smaller scales (see [77] and [62] for this process carried out further and in more

dimensions for the Navier-Stokes equation). This cascade will proceed to smaller and smaller scales without limit and excite an infinite number of Fourier modes.[6] It is this infinite amount of information that makes turbulent fluid flow problems difficult to solve. The large amount of information in the solutions also suggests a statistical approach to describe what can be known.

2.3 Navier-Stokes

Here, we present a heuristic derivation of the Navier-Stokes equations. To begin with, we make the continuum hypothesis that we are always able to choose a small enough volume so that the property we are measuring (*e.g.* average density, pressure, velocity) is local and independent of the number of particles in that volume (*i.e.* the volume contains a large number of particles) [3]. This assumption can be invalid for extremely low gas density or in a shock wave. Next, we consider a fluid element with one corner at the point (x, y, z) and volume, $\delta x \delta y \delta z = \delta V$ (see Figure 2.3). Newton's second law for the motion of this volume is

$$\boldsymbol{F} = m\boldsymbol{a} = m\frac{d\boldsymbol{u}}{dt}. \tag{2.3}$$

The forces are the fluid pressures on each of the faces times the area of each face,

$$\left(P_x(x) - P_x(x+\delta x)\right)\delta y\delta z + \left(P_y(y) - P_y(y+\delta y)\right)\delta x\delta z + \left(P_z(z) - P_z(z+\delta z)\right)\delta y\delta x = \rho\delta V\frac{d\boldsymbol{u}}{dt}, \tag{2.4}$$

where ρ is the average density of the fluid element. If we divide both sides by δV and take the limit $\lim_{\delta x,\delta y,\delta z\to 0}$ we find we have the definition of the derivative and

$$\rho\frac{d\boldsymbol{u}}{dt} = -\boldsymbol{\nabla}P. \tag{2.5}$$

Taking a dimensional analysis of (2.5), we find

$$\rho[L][T]^{-2} \sim P[L]^{-1},$$

[6] In a real system this infinite cascade would be stopped after reaching the dissipative scale discussed in §3.2. This could still be well outside the limits of modern computing.

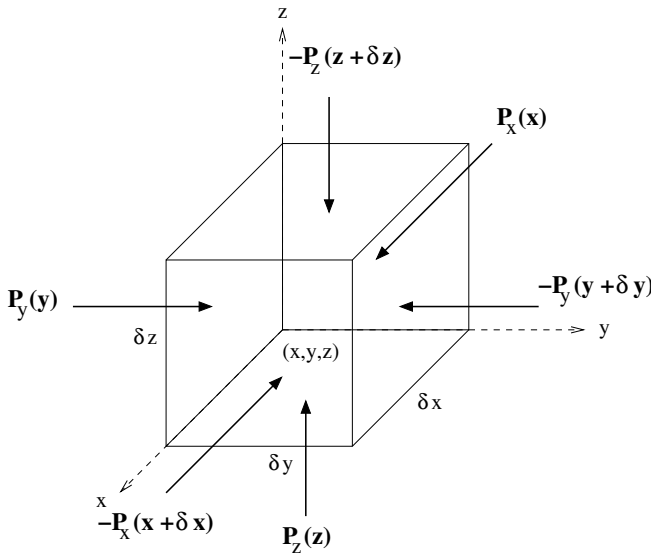

Figure 2.3: Fluid element at (x, y, z) with volume $\delta x \delta y \delta z = \delta V$. The bold arrows indicate pressures on the six faces with the following shorthand, $P_x(x) \equiv \int_y^{y+\delta y} dy' \int_z^{z+\delta z} dz' P(x, y', z')/\delta y \delta z$.

or

$$u^2 \sim \frac{\Delta P}{\Delta \rho}.$$

If we interpret this variation of pressure with density, $\Delta P/\Delta\rho$, as a derivative we have the sound speed squared, $\frac{\partial P}{\partial \rho} = C_S^2$ [63]. We see, then, that the condition for incompressibility, $\frac{\Delta\rho}{\rho} \ll 1$, is the same as requiring our velocities to be sub-sonic,

$$\frac{u^2}{C_S^2} \sim \frac{\Delta\rho}{\rho} \ll 1.$$

In other words, if the changes we are interested in propagate very much slower than pressure waves, the fluid will be able to adjust to the changes fast enough that it cannot be compressed, $\boldsymbol{\nabla}\cdot\boldsymbol{u} = 0$. Returning to (2.5) and dividing by the density and expanding the total derivative into its Eulerian components, we have Euler's equation,

$$\partial_t \boldsymbol{u} + \boldsymbol{u}\cdot\boldsymbol{\nabla}\boldsymbol{u} = -\boldsymbol{\nabla} p, \tag{2.6}$$

where $p \equiv P/\rho$. We assume the initial mass density to be constant and uniform. From the incompressibility condition and the continuity equation, then, we can infer the density to remain constant and uniform, and, therefore, normalize it out of our equations. With the addition of an arbitrary external force, $\mathcal{F}$, and a dissipative term, $\nu\nabla^2\boldsymbol{u}$, we arrive at the (incompressible) Navier-Stokes equations,

$$\begin{aligned} \partial_t \boldsymbol{u} + \boldsymbol{u}\cdot\boldsymbol{\nabla}\boldsymbol{u} &= -\boldsymbol{\nabla} p + \mathcal{F} + \nu\nabla^2\boldsymbol{u} \\ \boldsymbol{\nabla}\cdot\boldsymbol{u} &= 0. \end{aligned} \tag{2.7}$$

2.4 Pseudospectral Method

The main premise of the pseudospectral method is that it is computationally efficient and far more accurate to compute spatial derivatives in the Fourier domain. The pseudospectral approximate derivative can be understood as the limit of a finite difference approximation approaching infinite order. Thus, the pseudospectral approximation

approaches the true derivative exponentially as the grid spacing decreases. Considering the computational cost, the nonlinear advective term previously discussed in §2.2 is a multiplication of two vectors (in 1D), the velocity at all positions and the space derivative at all positions, and takes order N operations. N is the number of data points in our discretization. From the convolution theorem (see *e.g.* [12]), this multiplication becomes a convolution, the multiplication of a N by N matrix and a vector, in Fourier space and requires order N^2 operations. Through an algorithm known as the Fast Fourier Transform (FFT), the operation count to go between real (spatial) and Fourier (spectral) spaces is order $N \log N$. For very high resolution (large N) calculations, then, it is much cheaper to calculate the derivative in Fourier space and return to real space for the multiplication. This mixing of operations in both spaces is the reason for the 'pseudo'-spectral pseudonym. In two dimensions, we square the operation account advantage of 1D for pseudospectral and in three dimensions the advantage is cubed.

2.4.1 Example Application: Burgers Equation

We return to Burgers equation (2.2) for an illustrative example.

$$\partial_t u + u\partial_y u = \nu \partial_{yy}^2 u$$

Fourier transforms are commonly used in the analysis of partial differential equations [31]. The forward transform is taken to be[7]

$$\mathcal{F}[f(y)] \equiv \hat{f}(k) = \int_{-\infty}^{\infty} f(y) e^{-iky} dy, \tag{2.8}$$

and the inverse transform to be[8]

$$\mathcal{F}^{-1}[\hat{f}(k)] = \frac{1}{2\pi} \int_{-\infty}^{\infty} \hat{f}(k) e^{iky} dk. \tag{2.9}$$

[7] Other normalizations are possible.

[8] The Riemann-Lebesgue lemma guarantees that $F^{-1}[f(k)] = f(y)$ (except at discontinuities) if $f(y)$ has a finite number of discontinuities, is L_p integrable with $p \geq 1$, and is bounded. Dirichlet's theorem makes the same guarantee for $f(y)$ continuous, periodic, and bounded.

Expressing velocity, u, as a function of its transform, $\hat{u}$, we have

$$u(y) = \frac{1}{2\pi}\int_{-\infty}^{\infty} \hat{u}(k)e^{iky}dk. \tag{2.10}$$

From this, we can easily evaluate the spatial derivatives in Burgers equation.

$$\begin{aligned}\partial_y u &= \frac{i}{2\pi}\int_{-\infty}^{\infty} \hat{u}(k)ke^{iky}dk \\ \partial_{yy}^2 u &= \frac{-1}{2\pi}\int_{-\infty}^{\infty} \hat{u}(k)k^2e^{iky}dk\end{aligned} \tag{2.11}$$

Therefore, we require one FFT for $u \rightarrow \hat{u}$, two vector multiplications to find the transforms of the derivatives, and two FFTs to return to real space for multiplication of the nonlinear term and computation of the temporal derivative.

For computation, our problem is discretized, and we must consider the discrete Fourier transform[9] which is just an approximation to the Fourier series over the discretized domain $[1, N]$,

$$c_k = \frac{1}{N}\int_1^N f(x)e^{-ik\frac{2\pi}{N}x}dx \approx \frac{1}{N}\sum_1^N f(x)e^{-ik\frac{2\pi}{N}x}, \tag{2.12}$$

and

$$f(x) = \sum_{-\infty}^{\infty} c_k e^{ik\frac{2\pi}{N}x} \approx \sum_{-\frac{N}{2}}^{\frac{N}{2}} c_k e^{ik\frac{2\pi}{N}x} \approx \int_{-\frac{N}{2}}^{\frac{N}{2}} c(k)e^{ik\frac{2\pi}{N}x}dk. \tag{2.13}$$

Often, this last sum is rewritten using the fact that $e^{iN\frac{2\pi}{N}} = 1$. Defining, then, the c_k above $\frac{N}{2}$ to be the c_{k-N},

$$f(x) \approx \sum_1^N c_k e^{ik\frac{2\pi}{N}x}. \tag{2.14}$$

An important consequence of the discrete transform is aliasing. Aliasing is the corruption of the transform coefficients, c_k, for frequencies below the Nyquist frequency, $k = \frac{N}{2}$, by those above the Nyquist frequency. Aliasing is easily explained pictorially (see Figure 2.4). Here we can see that the Nyquist frequency is the highest frequency

[9] All implementations of the pseudospectral method employed in this work make use of the Fastest Fourier Transform in the West (FFTW) library [23].

we can unambiguously represent on our grid. Because of our limited sampling, we are unable to distinguish between a frequency k and a frequency $N-k$. We are guaranteed by the sampling theorem (see *e.g.* [9]) that our discretized representation contains all the information of the continuous function it represents if the continuous function has a Fourier transform that is zero above the Nyquist frequency. For a simulation starting from low frequency initial conditions, we might then zero all Fourier modes above the $N/2$ and be assured that our representation is complete. The nonlinear advection term transfers energy to higher modes, however, as discussed in §2.1 and §2.2. This would again introduce the aliasing problem as our modes just below $N/2$ would introduce energy beyond it. For this reason, the so-called two-thirds rule is often employed. That is, all modes above $k_{max} = N/3$ are zeroed.

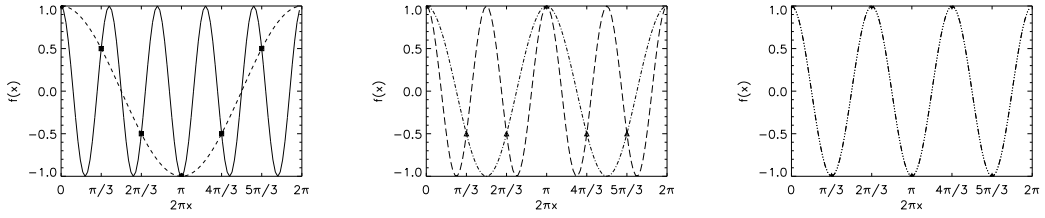

Figure 2.4: Example of aliasing for $N = 6$. Plots of $f(x) = \cos 2\pi kx$ for Left: $k = 1$ (dashed line) and $k = 5$ (solid line), Center: $k = 2$ (dash-dotted line) and $k = 4$ (long-dashed line), and Right: $k = 3$ (dash-triple-dotted line). The data is sampled at $N = 6$ points (0 and 2π are identical). Therefore, the Nyquist frequency is $N/2 = 3$ and this is the highest frequency mode captured by the grid (alternating ± 1 at sampled points). Higher frequency modes, $N - k$, are "aliased" onto lower frequency modes, k, because at the sampled points there is no way to distinguish between the two signals.

Parseval's relation (see §A.3) for the Fourier series is

$$< |f(x)|^2 >= \sum_{-\infty}^{\infty} |c_k|^2$$

$$\frac{1}{N}\int_1^N |f(x)|^2 dx = \sum_{-\infty}^{\infty} a_k^2 + b_k^2, \tag{2.15}$$

where we have defined $c_k = a_k + ib_k$. This is important for accurate dissipation of energy

(see §3.2). Using our finite summation we have

$$\frac{1}{N}\sum_{1}^{N}|f(x)|^2 \approx \sum_{-\frac{N}{2}}^{-1} a_k^2 + b_k^2 + a_0^2 + b_0^2 + \sum_{1}^{\frac{N}{2}} a_k^2 + b_k^2$$

$$\sum_{1}^{N}|f(x)|^2 \approx 2N\left(\frac{a_0^2}{2} + \frac{b_0^2}{2} + \sum_{1}^{\frac{N}{2}} a_k^2 + b_k^2\right) \tag{2.16}$$

where we have used $a_{-k} = a_k$ and $b_{-k} = -b_k$ for f real. The counting of grid points, $x \in [1, N]$, is the scale used by the FFT library. Our domain is $y \in [0, 2\pi]$ with periodic boundary condition, $y^{(p)}(0) = y^{(p)}(2\pi)\ \forall\ p \in \mathbb{N}$. Using $y = \frac{2\pi}{N}x$ and $dx = \frac{N}{2\pi}dy$,

$$c_k = \frac{N}{N2\pi}\int_1^N f(y)e^{-iky}dy = \frac{1}{2\pi}\hat{f}(k), \tag{2.17}$$

and

$$\int_{-\frac{N}{2}}^{\frac{N}{2}} c(k)e^{ik\frac{2\pi}{N}x}dk = \frac{1}{2\pi}\int_{-\frac{N}{2}}^{\frac{N}{2}} \hat{f}(k)e^{iky}dk \approx f(y). \tag{2.18}$$

Taking the derivative with respect to y of this last relation,

$$\partial_y f(y) \approx \frac{1}{2\pi}\int_{-\frac{N}{2}}^{\frac{N}{2}} ik\hat{f}(k)e^{iky}dk = \int_{-\frac{N}{2}}^{\frac{N}{2}} ikc(k)e^{ik\frac{2\pi}{N}x}dk \approx \sum_{-\frac{N}{2}}^{\frac{N}{2}} ikc(k)e^{ik\frac{2\pi}{N}x}dk. \tag{2.19}$$

Taking the derivative is a simple multiplication by ik in Fourier space followed by the inverse transform, just as it was for the continuous transforms.

Testing the FFTW library in double precision for $N = 128$ on a few simple sine waves ($k = 1$ to $k = 64$) gave derivatives with an accuracy of 10^{-4} to 10^{-7} depending on how well resolved the signal was, forward followed by inverse transforms with an accuracy of 10^{-16}, and Parseval's relations with an accuracy of 10^{-15} to 10^{-17}.

2.5 The Magnetohydrodynamic (MHD) Approximation

Electrically-conductive fluid flows occur commonly in nature. Some examples are the fluid motion in the earth's core which maintains the earth's magnetic field, the sun's convective zone and corona, the solar wind, the earth's magnetosphere and upper ionosphere, the interstellar medium, and numerous other astrophysical phenomena.

We present here a heuristic derivation of the simple, incompressible, one-fluid MHD equations (see *e.g.* [63]). We begin with the Navier-Stokes equations (2.7) and, therefore, with the continuum hypothesis, the incompressibility assumption, and a constant uniform density. Note that we have assumed there to be essentially one fluid, though for a plasma there could arise situations where the "positively-charged fluid" and the "negatively-charged fluid" should be considered separately. To the Navier-Stokes equations we add a Lorenz forcing term and Maxwell's equations. Additionally, we assume there is no creation or loss of particles and no pair productions or recombinations. We assume that the flow is non-relativistic, $\frac{u}{c} \ll 1$, and that, therefore, there will be no Maxwell displacement current and no charge separation (and hence no net forces from electric fields). Finally, we assume the fluid has a constant conductivity. We consider Maxwell's equations.[10] Ampere's law,

$$\boldsymbol{\nabla} \times \boldsymbol{b} = \mu \boldsymbol{j} + \frac{1}{c^2} \partial_t \boldsymbol{E}, \tag{2.20}$$

states that a current, $\boldsymbol{j}$, or the time rate of change of the electric field, $\boldsymbol{E}$, produces a curl in the magnetic field, $\boldsymbol{b}$, and vice-versa. The speed of light is c and μ is the permitivity. The term, $\frac{1}{c^2} \partial_t \boldsymbol{E}$, is called the Maxwell displacement current and can be neglected in the non-relativistic limit. Faraday's law is

$$\boldsymbol{\nabla} \times \boldsymbol{E} = -\partial_t \boldsymbol{b}, \tag{2.21}$$

that the time rate of change of the magnetic field produces a curl in the electric field and vice-versa. Ohm's law is

$$\boldsymbol{j} = \sigma \left(\boldsymbol{E} + \boldsymbol{u} \times \boldsymbol{b} \right), \tag{2.22}$$

that the current is proportional to the electric field and the curl of fluid velocity and the magnetic field by the conductivity, σ, which we assume to be constant. Combining Ohm's law with Ampere's law, minus the Maxwell displacement current, we find

$$\boldsymbol{\nabla} \times \boldsymbol{b} = \sigma \mu \left(\boldsymbol{E} + \boldsymbol{u} \times \boldsymbol{b} \right). \tag{2.23}$$

[10] We employ Alfvénic units (*i.e. the magnetic field is expressed in units of velocity).*

Applying a curl and using the absence of magnetic monopoles ($\boldsymbol{\nabla} \cdot \boldsymbol{b} = 0$), we derive

$$\boldsymbol{\nabla} \times \boldsymbol{\nabla} \times \boldsymbol{b} = -\boldsymbol{\nabla}^2 \boldsymbol{b} = \sigma\mu \left(\boldsymbol{\nabla} \times \boldsymbol{E} + \boldsymbol{\nabla} \times (\boldsymbol{u} \times \boldsymbol{b}) \right). \tag{2.24}$$

Finally, upon insertion of Faraday's law (2.21), we derive the induction equation

$$\partial_t \boldsymbol{b} = \boldsymbol{\nabla} \times (\boldsymbol{u} \times \boldsymbol{b}) + \eta \boldsymbol{\nabla}^2 \boldsymbol{b} \tag{2.25}$$

where we have defined the diffusivity from the permitivity and the conductivity, $\eta = \frac{1}{\mu\sigma}$. The Lorenz force is

$$\mathcal{F} = \boldsymbol{j} \times \boldsymbol{b}. \tag{2.26}$$

Upon combining Navier-Stokes (2.7), the induction equation (2.25), and the Lorenz force (2.26), we arrive at the MHD equations

$$\partial_t \boldsymbol{u} + \boldsymbol{u} \cdot \boldsymbol{\nabla} \boldsymbol{u} = -\boldsymbol{\nabla} p + \boldsymbol{j} \times \boldsymbol{b} + \nu \nabla^2 \boldsymbol{u} + \mathcal{F}_K \tag{2.27a}$$

$$\boldsymbol{\nabla} \cdot \boldsymbol{u} = 0 \tag{2.27b}$$

$$\boldsymbol{\nabla} \cdot \boldsymbol{b} = 0 \tag{2.27c}$$

$$\partial_t \boldsymbol{b} = \boldsymbol{\nabla} \times (\boldsymbol{u} \times \boldsymbol{b}) + \eta \boldsymbol{\nabla}^2 \boldsymbol{b} + \mathcal{F}_M, \tag{2.27d}$$

where $\mathcal{F}_K$ and $\mathcal{F}_M$ are external forces we may wish to apply.

Chapter 3

An Approach to Turbulence Theory

Big whorls have little whorls that feed on their velocity, and little whorls have lesser whorls, and so on to viscosity.[1]
-Lewis Fry Richardson [71]

3.1 What is Turbulence?

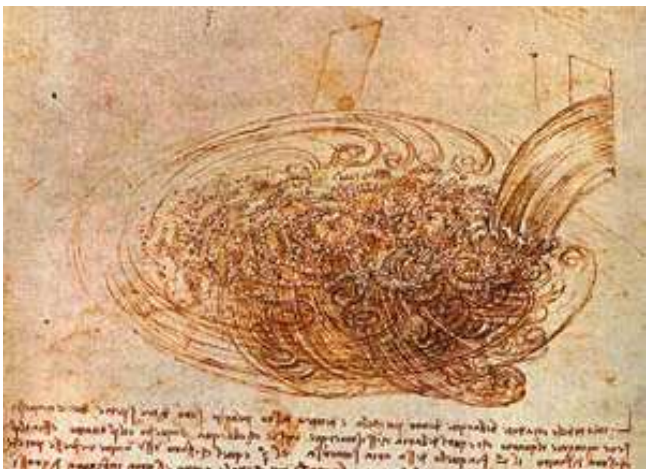

Figure 3.1: Leonardo da Vinci's illustration of the swirling flow of turbulence. (The Royal Collection ©2004, Her Majesty Queen Elizabeth II.) Taken from `http://www.maths.monash.edu.au/~jjm/jjmsph.shtml`.

Turbulence is the wake of a speedboat, water from a fire hose, boiling water, and, yes, that which shakes your airplane ride about.

[1] A poetic adaptation of "So, the nat'ralists observe, a flea \ hath smaller fleas that on him prey; And these have smaller yet to bite 'em, And so proceed *ad infinitum*. Thus every poet, in his kind \ Is bit by him that comes behind." by Jonathan Swift, Poetry a Rhapsody.

> Strong fluid turbulence [...] can be defined as a solution of the Navier-Stokes equations whose statistics exhibit spatial and temporal fluctuations.[20]

That is, turbulence is typified by large velocity differences and not, necessarily, by large velocities (see Figure 3.1). And the challenge, as we alluded to in the previous chapter is that these fluctuations occur over a large range of coupled spatial and temporal scales. That is, what happens over great distances influences what happens between very small elements and vice versa. For this reason, a detailed understanding from first principles still eludes turbulence theory.

3.2 Kolmogorov 41 Phenomenology

In 1941, Andrei Nikolævich Kolmogorov [46, 47, 48] fathered modern turbulence theory. He made a few essential assumptions and predictions that are still used today as a measuring stick for contemporary models and simulations.[24] These four assumptions, or hypotheses, are homogeneity, isotropy, self-similarity, and universality. Turbulence is homogeneous if, at least for the small scales, the statistical properties of the fluid flow are invariant under space-translations (the same at any point in the fluid).[2] Turbulence is isotropic if, at least for the small scales, the statistical properties of the fluid flow are invariant under rotations (independent of which direction we are looking). Universality applies to turbulence if, at least for the small scales,[3] there are quantifiable statistical properties common to all turbulent flows regardless of the type of flow, the fluid that is flowing, the boundary conditions, or the energy-input mechanisms (stiring, shaking, or shearing) [51]. Self-similarity, simply stated, is the idea that any small portion of the flow looks essentially the same as the larger flow if it is blown up to the same size. His results can also be derived from an approach by Robert Kraichnan (1967) that is described by the term "phenomenology" and at times seems to be nothing more than dimensional analysis. But, it has met with considerable success in both experimental

[2] This is the same word as for "homogenized" milk.
[3] Or, rather, for some range of scales.

and numerical verification. We will examine some of the results in simplified form here. The time rate of change of the energy in a fluid flow is given by the dissipation equation, we have

$$\frac{dE}{dt} = -2\nu\Omega, \tag{3.1}$$

in the absence of forcing (see §A.2 for a derivation of Burgers dissipation). Here, $E \equiv \int \frac{1}{2}u^2 dV$ represents the energy (per unit mass) integrated over the entire domain, ν is the kinematic viscosity, and $2\nu\Omega = 2\nu \int \frac{1}{2}(\boldsymbol{\nabla}\times\boldsymbol{u})^2 dV$ is called the enstrophy. Enstrophy is the dissipation into heat due to internal fluid friction. In the presence of forcing, we denote the energy injection rate by the forcing as ε. Then, for steady state we require

$$\frac{dE}{dt} = \varepsilon - 2\nu\Omega \approx 0 \tag{3.2}$$

or

$$\varepsilon \approx -2\nu\Omega. \tag{3.3}$$

From here we employ dimensional analysis or phenomenology as it is called.

Burgers Equation

We return again to Burgers equation, (2.2), for an illustrative example,

$$\partial_t u + u\partial_y u = \nu\partial^2_{yy} u.$$

The dimensional analysis for this equation is

$$[T]^{-1}[L][T]^{-1} + [L][T]^{-1}[T]^{-1} \sim \nu[L]^{-1}[T]^{-1}$$

which tells us the dimensions for the viscosity, ν, are $[L]^2[T]^{-1}$ as expected. Now, if we use Parseval's theorem (A.35), $\int_{-\infty}^{\infty} f^2 dx = \frac{1}{\pi}\int_0^{\infty} \hat{f}^*\hat{f} dk$ for E, we will have

$$E = \int_{-\infty}^{\infty} \frac{1}{2}u^2 dy = \int_0^{\infty} \frac{1}{2\pi}\hat{u}^*\hat{u} dk = \int_0^{\infty} E(k) dk. \tag{3.4}$$

where we have reasonably defined the spectral energy density, $E(k) \equiv \frac{1}{2\pi}\hat{u}^*\hat{u}$. Here we have used the notation * for complex conjugation and $\hat{u}$ for the Fourier transform[4] of

[4] Introduced in §2.4.

u. Using (2.8)

$$\mathcal{F}[u(y)] \equiv \hat{u}(k) = \int_{-\infty}^{\infty} u(y)e^{-iky}dy$$

we can find the dimensions of $\hat{u}$.

$$\hat{u} \sim [L][T]^{-1}[L] \tag{3.5}$$

From this, we can see the dimensions of spectral energy density, $E(k)$, are $[L]^4[T]^{-2}$.

Parseval's theorem for the enstrophy is

$$\Omega = \int_{-\infty}^{\infty} \frac{1}{2}(\partial y u)^2 dy = \int_0^{\infty} \frac{1}{2\pi}\mathcal{F}[\partial_y u]^* F[\partial_y u]dk. \tag{3.6}$$

Evaluating the Fourier transform using integration by parts,

$$\mathcal{F}[\partial_y u] \equiv \int_{-\infty}^{\infty} \partial_y u e^{-iky}dy = ue^{-iky}|_{-\infty}^{\infty} + ik\int_{-\infty}^{\infty} ue^{-iky}dy = ik\hat{u}. \tag{3.7}$$

Using either periodic boundary conditions or requiring the velocity to vanish at infinity will eliminate the first term leaving us with $\mathcal{F}[\partial_y u] = ik\hat{u}$ which has dimensions $[L][T]^{-1}$. Now we can write the enstrophy as a function of the spectral energy density.

$$\Omega = -\int_0^{\infty} k^2 E(k)dk \tag{3.8}$$

Returning to the balance between the energy injection and dissipation rates (3.3),

$$\varepsilon \approx -2\nu\Omega,$$

from which dimensional analysis gives us

$$\varepsilon \sim [L]^3[T]^{-3}.$$

Energy is assumed to be injected only into the larger, integral scales and dissipated only at the much smaller, dissipative scales for very high Reynolds number (*i.e.* very small ν).[5] See Figure 3.2. The dissipation term in Burgers equation, $\nu\partial_{yy}^2 u$, will go

[5] The ratio of the nonlinear term to the viscous dissipation term is a good measure of the strength of the turbulence. This ratio is called the Reynolds number, Re. For Burgers we can easily see $\frac{u\partial_y u}{\nu\partial_{yy}^2 u} \sim \frac{u\cdot u/D}{\nu\cdot u/D^2} = \frac{uD}{\nu} \equiv Re$ where u and D are some typical velocity and length, respectively.

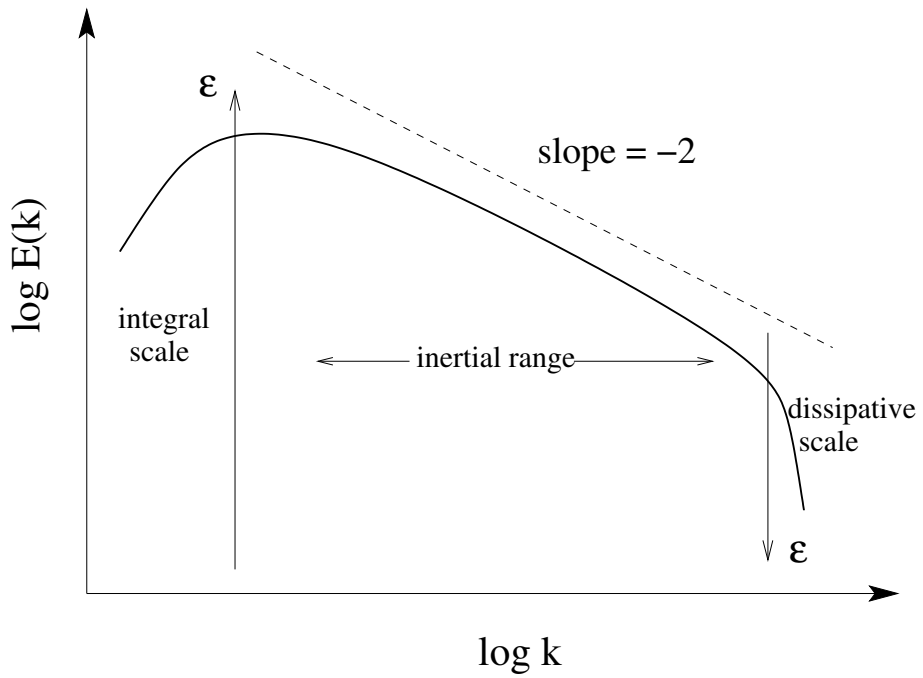

Figure 3.2: Log-log plot of energy density spectrum showing energy injection, ε, at the integral scale, energy dissipation, ε, at the dissipative scale, and inertial range with a k^{-2} spectrum corresponding to Burgers equation.

as $\nu k^2 \hat{u}$ in Fourier space. Therefore for very small viscosity, dissipation only becomes significant at very large wavenumbers (very small lengths). If the Reynolds number is high enough, there will be many orders of magnitude (decades) in wavenumber between the energy injection scales and the energy dissipation scales. This range is called the inertial range. In the inertial range energy is assumed, by the argument just given, to be transferred from larger scales to smaller scales without loss and thus with a constant rate ε. This is the assumption of universality.[6] From this reasoning, the spectral energy density in the inertial range must be independent of the viscosity, ν. It can only depend on the energy injection rate, ε, and the wavenumber, k,

$$E(k) \sim \varepsilon^{\beta} k^{\gamma}. \tag{3.9}$$

This relation (called a power law) will, then, be derived from dimensional analysis,

$$[L]^4 [T]^{-2} \sim [L]^{3\beta} [T]^{-3\beta} [L]^{-\gamma}.$$

And, finally, we have

$$E(k) \sim \varepsilon^{\frac{2}{3}} k^{-2}. \tag{3.10}$$

This analysis can also be used to calculate the Kolmogorov dissipation length. The Kolmogorov dissipation length, l_ν, is the length scale below which there is no energy contained in the system. Combining enstrophy as a function of the spectral energy density (3.8) and the balance between the energy injection and dissipation rates (3.3), we find

$$-\frac{\varepsilon}{2\nu} \approx \Omega \approx -\int_0^{k_\nu} k^2 E(k) dk. \tag{3.11}$$

Here the Kolmogorov dissipation wavenumber, k_ν, is chosen so that practically all of

[6] Actually, universality can be stated [24] as the assumption that "in the limit of infinite Reynolds number, all the small-scale statistical properties are uniquely and universally determined by the scale l and the mean energy dissipation rate ε."

the enstrophy is accounted for. Upon integration, we find

$$\frac{\varepsilon}{2\nu} \approx \varepsilon^{\frac{2}{3}} k_\nu$$
$$\frac{\varepsilon^{\frac{1}{3}}}{2\nu} \approx k_\nu,$$

or that $l_\nu \sim 2\nu$. That is, if a simulation is at its resolution limit and we halve the viscosity, we must also halve our length scales (double our linear resolution).[7] This defines the term "well resolved" for pseudospectral methods. When $k_\nu < k_{max}$, all the injected energy is dissipated at small scales by the viscous term.

Navier-Stokes Equations

The Navier-Stokes equations, (2.7), are

$$\partial_t \boldsymbol{u} + \boldsymbol{u} \cdot \boldsymbol{\nabla} \boldsymbol{u} = -\boldsymbol{\nabla} p + \nu \nabla^2 \boldsymbol{u}$$

$$\boldsymbol{\nabla} \cdot \boldsymbol{u} = 0.$$

For (2.7), the spectral energy density dimensional analysis relation is found to be

$$E(k) \sim \varepsilon^{\frac{2}{3}} k^{-\frac{5}{3}}. \tag{3.12}$$

Using the relation between energy density and the energy injection rate (3.11), we find that

$$\frac{\varepsilon}{2\nu} \approx \int_0^{k_\nu} k^2 E(k) dk = \varepsilon^{\frac{2}{3}} \int_0^{k_\nu} k^{\frac{1}{3}} dk = \frac{3}{4} \varepsilon^{\frac{2}{3}} k_\nu^{\frac{4}{3}} \tag{3.13}$$

and $k_\nu^{\frac{4}{3}} \sim \frac{\varepsilon^{\frac{1}{3}}}{\nu}$ which yields

$$k_\nu \sim \left(\frac{\varepsilon}{\nu^3}\right)^{\frac{1}{4}}. \tag{3.14}$$

That is, if a simulation is at it's resolution limit and we halve the viscosity, we must increase our resolution by a factor of $8^{\frac{1}{4}}$. For a linear resolution, N, the computational cost will be proportional to N^3 for 2D simulations and N^4 for 3D. From this we can see that if we wish to double our Reynolds number we quadruple and octuple our computer time for 2D and 3D, respectively.

[7] The total resolution will grow as the number of dimensions

This can be related to the continuum hypothesis from §2.3. If all the energy containing scales are larger than l_ν, and l_ν^3 contains a very large number of individual particles, then scales small enough for the continuum hypothesis to be invalid have no influence on the dynamics of the fluid.

3.3 Intermittency and Structure Functions

3.3.1 Description

Something is intermittent if it has short bursts separated by relatively sedate periods. This is temporal intermittency (being intermittent in time). Spatial intermittency (being intermittent in position) displays isolated regions of fluctuations separated by relatively unchanging regions. Intermittency in time is the more often experienced of the two. Consider the intermittent problem with your car that is never there when the mechanic looks at it, or the intermittency of natural phenomena like earthquakes and solar flares. They happen at irregular intervals that are difficult to predict but are extremely energetic when they do occur. Using the example of turbulent boiling water, the times at which the water boils over and out of the pan are temporally intermittent. On the other hand, the position of all the bubbles in the boiling water is spatially intermittent. For turbulence, intermittency is "associated with [its] violent, atypical discontinuous nature" [20]. It is both spatially and temporally intermittent. In Figure 3.3, we illustrate temporal intermittency by comparing a regular, periodic signal (not intermittent), an earthquake seismogram[8] (intermittent), a random signal (not intermittent), and a chaotic signal[9] (not intermittent). Randomness can be thought of as the simple process of rolling a die or picking a card from a shuffled deck.[10] A defi-

[8] Data is from 9 September 2001, 16:59:16 PDT, at Hollywood Boulevard and Hillhurst, Los Angeles (CGS Station No. 24982) obtained from the California Integrated Seismic Network. `http://www.quake.ca.gov/cisn-edc/search/24982.HTM`

[9] Data is from the quadratic map, $x_{t+1} = x_t^2 - 1.5$ (see for instance [73]).

[10] These are examples of an even random distribution. Other distributions, such as Gaussian, are possible as well.

nition of chaos is a little harder to pin down. A chaotic system is a deterministic one. If the value of all the variables of a system is known with infinite precision, all futures values can be predicted. Chaos, however, exhibits sensitivity to initial conditions. A small error in one of the variables grows exponentially in time (see *e.g.* [2]). These same signals can be used to generate examples of spatial intermittency as seen in Figure 3.4. From these pictures we can see why intermittency is sometimes described as the degree of spottiness. Extreme events are more likely than for a random, or Gaussian process. These events will stand out as "spots" in a 2D visualization.

We would like to have some measure of the amount of burstiness in a given data set. One such measure is the structure function. It measures the burstiness of a signal by the deflection of its structure-function plot from a straight line. In other words, it measures the statistics of violent events as higher order (smaller scales) are considered. Any deviation from a straight line indicates complex behavior of the system with the scale, or departures from self-similarity. In Figure 3.5 we can see both how intermittency is a violation of the assumption of self-similarity and how the structure functions measure it. Here we have cut out a small portion of the earthquake signal and and blown it up. The result does not look at all similar to the original signal, and, hence, we can see that the signal is not self-similar. The structure functions are formed by looking at the difference in the signal at two separate times. Consider, for instance, the two times indicated and marked τ_1 in the figure. Such a stencil is moved along the signal and an average is made over the entire signal. This is the structure function of order one. Different stencil lengths are employed, such as τ_2 in the figure. For a length longer than the typical burst length (*e.g.* τ_1), such a stencil will pick up at most half the amplitude of the burst, $A/2$. For a length shorter than the burst length (*e.g.* τ_2), the stencil could pick up the full amplitude, A. Now the higher-order structure functions are made by raising the stencil differences to higher powers before averaging. Whereas, for our first-order structure function, we had a factor of two

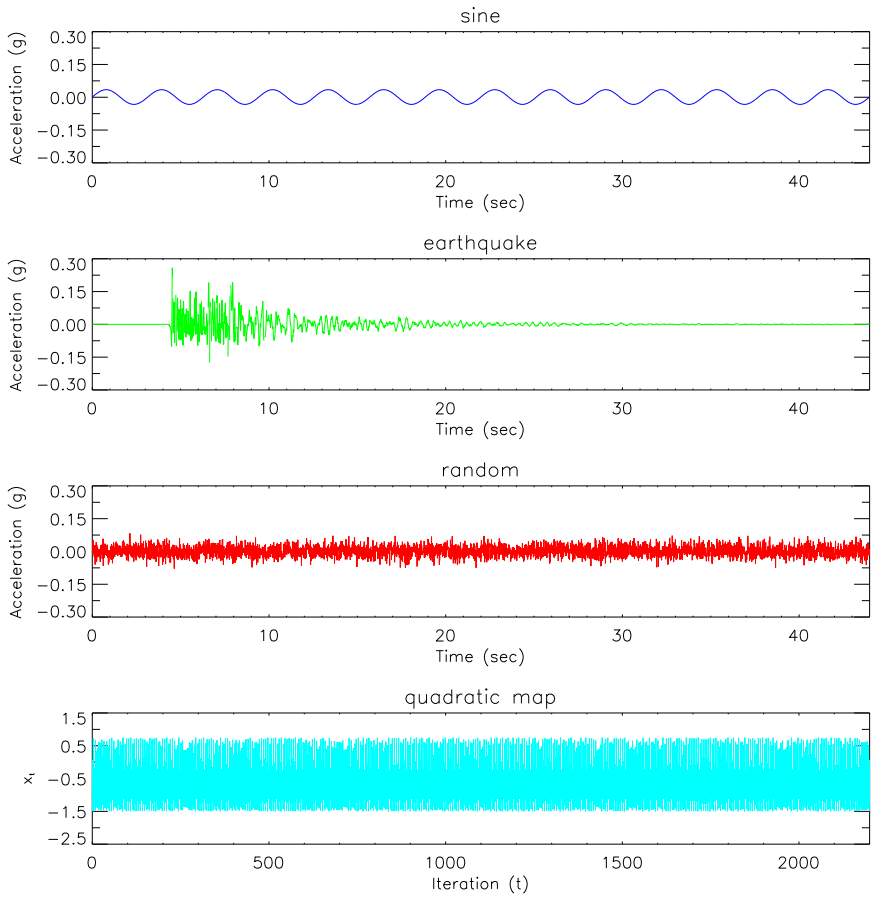

Figure 3.3: Example of temporal intermittency. The top frame (blue line) is a regular, periodic, and in this case sinusoidal signal (not intermittent). The upper-middle frame (green line) is an earthquake seismogram in units of g (intermittent). The lower-middle frame (red line) is a random signal (not intermittent). The bottom frame (cyan line) is a chaotic signal (not intermittent).

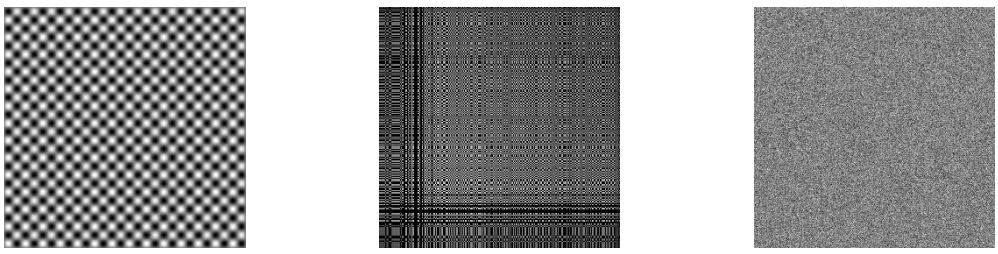

Figure 3.4: Example of spatial intermittency. The leftmost image is completely regular (not intermittent), the middle image is intermittent, and the rightmost image is completely random (not intermittent).

difference depending on τ, for the second-order structure function we square our terms for a factor of four. For the third-order we have a factor of eight, and so on. As the powers, p, become larger the effect becomes more nonlinear as can bee seen in Figure 3.6

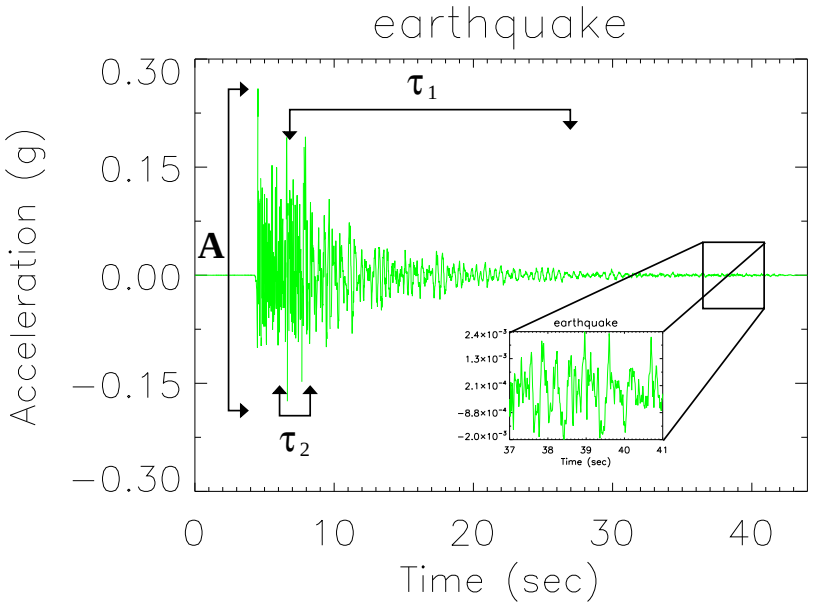

Figure 3.5: Intermittency as a violation of the self-similarity hypothesis.

which is a structure-function plot for the four data sets depicted in Figure 3.3. Notice that the non-intermittent data sets lie along straight lines while the intermittent data set curves below an imaginary straight line. This last curve will be seen to be similar to curves for intermittent turbulence we will see later. Intermittency is an essential part of turbulence, and we would like for any model we use of turbulence to reproduce it. These structure functions will be the tools we use to test for it.

3.3.2 Mathematics

In the late nineteenth century Osborne Reynolds brought about the introduction of statistics and probability to turbulence theory by regarding the flow as a superposition of mean and fluctuating parts. Modern analysis discovers the generic properties of

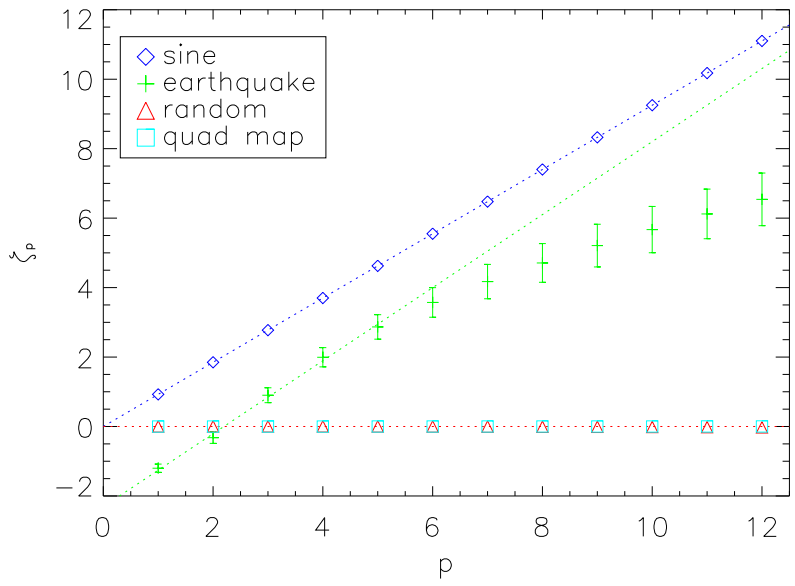

Figure 3.6: Scaling of structure functions: ζ_p versus p for a regular, periodic signal (sine wave) as blue diamonds, for an earthquake signal as green pluses, for a random signal as red triangles, and for a chaotic signal as cyan squares. Error bars are shown only for the earthquake signal as the errors for the other signals are very small. The dotted lines are present only to highlight the earthquake's deviation from a straight line.

turbulence in the statistics of the velocity increment [20]. We can see how these statistics measure intermittency by considering a time series. The typical scale-dependent quantities constructed from the increments are known as structure functions. The structure function of a time series f is defined as $S_p^f(\tau) \equiv \langle |\delta f(\tau)|^p \rangle$[11] where $\delta f(\tau) = f(t+\tau) - f(t)$ is the increment of f. The assumption of self-similarity can be written mathematically as

$$\delta f(\lambda T) = \lambda^h \delta f(T), \tag{3.15}$$

where h is some scaling exponent [24]. Defining $\tau = \lambda T$, we find

$$S_p^f(\tau) = \langle |\lambda^h \delta f(T)|^p \rangle = \lambda^{h \cdot p} \langle |\delta f(T)|^p \rangle \sim \tau^{\zeta_p^f}, \tag{3.16}$$

where $\zeta_p^f = h \cdot p$ are the scaling exponents of the structure functions. If the statistical features of the system are independent of spatial scale, it is described as self-similar and it's scaling will be linear, $\zeta_p^f \sim p$.

Frisch [24] gives a precise definition of an intermittent function. "It displays activity during only a fraction of the time, which decreases with the scale under consideration". He goes on to define the flatness,

$$F(\omega) \equiv \frac{\langle (f_\omega^>(t))^4 \rangle}{\langle (f_\omega^>(t))^2 \rangle^2}, \tag{3.17}$$

of a time series f where $f_\omega^>(t)$ has been high-bandpass filtered with frequency ω. If this quantity grows without bound as ω increases, f is said to be intermittent.[12] To justify this choice, Frisch considers a signal f that is derived by being zero most of the time with short intervals copied from a random signal v for a fraction γ of the time. Then, $\langle f^p \rangle = \gamma \langle v^p \rangle$ and $F(\omega) = \frac{1}{\gamma} \cdot \frac{\langle (v_\omega^>(t))^4 \rangle}{\langle (v_\omega^>(t))^2 \rangle^2}$. Heuristically speaking, as the high-bandpass frequency is increased, there will be less and less of v left non-zero effectively decreasing γ and F will grow. Extending this idea, he defines a hyper-flatness,

$$F_p(\tau) \equiv \frac{S_p(\tau)}{(S_2(\tau))^{p/2}}, \tag{3.18}$$

[11] Angle brackets, $\langle \cdot \rangle$, denote integration over the entire domain.
[12] In practice, the "filtered" flatness will decrease again after reaching the dissipation scale.

from the structure functions. If this hyper-flatness grows without bound as $\tau \to 0$, the signal is intermittent. In other words, for intermittency, the statistics of velocity increments become extremely non-Gaussian as the scale decreases. If the structure functions have scaling exponents, we find

$$F_p(\tau) \sim \tau^{\zeta_p^f - \zeta_2^f \cdot \frac{p}{2}}. \tag{3.19}$$

Under the assumption of self-similarity, $\zeta_p^f \sim p$ and we find $F_p(\tau) \sim \tau^{p-2\cdot\frac{p}{2}} = 1$ and the hyper-flatness does not grow as $\tau \to 0$. If, however, $\zeta_p^f < \zeta_2^f \cdot \frac{p}{2}$ then the graph of ζ_p^f versus p will lie below the line of $\zeta_2^f \cdot \frac{p}{2}$, $F_p(\tau)$ will grow without bound as $\tau \to 0$, and the signal will be intermittent (by definition) as in Figure 3.6.

For instance, for the sine function, the increment takes the form

$$\delta \sin(\lambda T) = \sin(t + \lambda T) - \sin(t) = 2\sin(\frac{\lambda T}{2})\cos\left(t + \frac{\lambda T}{2}\right).$$

In the limit as $\lambda T \equiv \tau \to 0$, we have

$$\delta \sin(\lambda T) \approx \lambda T \cos(t) = \lambda^1 \delta \sin(T).$$

Then in the asymptotic limit sine is self-similar and not intermittent. This is shown in Figure 3.6. For a completely random signal, $\delta f(\tau)$ will also be a random quantity with no τ-dependence and S_p^{rand} will be constant. We should expect $\zeta_p^{rand} = 0$ as we do indeed see in Figure 3.6. When there are isolated small patches of rapid fluctuations (intermittency), we expect $\langle |\delta f(\tau)|^p \rangle$ to be enhanced for τ smaller than the typical patch length and the more so the greater the value of p. It is this enhancement at smaller τ that leads to smaller ζ_p for higher order, p.

3.3.3 von Kármán-Howarth Theorem

From the von Kármán-Howarth equation Kolmogorov [46] derives the four-fifths law,

$$\langle (\delta u_L(l))^3 \rangle = -\frac{4}{5}\varepsilon l, \tag{3.20}$$

for the third-order longitudinal structure function of the velocity ($\delta u_L(l) = (\boldsymbol{u}(\boldsymbol{x}+\boldsymbol{l}) - \boldsymbol{u}(\boldsymbol{x})) \cdot \boldsymbol{l}/l$), the energy dissipation rate ε, and length l in the inertial range. This is one of the few "exact" results for turbulence. It is beyond the scope of this work to derive this result, the result for MHD, or the result for the Lagrangian-averaged alpha model (the alpha model is presented in the following section). Instead, we will develop the so-called twelfth law for Burgers equation (2.2),

$$\partial_t u + u\partial_y u = \nu \partial^2_{yy} u.$$

We define an independent point $y^{'}$ and denote $u^{'} = u(y^{'}, t)$. Following [46] we momentarily neglect the energy dissipation. Multiplying Burgers equation by $u^{'}$ from the left, we obtain

$$u^{'}\partial_t u = -\frac{1}{2}\partial_y (u^2 u^{'}), \tag{3.21}$$

where we have made use of the fact that $u^{'}$ is independent of y. Denoting $\partial^{'} = \frac{\partial}{\partial y^{'}}$, we find similarly

$$u\partial_t u^{'} = -\frac{1}{2}\partial^{'}(u u^{'2}). \tag{3.22}$$

Defining $l = y^{'} - y$, we have $\partial_l = \partial^{'} = -\partial_y$ and

$$2\partial_t (u u^{'}) = -\partial_l (u u^{'2} - u^2 u^{'}). \tag{3.23}$$

Letting angle brackets denote averaging over space we have a relation for the time evolution of the two-point correlation function for velocity

$$2\partial_t \langle u u^{'} \rangle = -\partial_l \langle u u^{'2} - u^2 u^{'} \rangle. \tag{3.24}$$

In our notation, the increment of the velocity becomes $\delta u(l) = u^{'} - u$. Assuming homogeneity, we find

$$\langle \delta u^2 \rangle = 2\langle u^2 \rangle - 2\langle u u^{'} \rangle, \tag{3.25}$$

and

$$\langle \delta u^3 \rangle = -3\langle u u^{'2} - u^2 u^{'} \rangle. \tag{3.26}$$

Substituting (3.24) into (3.26) we find

$$\langle \delta u^3 \rangle = 6l\partial_t \langle u u' \rangle. \tag{3.27}$$

Under assumption of stationarity (see *e.g.* [24]) the spatially-averaged increments are time independent and (3.25) yields the relation $\partial_t \langle u u' \rangle = \partial_t \langle u^2 \rangle = -2\varepsilon$, where we have also employed the definition of the energy dissipation rate, ε. Finally, substitution of this relation into (3.27) we have our twelfth law:

$$\langle \delta u^3(l) \rangle = -12\varepsilon l. \tag{3.28}$$

The third-order structure function scales linearly with length. Under the additional assumption of isotropy and with the use of tensor analysis, similar relations are found for Navier-Stokes [46], MHD [14, 66, 68], the Lagrangian-averaged Navier-Stokes alpha model [35], and for the Lagrangian-averaged MHD alpha model [56].

3.4 The Lagrangian-Averaged Alpha Model

In §2.1 we presented the idea of a closure scheme to solve fluid flow problems by evolving only the larger scales in a direct solution while the closure models the effects of the smaller scales. One possible closure is variously called the "Lagrangian-averaged alpha model", the "Camassa-Holm" equations, or simply the "alpha model" [11, 34, 1, 22, 36]. Two excellent reviews were recently written [44, 43] and are summarized here. The Lagrangian-averaged Navier-Stokes alpha (LANS-α) model began as a one-dimensional model of nonlinear shallow-water wave dynamics [11] and was later rederived from Hamilton's principle of least action as follows [38, 39, 15, 18, 33]. One begins with the Lagrangian density[13] in Hamilton's principle[14] for incompressible fluid motion. The fluid velocity and volume element are decomposed into their average and fluctuating parts (using Lagrangian coordinates fixed to the fluid current). Then Taylor's

[13] The Lagrangian density is the density of the kinetic energy minus the potential energy.
[14] Variational methods will not be discussed in this work.

frozen-in turbulence hypothesis, that small-scale turbulent fluctuations (those smaller than the length alpha) are swept along by the larger scale motions [76], is taken. In this way the averaging occurs along the Lagrangian fluid trajectory (see Figure 3.7). Also, we assume that these small-scale fluctuations are homogeneous and isotropic. That is, under any lateral translations and under any rotations they look the same. Finally, the energy in the small-scale turbulence can be derived from the energy of the mean fluid velocity by the hypotheses. Similar derivations have also extended the alpha model to the compressible fluid case [6] and to the anisotropic case, by dynamically varying the length alpha [79].

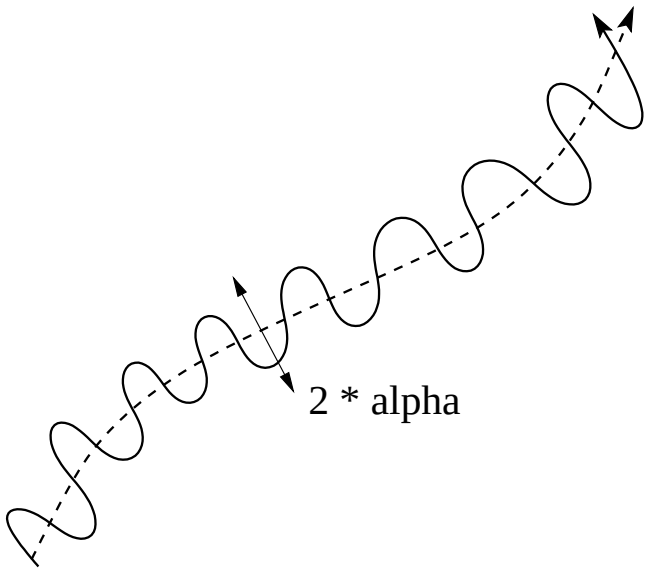

Figure 3.7: Illustration of Lagrangian averaging. The solid line depicts the flow of a fluid parcel. The dashed line is the Lagrangian average of this motion removing fluctuations smaller than size alpha. Twice alpha is depicted by the double-headed arrow.

By making the approximation before applying Hamilton's principle important fluid dynamical properties are retained such as conservation both of energy and potential fluid vorticity in the absence of viscosity and Kelvin's theorem which insures the proper dynamics of circulation. Other methods to model turbulent flows include Reynolds-averaged Navier-Stokes (RANS) simulations which separate the ensemble av-

eraged motions and the fluctuating fluid motions at fixed positions in space and the large eddy simulations (LES) framework which spatially low-bandpass filters the flow (see Figures 3.8 and 3.9). In this way, most of the modeling effort happens after Hamilton's principle and the conservation of invariants is lost. In other words, the dissipation is modified (LES model the small scales as eddy viscosity and, hence, are intrinsically dissipative). LANS$-\alpha$ modifies the nonlinearity in the Lagrangian-averaged Euler alpha model and adds the dissipation *add hoc*.

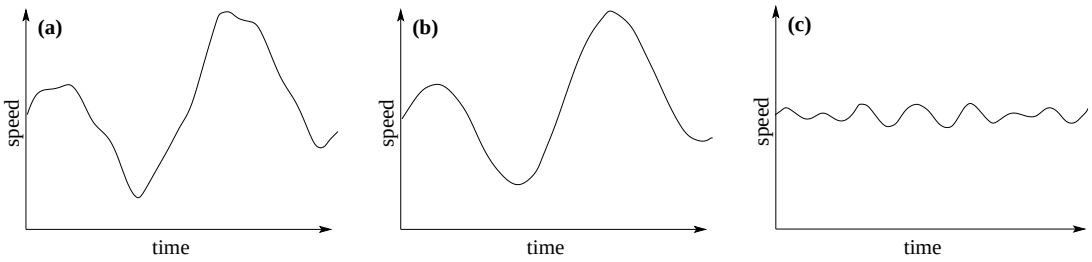

Figure 3.8: Illustration of Reynolds decomposition. Figures depict one-dimensional velocity fluctuations at a fixed position in space versus time. Panel **(a)** shows the complete fluctuations. Panel **(b)** shows the average motions. Panel **(c)** shows the fluctuations about the average motions.

LANS$-\alpha$ solutions for pipe flow were compared with experimental data for Reynolds numbers from 10^5 to over 10^7 and were found to match the measured mean velocity all the way across the pipe [15, 17]. Reference [18] shows that for scales larger than alpha ($k\alpha < 1$), the energy spectrum for homogeneous isotropic Navier-Stokes turbulence ($\sim k^{-5/3}$) is preserved. That is, for the energy spectrum at least, LANS$-\alpha$ is correctly mimicking the effect of the small scales on the large scales. For scales smaller than alpha ($k\alpha > 1$), the LANS$-\alpha$ energy spectrum is $\sim k^{-3}$ as predicted by [22]. This faster decay of energy is what makes numerical solutions at lower resolutions than for exact Navier-Stokes possible. Reference [16] found that they were able to reduce the resolution by a factor of 8 (saving a factor of 256 in computation time) for 3D, homogeneous, isotropic LANS-α.

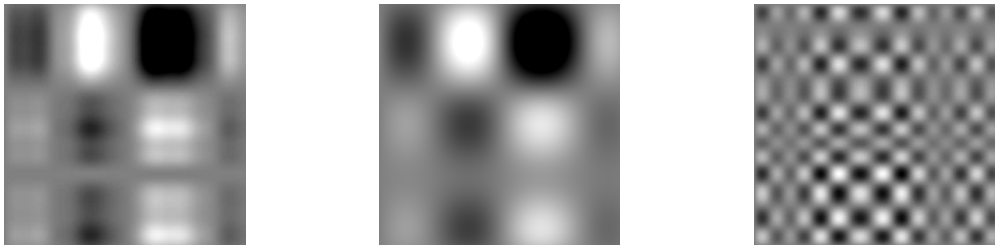

Figure 3.9: Example of spatial filtering: two-dimensional field of 1D velocities. White represents out of the page velocity, black represents into the page, and shades of grey for intermediate values. The leftmost image is the complete field, the middle image has small fluctuations filtered out, and the rightmost image is those small fluctuations (amplitude scale magnified).

Three-dimensional incompressible, decaying (and forced [57]) turbulence was investigated under a variety of initial conditions [37, 26, 27, 59, 58, 57]. LES methods and the LANS$-\alpha$ model were compared to direct numerical solutions of the Navier-Stokes equation at much higher resolution. In all cases LANS$-\alpha$ was found comparable with the best of standard LES models. To model the small scales, LES introduces additional dissipation. Consequently, [26, 27] found that the alpha model produces sharper more-pronounced coherent structures than even dynamic LES models in turbulent shear mixing.

The alpha model also tested well for boundary effects, jets, wakes, and plumes [19, 41, 70]. For quasi-geostrophy it has yielded mixed results [30, 40]. Results for rotating shallow water were better [42, 40] but bring up the question of determining the optimal length alpha for good predictions. LANS$-\alpha$ preserves but modifies the elliptic instability (conversion of 2D fluid motion into 3D convection) [21]. For the baroclinic instability it was found that for LANS$-\alpha$ it occurs at the same forcing values as for exact Navier-Stokes [42].

3.4.1 Simplified rederivation of LANS$-\alpha$

A simplified rederivation of the LANS$-\alpha$ model was made [60] by defining a local spatial averaging and neglecting fluctuations about that average. Starting from the velocity $\boldsymbol{u}$ in the Navier-Stokes equations (2.7), we define[15] a smoothed velocity field in Fourier-space,

$$\hat{u}_s = \frac{\hat{u}}{1+\alpha^2 k^2}, \tag{3.29}$$

then,

$$\boldsymbol{u_s} = F^{-1}[\hat{u_s}] = F^{-1}[\hat{u} \cdot \frac{1}{1+\alpha^2 k^2}] = \int G_\alpha(\boldsymbol{x}-\boldsymbol{x}')\boldsymbol{u}(\boldsymbol{x}',t)d^3\boldsymbol{x}', \tag{3.30}$$

where

$$G_\alpha(\boldsymbol{r}) = \int \frac{e^{i\boldsymbol{k}\cdot\boldsymbol{r}}}{1+\alpha^2 k^2}\frac{d^3\boldsymbol{k}}{(2\pi)^3} \tag{3.31}$$

is the inverse transform of $(1+\alpha^2 k^2)^{-1}$. α is the length scale over which $\boldsymbol{u}$ is smoothed. Taking the inverse Fourier transform of $\hat{u} = \hat{u}_s + \alpha^2 k^2 \hat{u}_s$, we find

$$\boldsymbol{u} = \boldsymbol{u_s} + \frac{\alpha^2}{(2\pi)^3}\int k^2 e^{i\boldsymbol{k}\cdot\boldsymbol{r}}\hat{\boldsymbol{u_s}}d^3\boldsymbol{k} = (1-\alpha^2\nabla^2)\boldsymbol{u_s}. \tag{3.32}$$

Substituting $\boldsymbol{u} \equiv \boldsymbol{u_s} + \boldsymbol{\delta u}$ into the vorticity equation for Navier-Stokes (A.10),

$$\partial_t \boldsymbol{w} + \boldsymbol{u}\cdot\boldsymbol{\nabla}\boldsymbol{w} = \boldsymbol{w}\cdot\boldsymbol{\nabla}\boldsymbol{u} + \boldsymbol{\nabla}\times\mathcal{F} + \nu\nabla^2\boldsymbol{w},$$

we find

$$\partial_t \boldsymbol{w} + (\boldsymbol{u_s}+\boldsymbol{\delta u})\cdot\boldsymbol{\nabla}\boldsymbol{w} - \boldsymbol{w}\cdot\boldsymbol{\nabla}(\boldsymbol{u_s}+\boldsymbol{\delta u}) = \boldsymbol{\nabla}\times\mathcal{F} + \nu\nabla^2\boldsymbol{w}. \tag{3.33}$$

Recall that vorticity is the curl of velocity, $\boldsymbol{w} \equiv \boldsymbol{\nabla}\times\boldsymbol{u}$. Neglecting fluctuations about the smoothed velocity, we approximate $\boldsymbol{\delta u} \ll \boldsymbol{u_s}$ while leaving the source term $\boldsymbol{w}$ alone.

$$\partial_t \boldsymbol{w} + \boldsymbol{u_s}\cdot\boldsymbol{\nabla}\boldsymbol{w} - \boldsymbol{w}\cdot\boldsymbol{\nabla}\boldsymbol{u_s} = \boldsymbol{\nabla}\times\mathcal{F} + \nu\nabla^2\boldsymbol{w} \tag{3.34}$$

Using the identity, $\boldsymbol{\nabla}\times(\boldsymbol{A}\times\boldsymbol{B}) = \boldsymbol{B}\cdot\boldsymbol{\nabla}\boldsymbol{A} - \boldsymbol{A}\cdot\boldsymbol{\nabla}\boldsymbol{B} - \boldsymbol{B}(\boldsymbol{\nabla}\cdot\boldsymbol{A}) + \boldsymbol{A}(\boldsymbol{\nabla}\cdot\boldsymbol{B})$ and that $\boldsymbol{w}$ and $\boldsymbol{u_s}$ are divergence free, we find

$$\partial_t \boldsymbol{w} + \boldsymbol{\nabla}\times(\boldsymbol{w}\times\boldsymbol{u_s}) = \boldsymbol{\nabla}\times\mathcal{F} + \nu\nabla^2\boldsymbol{w}. \tag{3.35}$$

[15] Other filters are possible.

If we remove a curl, the result is

$$\partial_t \boldsymbol{u} + \boldsymbol{w} \times \boldsymbol{u_s} = \mathcal{F} + \nu \nabla^2 \boldsymbol{u}. \tag{3.36}$$

Using tensor math notation (see §B), we see that

$$\boldsymbol{w} \times \boldsymbol{u_s} = \epsilon_{ikl} w^k u_s^l = \epsilon_{kli} \epsilon^{kjm} u_s^l \partial_j u_m = u_s^j \partial_j u_i - u_s^j \partial_i u_j \tag{3.37}$$

where we made use of identity (B.7). We can see that $u_s^j \partial_j u_i$ is just $\boldsymbol{u_s} \cdot \boldsymbol{\nabla u}$. Upon using $\partial_i (u_j u_s^j) = u_j \partial_i u_s^j + u_s^j \partial_i u_j$, we finally arrive at the LANS$-\alpha$ model

$$\partial_t \boldsymbol{u} + \boldsymbol{u_s} \cdot \boldsymbol{\nabla u} + \boldsymbol{\nabla} \mathcal{P} + \boldsymbol{\nabla u_s^T} \cdot \boldsymbol{u} - \nu \nabla^2 \boldsymbol{u} = \mathcal{F} \tag{3.38}$$

where $\mathcal{P} = -u_j u_s^j$ is a pressure-like scalar and $\boldsymbol{\nabla u_s^T} \cdot \boldsymbol{u}$ is just $u_j \partial_i u_s^j$.

From the Courant Friedrich Levy (CFL) condition, we know that a numerical solution will be unstable if the maximum velocity allowed by the discretization, $\frac{\Delta x}{\Delta t}$, is less than the maximum propagation velocity of the solution. This places an upper limit on the time step of $\Delta t \sim \frac{1}{uN}$. Thus, the total computation cost to reach a fixed time will go as N^d, d being the dimension of the space, for the number of grid points and another power of N for the time stepping, $\sim N^{d+1}$.[16] If the LANS$-\alpha$ reduces the required resolution by a factor of 2, the time savings will be a factor of 8 in 2D and 16 in 3D.[17] A reduction of resolution by a factor of 4 would be a savings of a factor of 64 or 256, respectively.[18]

3.4.2 Lagrangian-Averaged Magneto-Hydrodynamic Alpha (LAMHD$-\alpha$) Model

Following the method of §3.4.1, we derive the LAMHD$-\alpha$ equations from the MHD equations (2.27). We do no smoothing to either the vorticity or the current,

[16] This is an over-simplification. Actually, the spatial number of degrees of freedom in 3D, and hence the memory requirements, goes as $Re^{9/4}$. Taking into account CFL, the total computation time is proportional to Re^3.

[17] Actually, for the alpha model we find $Re^{3/4}$ for memory requirements and computation time $\sim Re$. This translates to a memory savings of $Re^{3/2}$ and a computation time savings of Re^2.

[18] Falling back on our Moore's law calculations, this would mean having the numerical solution to a given problem 12 years early!

which are the curl of the velocity and magnetic field, respectively. We do define the smoothed velocity, $\boldsymbol{u}_s$, and the smoothed magnetic, $\boldsymbol{b}_s$, fields in the same way as for LANS-α,

$$\boldsymbol{u} = (1 - \alpha^2\nabla^2)\boldsymbol{u_s} \tag{3.39}$$

and

$$\boldsymbol{b} = (1 - \alpha^2\nabla^2)\boldsymbol{b_s}. \tag{3.40}$$

Note that here we have made the simplification of the smoothing length α being the same for magnetic and velocity fields. This need not be so. There is the possibility of assigning one value for $\boldsymbol{v}$ and a different value $\boldsymbol{b}$ (α_K and α_M, respectively) but $\alpha_K = \alpha_M = \alpha$ is appropriate considering our choice of $\eta = \nu$ in the simulations. Upon substituting $\boldsymbol{b} \equiv \boldsymbol{b_s} + \boldsymbol{\delta b}$ into the LANS$-\alpha$ equation (3.38) with the Lorenz force (2.26), we find

$$\partial_t \boldsymbol{u} + \boldsymbol{u}_s \cdot \boldsymbol{\nabla u} + \boldsymbol{\nabla u}_s^T \cdot \boldsymbol{u} = -\boldsymbol{\nabla}\mathcal{P} + \boldsymbol{j} \times (\boldsymbol{b}_s + \boldsymbol{\delta b}) + \nu\nabla^2\boldsymbol{u} \tag{3.41}$$

and all that remains is to neglect fluctuations about the smoothed magnetic field and approximate $\boldsymbol{\delta b} \ll \boldsymbol{b_s}$. For the induction equation (2.25), we note that the absence of magnetic monopoles, $\boldsymbol{\nabla} \cdot \boldsymbol{b} = 0$, and Ampere's law imply

$$\eta\boldsymbol{\nabla}^2\boldsymbol{b} = -\eta\mu\boldsymbol{\nabla} \times \boldsymbol{j}. \tag{3.42}$$

Therefore upon substitution of $\boldsymbol{b} = \boldsymbol{b_s} + \boldsymbol{\delta b}$ and $\boldsymbol{u} = \boldsymbol{u_s} + \boldsymbol{\delta u}$ into (2.25) we find

$$\partial_t(\boldsymbol{b}_s + \boldsymbol{\delta b}) = \boldsymbol{\nabla} \times ((\boldsymbol{u}_s + \boldsymbol{\delta u}) \times (\boldsymbol{b}_s + \boldsymbol{\delta b})) - \eta\mu\boldsymbol{\nabla} \times \boldsymbol{j}. \tag{3.43}$$

Again, we neglect fluctuations about the smoothed magnetic and velocity fields while leaving the source term, $\boldsymbol{j}$, alone and reuse (3.42) to complete the derivation of the LAMHD$-\alpha$ equations,

$$\partial_t \boldsymbol{u} + \boldsymbol{u}_s \cdot \boldsymbol{\nabla u} + u_j\boldsymbol{\nabla u}_s^j = -\boldsymbol{\nabla}P + \boldsymbol{j} \times \boldsymbol{b}_s + \nu\nabla^2\boldsymbol{u} + \mathcal{F}_K \tag{3.44a}$$

$$\partial_t \boldsymbol{b}_s + \boldsymbol{u}_s \cdot \boldsymbol{\nabla b}_s = \boldsymbol{b}_s \cdot \boldsymbol{\nabla u}_s + \eta\nabla^2\boldsymbol{b} + \mathcal{F}_M \tag{3.44b}$$

using, of course, that the smoothed fields are divergence free.

LAMHD$-\alpha$ has been considered before in the non-dissipative case [36] and in the turbulent regime for 2D [55], for 3D [54], and for low magnetic Prandtl number, $P_M = \frac{\nu}{\eta}$, dynamos [69]. In [55] it was discovered that LAMHD$-\alpha$ recovers the main features of the long wavelength behavior of 2D MHD turbulent flows whereas small-scale detailed information is lost. For instance, the locations of specific features are virtually never reproduced after short times. In addition non-Gaussian wings of the probability density functions (for the current density, for example) were found. These are indicative of intermittency but are not as quantitative a measure of it as the structure functions studied here. Another difference of small note between this study and [55] is that the induction equation only is forced in [55] while both equations are subject to forcing here.

Chapter 4

2D MHD and LAMHD$-\alpha$ Turbulence

Three-dimensional (3D) calculations are very expensive in computer resources (for example between a 1024^3 3D experiment and a 1024^2 2D experiment, the 2D choice is one-thousand times cheaper). It is preferable, then, to study intermittency in two dimensions if we can. This is not possible for Navier-Stokes because in 2D hydrodynamics the energy has an inverse cascade to large scales.[1] Without the transfer of energy to small scales strong, localized events are not possible. For 2D MHD, however, the energy has a direct cascade to small scales. This makes 2D MHD similar to the 3D case and allows us to study intermittency at high resolution. To test LAMHD$-\alpha$ we make a fully resolved, direct numerical simulation (DNS) run at the highest attainable Reynolds number for our computer resources and compare the results to LAMHD$-\alpha$ results obtained at lower resolutions. Direct numerical simulation means that we solve the equations numerically by resolving all scales down to the scale of viscous dissipation. We will also variously call this solution the MHD solution as it is the solution to the MHD equations as opposed to the LAMHD$-\alpha$ equations.

[1] For instance, looking at a national weather map, one can see the large-scale systems formed in the nearly 2D flows of a stratified atmosphere.

4.1 Two-Dimensional Magnetohydrodynamics (2D MHD)

In two dimensions, the velocity and magnetic field can be expressed as the curl of a scalar stream function Ψ and a scalar vector potential a_z, respectively:

$$\mathbf{v} = \nabla \times (\Psi \hat{\mathbf{z}}), \quad \mathbf{v}_s = \nabla \times (\Psi_s \hat{\mathbf{z}}) \tag{4.1a}$$

$$\mathbf{b} = \nabla \times (a_z \hat{\mathbf{z}}), \quad \mathbf{b}_s = \nabla \times (a_{s_z} \hat{\mathbf{z}}) \tag{4.1b}$$

Upon substitution into (2.27) combined with taking the divergence of the momentum equation (2.27a) and removing a curl from the induction equation (2.27d), our 2D MHD equations become

$$\partial_t \nabla^2 \Psi = [\Psi, \nabla^2 \Psi] - [a_z, \nabla^2 a_z] + \nu \nabla^2 \nabla^2 \Psi \tag{4.2a}$$

$$\partial_t a_z = [\Psi, a_z] + \eta \nabla^2 a_z \tag{4.2b}$$

where

$$[F, G] = \partial_x F \partial_y G - \partial_x G \partial_y F. \tag{4.3}$$

Similarly, the 2D alpha model equations are

$$\partial_t \nabla^2 \Psi = [\Psi_s, \nabla^2 \Psi] - [a_{s_z}, \nabla^2 a_z] + \nu \nabla^2 \nabla^2 \Psi \tag{4.4a}$$

$$\partial_t a_{s_z} = [\Psi_s, a_{s_z}] + \eta \nabla^2 a_z \tag{4.4b}$$

where $\Psi = (1 - \alpha^2 \nabla^2)\Psi_s$ and $a = (1 - \alpha^2 \nabla^2) a_s$. Evolution of these equations for scalar fields is clearly more computationally efficient than for the vector field equations.

4.2 Invariants

4.2.1 Invariants in 2D MHD

In this section we develop the expressions for the ideal invariants (in the case for which there is no viscous or Ohmic dissipative terms) and for the decay laws (in the

presence of dissipation). For 2D MHD, the ideal invariants are the total energy,

$$E = \int dA \frac{1}{2}(u^2 + b^2), \tag{4.5}$$

the total cross helicity,

$$H_C = \int dA \frac{1}{2} \boldsymbol{u} \cdot \boldsymbol{b}, \tag{4.6}$$

and the total mean-square vector potential,

$$\mathcal{A} = \int dA \frac{1}{2} a_z^2. \tag{4.7}$$

The decay laws (or dissipation rates) of these invariants under the influence of dissipation are[2]

$$\frac{dE}{dt} = -\nu \int dA w^2 - \eta \int dA j^2 = -\nu \langle w^2 \rangle - \eta \langle j^2 \rangle \tag{4.8a}$$

$$\frac{dH_C}{dt} = -\frac{1}{2}(\nu + \eta) \int dA w \cdot j \tag{4.8b}$$

$$\frac{d\mathcal{A}}{dt} = -\nu \int dA b^2. \tag{4.8c}$$

To calculate the energy dissipation rate for 2D MHD (4.8a), we take the dot product of the velocity with the Navier-Stokes equation (2.27a) added to the dot product of the magnetic field with the induction equation (2.27d) and integrate,

$$\int dA \boldsymbol{u} \cdot \partial_t \boldsymbol{u} + \boldsymbol{b} \cdot \partial_t \boldsymbol{b} + \int dA \boldsymbol{u} \cdot \boldsymbol{u} \cdot \boldsymbol{\nabla} \boldsymbol{u} =$$
$$- \int dA \boldsymbol{u} \cdot \boldsymbol{\nabla} p + \int dA \boldsymbol{u} \cdot \boldsymbol{j} \times \boldsymbol{b} + \boldsymbol{b} \cdot \boldsymbol{\nabla} \times (\boldsymbol{u} \times \boldsymbol{b}) + \int dA \boldsymbol{u} \cdot \nu \nabla^2 \boldsymbol{u} + \boldsymbol{b} \cdot \eta \nabla^2 \boldsymbol{b}. \tag{4.9}$$

Using $\frac{1}{2}\partial_t(\boldsymbol{u} \cdot \boldsymbol{u}) = \boldsymbol{u} \cdot \partial_t \boldsymbol{u}$, we derive

$$\int dA \boldsymbol{u} \cdot \partial_t \boldsymbol{u} + \boldsymbol{b} \cdot \partial_t \boldsymbol{b} = \frac{d}{dt} \int dA \frac{1}{2} \left(u^2 + b^2\right) \equiv \frac{dE}{dt}, \tag{4.10}$$

the time rate of change of the total energy in the system. It can easily be shown that the integral of a divergence (or a gradient) over a periodic domain is zero $\int dA \boldsymbol{\nabla} p = 0$.

[2] Angle brackets, $\langle \cdot \rangle$, denote integration over the entire domain and will be our preferred notation where square vorticity and square current are concerned.

Using integration by parts, we have the same for an advection-like term (movement across periodic boundaries is conservative),

$$\int dA\boldsymbol{u}\cdot\boldsymbol{\nabla}p=\int dA\boldsymbol{\nabla}\cdot(p\boldsymbol{u})-\int dAp\boldsymbol{\nabla}\cdot\boldsymbol{u}=0, \tag{4.11}$$

by using that the integral of a divergence is zero and the incompressibility condition. For the second left-hand term in (4.9), we use what could be called the velocity-cross-vorticity identity, $\boldsymbol{u}\times\boldsymbol{w}=\frac{1}{2}\boldsymbol{\nabla}u^2-\boldsymbol{u}\cdot\boldsymbol{\nabla}\boldsymbol{u}$,

$$\int dA\boldsymbol{u}\cdot\boldsymbol{u}\cdot\boldsymbol{\nabla}\boldsymbol{u}=\int dA\boldsymbol{u}\cdot\frac{1}{2}\boldsymbol{\nabla}u^2-\int dA\boldsymbol{u}\cdot(\boldsymbol{u}\times\boldsymbol{w})=0. \tag{4.12}$$

The advection-like term is zero and $\boldsymbol{u}\times\boldsymbol{w}$ being perpendicular to $\boldsymbol{u}$ has a zero dot product with it. For the first part of the second right-hand term, we reuse our identity to find

$$\boldsymbol{u}\cdot\boldsymbol{j}\times\boldsymbol{b}=\boldsymbol{u}\cdot\boldsymbol{b}\cdot\boldsymbol{\nabla}\boldsymbol{b}-\boldsymbol{u}\cdot\frac{1}{2}\boldsymbol{\nabla}b^2. \tag{4.13}$$

The advection-like term again being zero, we are left with $\boldsymbol{u}\cdot\boldsymbol{b}\cdot\boldsymbol{\nabla}\boldsymbol{b}$. From $\boldsymbol{\nabla}\cdot\boldsymbol{u}=\boldsymbol{\nabla}\cdot\boldsymbol{b}=0$, we have $\boldsymbol{\nabla}\times(\boldsymbol{u}\times\boldsymbol{b})=\boldsymbol{b}\cdot\boldsymbol{\nabla}\boldsymbol{u}-\boldsymbol{u}\cdot\boldsymbol{\nabla}\boldsymbol{b}$ for the second part of the second right-hand term. Recalling that dot products do not commute in tensor analysis, we have for the second-right hand term in (4.9),

$$\boldsymbol{u}\cdot\boldsymbol{b}\cdot\boldsymbol{\nabla}\boldsymbol{b}+\boldsymbol{b}\cdot\boldsymbol{b}\cdot\boldsymbol{\nabla}\boldsymbol{u}-\boldsymbol{b}\cdot\boldsymbol{u}\cdot\boldsymbol{\nabla}\boldsymbol{b}. \tag{4.14}$$

These terms represent the exchange of magnetic and kinetic energy. In tensor notation (see §B), we write

$$u_m b_j\partial_j b_m+b_m b_j\partial_j u_m-b_m u_j\partial_j b_m. \tag{4.15}$$

Integrating the middle term by parts,

$$u_m b_j\partial_j b_m+b_j\partial_j(b_m u_m)-u_m b_j\partial_j b_m-b_m u_j\partial_j b_m. \tag{4.16}$$

Whether a quantity is advection-like with velocity or with the magnetic field, it will still integrate to zero over periodic boundary conditions, and we are left with $-b_m u_j\partial_j b_m$.

This we can recognize as being the same as $-\boldsymbol{u}\cdot\boldsymbol{\nabla}b^2/2$ which gives a zero contribution. Now, (4.9) can be reduced to

$$\frac{dE}{dt} = \nu\int dA\boldsymbol{u}\cdot\nabla^2\boldsymbol{u} + \eta\int dA\boldsymbol{b}\cdot\nabla^2\boldsymbol{b}. \tag{4.17}$$

These terms have the same form and we will simplify it only once. In tensor notation, $\boldsymbol{b}\cdot\nabla^2\boldsymbol{b} = b_m\partial_j\partial_j b_m$ which, upon integration by parts, is $\partial_j(b_m\partial_j b_m) - (\partial_j b_m)(\partial_j b_m)$. After ignoring the divergence term this only differs from $(\boldsymbol{\nabla}\times\boldsymbol{b})^2$ by the term $\partial_j(\partial_m b_m b_j)$ which is also a divergence. Finally, we arrive at

$$\frac{dE}{dt} = -2\nu\Omega - 2\eta\Omega_M, \tag{4.18}$$

where $E \equiv \frac{1}{2}\langle u^2 + b^2\rangle$, $\Omega \equiv \frac{1}{2}\langle w^2\rangle$, and $\Omega_M \equiv \frac{1}{2}\langle j^2\rangle$.

The mean-square vector potential dissipation rate (4.8c), can be found by noting that the magnetic field is the curl of the square vector potential which in 2D is represented by $\boldsymbol{b} = \boldsymbol{\nabla}\times(a_z\hat{\boldsymbol{z}})$. Substituting this into the induction equation (2.27d),

$$\partial_t\boldsymbol{\nabla}\times(a_z\hat{\boldsymbol{z}}) = \boldsymbol{\nabla}\times(\boldsymbol{u}\times\boldsymbol{b}) + \eta\boldsymbol{\nabla}^2\boldsymbol{\nabla}\times(a_z\hat{\boldsymbol{z}}). \tag{4.19}$$

After removing a curl, we find

$$\partial_t a_z = (\boldsymbol{u}\times\boldsymbol{b})_z + \eta\boldsymbol{\nabla}^2 a_z. \tag{4.20}$$

Multiplying by a_z and integrating gives us

$$\frac{d}{dt}\int dA\frac{1}{2}a_z^2 = \int dA a_z(\boldsymbol{u}\times\boldsymbol{b})_z + \eta\int dA a_z\boldsymbol{\nabla}^2 a_z. \tag{4.21}$$

The first term on the right hand side can be seen to vanish as follows.

$$\boldsymbol{a}\cdot(\boldsymbol{u}\times(\boldsymbol{\nabla}\times\boldsymbol{a})) = \boldsymbol{u}\cdot((\boldsymbol{\nabla}\times\boldsymbol{a})\times\boldsymbol{a}) = \boldsymbol{u}\cdot\left(\boldsymbol{a}\cdot\boldsymbol{\nabla}\boldsymbol{a} - \frac{1}{2}\boldsymbol{\nabla}a^2\right) \tag{4.22}$$

Upon integration, the advection-like term is zero and in two dimensions, we have $\boldsymbol{u}\cdot\boldsymbol{a}\cdot\boldsymbol{\nabla}\boldsymbol{a} = u_z a_z\partial_z a_z$. As $u_z = \partial_z a_z = 0$ there is no contribution from this term. Integrating by parts will simplify the dissipation term $a_z\partial_i(\partial_i a_z) = \partial_i(a_z\partial_i a_z) - (\partial_i a_z)^2$. The

divergence term, of course, gives no contribution. Further simplification results from noticing that

$$b^2 = (\boldsymbol{\nabla} \times \boldsymbol{a}) \cdot (\boldsymbol{\nabla} \times \boldsymbol{a}) = \partial_m a_n \partial_m a_n - \partial_n (\partial_m a_m a_n) = (\partial_i a_z)^2 \tag{4.23}$$

after integration. This also gives us the Fourier-space relation $k^2 a^2 = b^2$. Finally, we have the relation

$$\frac{d\mathcal{A}}{dt} = -2\eta E_M, \tag{4.24}$$

where $\mathcal{A} \equiv \int dA \frac{1}{2} a_z^2$ and $E_M \equiv \int dA \frac{1}{2} b^2$.

These two relations (4.18) and (4.24) define the energy, E, and square vector potential, $\mathcal{A}$ as invariants of 2D MHD ((4.8b) can be derived in the same way). In the absence of dissipation, they are conserved quantities.

4.2.2 Cascades in 2D MHD

"Selective decay" refers to

> turbulent processes in which one or more ideal invariants are dissipated rapidly relative to another, due to the transfer of the dissipated quantities to short wavelengths where the dissipation coefficients become effective.[55]

The system seeks a state where the dissipated quantity is as close to zero as can be for the surviving value of the nearly-conserved quantity. In 2D MHD with negligible cross helicity (the case we study),[3] the dissipated quantity is energy. For 2D Navier-Stokes, the dissipated quantity is enstrophy (which therefore must experience a direct cascade to smaller scales). Fjortoft's theorem (see [53]) suggests such a direct cascade for enstrophy and an inverse cascade (to larger scales) for energy for the 2D Navier-Stokes case. We now apply the same argument for 2D MHD to illustrate its dynamics. In Fourier space we consider only three modes, k_1, $k_2 = 2k_1$, and $k_3 = 3k_1$. Let $E(k_i, t)$

[3] We use random phases for $\boldsymbol{u}$ and $\boldsymbol{b}$ either in the initial conditions or in the forcing. This implies negligible correlation between them and, hence, negligible cross helicity.

and $\mathcal{A}(k_i, t)$ be the energy and the square vector potential, respectively, in the mode k_i at time t. Defining the variation $\delta E_i = E(k_i, t_2) - E(k_i, t_1)$, we see that conservation of energy between times t_1 and t_2 implies

$$\delta E_1 + \delta E_2 + \delta E_3 = 0. \tag{4.25}$$

Similarly, conservation of square vector potential will imply

$$\delta \mathcal{A}_1 + \delta \mathcal{A}_2 + \delta \mathcal{A}_3 = 0, \tag{4.26}$$

or, using $k^2 \mathcal{A} \sim b^2$,

$$\frac{1}{k_1^2}\delta E_{M_1} + \frac{1}{k_2^2}\delta E_{M_2} + \frac{1}{k_3^2}\delta E_{M_3} = 0. \tag{4.27}$$

Assuming the system is initially in equipartition, $E_M = E_K = \frac{1}{2}E$. Using this and the relation between our modes, we find

$$36\delta E_1 + 9\delta E_2 + 4\delta E_3 = 0. \tag{4.28}$$

Solving (4.25) and (4.28) we find $\delta E_1 = -\frac{5}{32}\delta E_2$ and $\delta E_3 = -\frac{27}{32}\delta E_2$. If energy moves away from the middle energy band ($\delta E_2 < 0$), more of it goes to smaller scales (k_3) than to larger scales (k_1). This suggests a direct cascade of energy. Conversely, for square vector potential, we find $\delta \mathcal{A}_1 = -\frac{5}{8}\delta \mathcal{A}_2$ and $\delta \mathcal{A}_3 = -\frac{3}{8}\delta \mathcal{A}_2$ which suggests an inverse cascade (more energy goes from k_2 to k_1 than to k_3). Given this inverse cascade of square vector potential, in a freely decaying run with negligible cross helicity, it is expected that $\mathcal{A}$ will cascade to larger scales where it will dissipate slowly. As a result, the final state is expected to be dominated by magnetic energy.

4.2.3 Invariants in 2D LAMHD$-\alpha$

For 2D LAMHD$-\alpha$, the ideal invariants are the total energy,

$$E = \int dA \frac{1}{2}(\boldsymbol{u} \cdot \boldsymbol{u}_s + \boldsymbol{b} \cdot \boldsymbol{b}_s), \tag{4.29}$$

the total cross helicity,

$$H_C = \int dA \frac{1}{2} \boldsymbol{u} \cdot \boldsymbol{b}_s, \tag{4.30}$$

and the total mean-square vector potential,

$$\mathcal{A} = \int dA \frac{1}{2} a_{s_z}^2. \tag{4.31}$$

The decay laws (or dissipation rates) of these invariants under the influence of dissipation are

$$\frac{dE}{dt} = -\nu \int dA w \cdot w_s - \eta \int dA j^2 = -\nu \langle w \cdot w_s \rangle - \eta \langle j^2 \rangle \tag{4.32a}$$

$$\frac{dH_C}{dt} = -\frac{1}{2}\nu \int dA w \cdot j - \frac{1}{2}\eta \int dA w \cdot j_s \tag{4.32b}$$

$$\frac{d\mathcal{A}}{dt} = -\nu \int dA \boldsymbol{b} \cdot \boldsymbol{b}_s. \tag{4.32c}$$

The conservation of the invariants under the alpha model is one the greatest strengths of this closure. In the limit $\alpha \to 0$, we recover the MHD invariants and decay laws. As the invariants are crucial for turbulence, it is the comparison between the MHD invariants and the LAMHD$-\alpha$ invariants that shall be our test of the alpha model. The decay laws of LAMHD$-\alpha$ have forms similar to

$$\frac{d}{dt} \int dA (\boldsymbol{u}_s \cdot \boldsymbol{u}) = \int dA \partial_t (\boldsymbol{u}_s \cdot \boldsymbol{u}) = \int dA (\boldsymbol{u}_s \cdot \partial_t \boldsymbol{u} + \boldsymbol{u} \cdot \partial_t \boldsymbol{u}_s). \tag{4.33}$$

As the Helmholtz operator, $(1 - \alpha^2 \nabla^2)$, is Hermitian we can use a significant simplification in the derivation of the invariants.

$$\int dA \boldsymbol{u}_s \cdot \partial_t \boldsymbol{u} = \int dA \boldsymbol{u}_s \cdot \partial_t (1 - \alpha^2 \nabla^2) \boldsymbol{u}_s = \int dA (1 - \alpha^2 \nabla^2) \boldsymbol{u}_s \cdot \partial_t \boldsymbol{u}_s = \int dA \boldsymbol{u} \cdot \partial_t \boldsymbol{u}_s \tag{4.34}$$

Therefore,

$$\frac{d}{dt} \int dA (\boldsymbol{u}_s \cdot \boldsymbol{u}) = 2 \int dA \boldsymbol{u}_s \cdot \partial_t \boldsymbol{u} \tag{4.35}$$

and

$$\frac{d}{dt} \int dA \frac{1}{2} (\boldsymbol{u}_s \cdot \boldsymbol{u} + \boldsymbol{b}_s \cdot \boldsymbol{b}) = \int dA (\boldsymbol{u}_s \cdot \partial_t \boldsymbol{u} + \boldsymbol{b} \cdot \partial_t \boldsymbol{b}_s). \tag{4.36}$$

The remainder of the derivation is then similar to §4.2.1.

4.3 Numerical Technique

Pseudospectral methods are preferred for their accuracy and ease of solution to a Poisson equation, which is needed to remove the pressure term from flow equations (see §A.1.2). It also is important to ensure energy dissipation is due to the viscous terms in the modeled equations rather than the numerical method used. Again, pseudospectral methods are preferred as they are non-dissipative and non-dispersive. In the absence of physical dissipation, energy piles up and a k^2 spectrum is obtained. The nonlinear advection term, however, can transfer energy to frequencies higher than can be resolved by the numerical grid. This contamination of resolved frequencies is called aliasing (see §2.4). For this reason we implement the two-thirds rule for dealiasing by zeroing all Fourier modes above $k_{max} = N/3$, where N is the linear resolution of the simulation, and require a resolution of $\Delta y \leq 3l_\nu$. As the highest possible Reynolds numbers can be achieved for homogeneous turbulence in a square box with periodic boundary conditions [51], this is the geometry, with edge length 2π, and boundary conditions that we will employ. We use the same parallel pseudospectral code as [55]. The FFTW [23] is employed, parallelized as described in [25], with a second-order Runge Kutta method for the time derivative. The balance equation, $\frac{dE}{dt} = \varepsilon - \nu\langle w^2\rangle - \eta\langle j^2\rangle$, was verified to be satisfied up to the machine precision.

4.4 Numerical Experiments

We test LAMHD$-\alpha$ against the fully resolved MHD ($\alpha \equiv 0$) results for a freely decaying run with identical initial conditions, dissipation and time-stepping and also for a forced run with identical forcing, dissipation, and time-stepping. Statistics for the forced run are averaged over 20 turn over times. The eddy turnover time is defined to be the length scale of the largest eddies divided by the root-mean-square (*r.m.s.*) velocity, $\tau \equiv l/v_{rms}$. That is, the time scale for the largest eddies to go around once.

4.4.1 Freely Decaying Turbulence

We study a MHD run using 2048^2 grid points, a 1024^2 LAMHD$-\alpha$ run with $\alpha_K = \alpha_M = 6/1024$, and a 512^2 LAMHD$-\alpha$ run with $\alpha_K = \alpha_M = 6/512$ all started with identical initial conditions. We specify the initial conditions in Fourier space with $\boldsymbol{u}$ and $\boldsymbol{b}$ represented as the Fourier series

$$\boldsymbol{u}(\boldsymbol{x},t) = \sum_k \boldsymbol{u}(\boldsymbol{k},t)e^{i\boldsymbol{k}\cdot\boldsymbol{x}}, \quad \boldsymbol{b}(\boldsymbol{x},t) = \sum_k \boldsymbol{b}(\boldsymbol{k},t)e^{i\boldsymbol{k}\cdot\boldsymbol{x}}.$$

The non-vanishing initial Fourier coefficients are to confined to a ring in k-space between $k = 1$ and $k = 3$. Random phases within this ring and unit *r.m.s.* values of the fields are employed. Kinetic viscosity and magnetic diffusivity, $\nu = \eta$, are 10^{-4} and the experiments are evolved in time without external forcing. The initial Reynolds number of the flow, $R = \frac{lu_{rms}}{\nu}$, based on a unit length scale in a square of edge 2π is 10,000. The Taylor Reynolds number,

$$R_\lambda = \frac{\lambda u_{rms}}{\nu}, \tag{4.37}$$

where

$$\lambda = 2\pi\sqrt{\langle u^2\rangle/\langle w^2\rangle}, \tag{4.38}$$

for peak dissipation, $t \approx 6.5$, is 1500 for DNS and 1700 for LAMHD$-\alpha$ as shown in Table 4.3.

4.4.2 Forced Turbulence

In designing the forced turbulence experiments, we begin with low resolution ($N = 128$) calculations. Due to the fact that computing time is proportional to N^3, it is helpful to determine the experimental parameters at relatively little computational cost and then reduce the viscosity as we increase resolution. We are seeking to have the magnetic and kinetic energies somewhat balanced (near equipartition), to reach the peak in vorticity (dissipation) relatively quickly and to have as high a Reynolds number as

we can for our resolution. The inverse cascade of square vector potential constrains the magnetic energy from going to zero, while the kinetic energy has a direct cascade. We therefore find 2D turbulent MHD flows to be magnetically dominated. For this reason we will require more forcing in the momentum equation than in the vector potential equation. After a few trials, we settle for $\mathcal{F}_M = 0.2$ in the vector potential equation and $\mathcal{F}_K = 0.45$ in the momentum equation. These values are space averages. We force at large scales as we are not interested in the inverse cascade for studying intermittency. This leaves more resolution for the direct cascade. The expressions of the external forces were loaded with random phases in the Fourier ring between $k = 1$ and $k = 2$, and the phases were changed randomly with a correlation time $\Delta t = 5 \times 10^{-2}$. For time-stepping we chose $\Delta t = 10^{-2}$.

As our code is fully dealiased, all modes above $N/3$ are suppressed. When the dissipation scale is of higher wave number than this, our solution will not be valid. Such a run is under-resolved. For an example, see Figure 4.1. For this run we have $k_\varepsilon \approx 105 > N/3 \approx 42$.[4] Examination of the current and vorticity spectra also clearly indicate that there is dissipation left unresolved as the spectra of current and vorticity are flat and there is little decrease in the Fourier domain. Note, however, that the kinetic and magnetic energies differ only by a factor of two and that the maximum dissipation is reached by $t \approx 30$ (a few turnover times). Several more experiments are made at this resolution as summarized in Table 4.1.

Parameters for new experiments are derived from previous runs as follows. As is well known, in the Kolmogorov limit of $R \to \infty$, we expect (3.14)

$$k \propto \left(\frac{\epsilon}{\nu^3}\right)^{\frac{1}{4}},$$

or, equivalently,

$$k^4 \nu^3 = const$$

[4] $k_\varepsilon \equiv (\frac{|\varepsilon|}{\nu^3})^{\frac{1}{4}}$ and should be similar to the Kolmogorov dissipation scale assuming $\langle w^2 \rangle \approx \langle j^2 \rangle$.

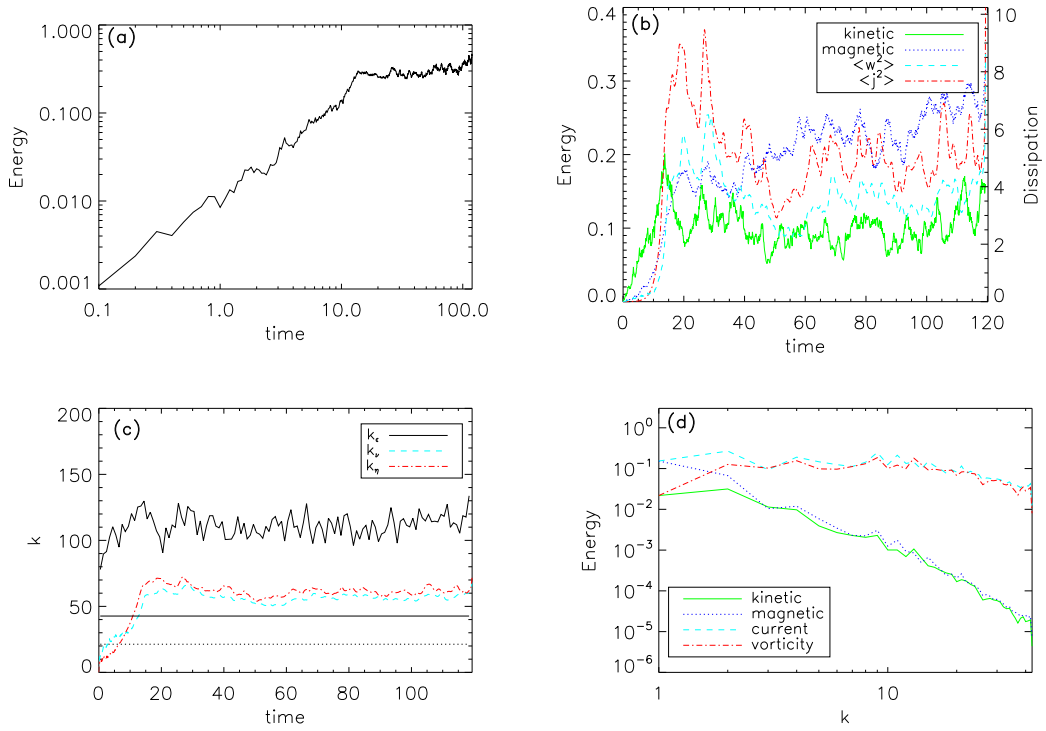

Figure 4.1: Example of under-resolved, forced run (experiment 3 from Table 4.1). Panel **(a)** shows energy versus time. Panel **(b)** shows kinetic energy (green, solid line), magnetic energy (blue, dotted line), average square vorticity (cyan, dashed line), and average square current (red, dash-dot line). Panel **(c)** is for the dissipative wavenumbers. Wavenumber of approximate Kolmogorov-like dissipation scales, $k_\varepsilon \equiv (\frac{|\varepsilon|}{\nu^3})^{\frac{1}{4}}$ (running average over $\Delta t = 0.1$) versus time as a solid black line. $k_\nu \equiv (\frac{\langle w^2 \rangle}{\nu^2})^{\frac{1}{4}}$ is indicated by a cyan dashed line while $k_\eta \equiv (\frac{\langle j^2 \rangle}{\eta^2})^{\frac{1}{4}}$ is indicated by a red dash-dot line. The N/3 resolution limit (solid line) and a reference line at N/6 (dotted) are also shown. Panel **(d)** shows the energy spectra for $t = 100$ with labels as in panel **(b)**.

Table 4.1: $N = 128$ forced experiments. Table shows viscosity, $\nu = \eta$, and approximate wave numbers for the Kolmogorov dissipative scale.

experiment	$\nu = \eta$	$k_\varepsilon \equiv (\frac{\lvert\varepsilon\rvert}{\nu^3})^{\frac{1}{4}}$	$k_\nu \equiv (\frac{\langle w^2 \rangle}{\nu^2})^{\frac{1}{4}}$	$k_\eta \equiv (\frac{\langle j^2 \rangle}{\eta^2})^{\frac{1}{4}}$
3	$5.88 \cdot 10^{-4}$	105	54	58
4	$1.0 \cdot 10^{-3}$	71	37	41
5	$1.25 \cdot 10^{-3}$	59	30	34
6	$2.0 \cdot 10^{-3}$	42	22	25
7	$3.0 \cdot 10^{-3}$	31	17	19

to hold for 2D MHD as it does for 3D Navier-Stokes (if we assume $\langle w^2 \rangle \approx \langle j^2 \rangle$). As an illustration we use the results of experiments 4 and 5 from Table 4.1 to predict the dissipative parameters, $\nu = \eta$, for $k = 42$. From experiment 4 we calculate

$$42^4 \nu^3 = 71^4 (10^{-3})^3 \rightarrow \nu \approx 2.01 \cdot 10^{-3}.$$

While from experiment 5 we calculate

$$42^4 \nu^3 = 59^4 (1.25 \cdot 10^{-3})^3 \rightarrow \nu \approx 1.97 \cdot 10^{-3}.$$

The accuracy of these predictions compared to experiment 6 is an indication that we have reached sufficiently high Reynolds number to make accurate predictions for higher resolution runs without concern for wasting much computation time due to poor parameter choices. For an example of a resolved run see Figure 4.2. Here we see that both the peak of the vorticity and of the current are well resolved (both decrease by three orders of magnitude) and that the dissipative scale approximations are all less than the resolution limit of N/3.

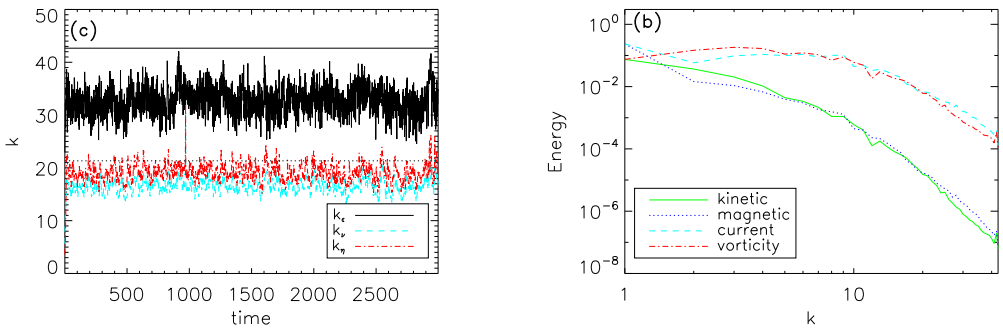

Figure 4.2: Example of resolved, forced run (experiment 7 from Table 4.1). Labels are as in Figure 4.1. Panel **(a)** shows the dissipative wavenumbers versus time. Panel **(b)** shows the spectra for $t = 2000$.

To safely scale our experiments to higher resolutions and Reynolds number, we increase our resolution by a factor of two. In going from the $N = 128$ experiment 7

to $N = 256$, we cut the time step and the viscosity/diffusivity in half. Our prediction from (3.14) is $k_\varepsilon \approx 52$ and the computed dissipation scale is $k_\varepsilon \approx 54$ (see Table 4.2). For LAMHD$-\alpha$ experiments, we will make experiments with one-half and one-quarter of the DNS resolution. It is reasonable, then, to design an experiment with $N/6 = 43 < k_\nu < 85 = N/3$ so that dissipation would be unresolvable at the lower resolution. Our prediction for $\nu = 7 \cdot 10^{-4}$ is $k_\nu \approx 50$ which would provide a better test for LAMHD$-\alpha$ than $k_\nu \approx 30$.[5]

Table 4.2: $N = 256$ forced experiments. Table shows viscosity, $\nu = \eta$, and approximate wave numbers for the Kolmogorov dissipative scale.

experiment	$\nu = \eta$	k_ε	k_ν	k_η
7	$1.5 \cdot 10^{-3}$	54	26	29
8	$7 \cdot 10^{-4}$	106	48	53

Doubling the resolution going to $N = 512$ and doubling the dissipative wavenumber should be accomplished by $\nu \approx 2.8 \cdot 10^{-4}$ (for $k_\nu \sim 100 > 85 = N/6$ and $k_\varepsilon \sim 200 > 171 = N/3$). Therefore a better resolved choice is $\nu = 3.2 \cdot 10^{-4}$ (predicting $k_\varepsilon \sim 180$) and we employ $\Delta t = 1 \cdot 10^{-3}$. For this choice we find $k_\varepsilon \sim 200 > 171 = N/3$ ($k_\nu \sim 90$). Doubling our resolution for the last time ($N = 1024$) we halve the viscosity, $\nu = 1.6 \cdot 10^{-4}$, which should give dissipative scales $k_\nu \sim 151$ and $k_\varepsilon \sim 331 < 341 = N/3$. For time step we impose the CFL condition,

$$\Delta t < \frac{1}{uN} = \frac{1}{1024} = 9.77 \cdot 10^{-4}.$$

We employ $\Delta t = 5 \cdot 10^{-4}$ hoping to deal with reconnection events as large as $b = 2$. The actual scales were found to be $k_\nu \sim 155$ and $k_\varepsilon \sim 319$. The time chosen as a quasi-steady-state is $t = [50, 150]$ (see Figure 4.3). A true steady state will only be achieved when the magnetic field at $k = 1$ saturates, after a large-scale magnetic diffusion time which is given by $\tau = \frac{l^2}{\eta} \sim 15,000$. This we cannot afford to compute.

[5] $k_\nu \equiv (\frac{\langle w^2 \rangle}{\nu^2})^{\frac{1}{4}}$ and should be also be similar to the Kolmogorov dissipation scale. Experience indicates that allowing this value to be too small wastes resolution.

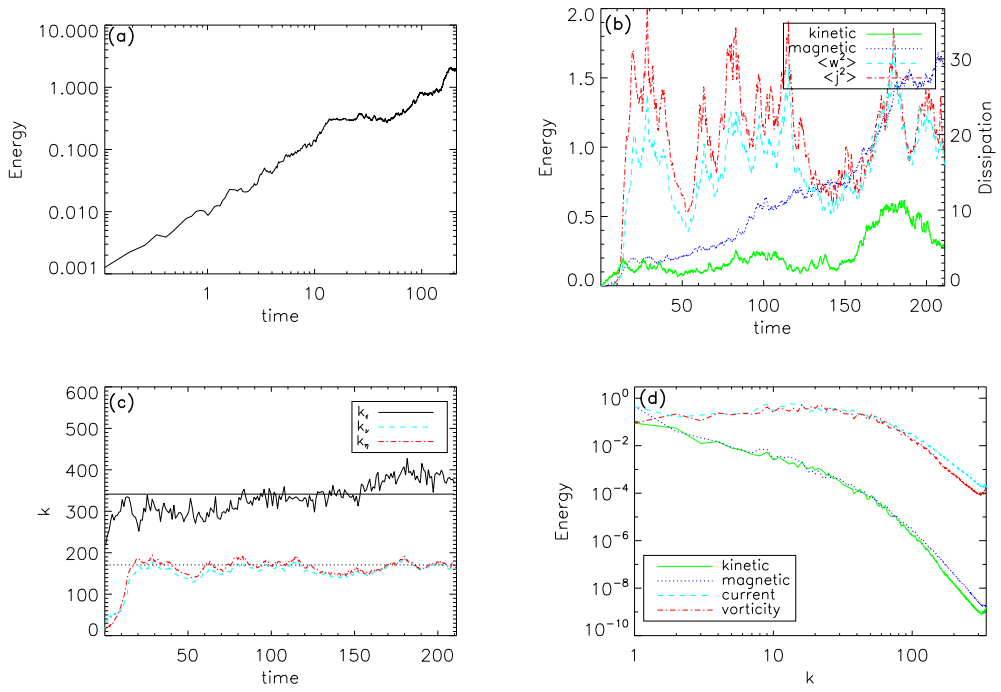

Figure 4.3: Final forced-run experiment (run d). Labels are as in Figure 4.1. Panel **(a)** shows energy versus time. Panel **(b)** shows kinetic energy, magnetic energy, average square vorticity, and average square current. Panel **(c)** shows the Kolmogorov dissipative wavenumber versus time as well as the N/3 resolution limit (solid line) and a reference line at N/6 (dotted). Panel **(d)** shows the spectra for $t = 100$.

4.4.3 Results

All experiments used in our final study are summarized in Table 4.3. In addition to the fully resolved MHD simulations, alpha model simulations are made at 1/2 and 1/4 resolutions. This corresponds to 1/4 and 1/16 the number of grid points and, hence, the same reduction in statistics. As many data points are essential for calculation of high-order structure functions, no lower resolution calculations are made. Two values of alpha are employed for both types of experiments corresponding to $12/N^{'}$ and $24/N^{'}$, where $N^{'}$ is the resolution of the MHD run.

Table 4.3: Turbulence experiments (runs a-f). Table shows experiment label, resolution, N, model parameter, α, viscosity, $\nu = \eta$, forcing, $\mathcal{F}_M, \mathcal{F}_K$, initial conditions, $u_o = b_0$, Taylor length scale, λ, Taylor Reynolds number, R_λ,† and figures depicted for all experiments.

Run	N	$\alpha \cdot N^*_{DNS}$	$\nu = \eta$	$\mathcal{F}_M$	$\mathcal{F}_K$	$u_o = b_0$	λ	R_λ	Figs.
a	2048	0 (DNS)	10^{-4}	0	0	1	.23	1500	4.4-8; 5.1-3,7-8
b	1024	12	10^{-4}	0	0	1	.26	1700	4.4-8; 5.1-2,7-8
c	512	24	10^{-4}	0	0	1	.26	1700	4.4-8; 5.1-2,7-8
d	1024	0 (DNS)	$1.6 \cdot 10^{-4}$	0.2	0.45	0	.63	1600	4.3,9-11; 5.4-6,9-12
e	512	12	$1.6 \cdot 10^{-4}$	0.2	0.45	0	.60	1300	4.3,9-11; 5.4-5,9-12
f	256	24	$1.6 \cdot 10^{-4}$	0.2	0.45	0	.54	1100	4.3,9-11; 5.4-5,9-12

†Computed at peak of the dissipation, $t \approx 6.5$, for freely decaying runs (a-c) and averaged over $t = [50, 150]$ for forced runs (d-f).
$^*\alpha^{-1} = k_{max}/2$.

4.4.3.1 Freely Decaying Turbulence

As described in §4.3, both the MHD equations, (4.2), and the LAMHD$-\alpha$ equations, (4.4), were solved on a square box of edge size 2π with periodic boundary conditions. The evolution of magnetic, E_M, and kinetic, E_K, energy versus time is shown in Fig 4.4. The upper grouping of the lines are for magnetic energy, the green dotted line is for 2048^2 DNS, the blue dashed line and the red dash-triple-dotted line are for

1024^2 and 512^2 LAMHD$-\alpha$, respectively. The lower grouping of lines are the kinetic energies, solid green for DNS, blue dash-dotted for 1024^2 alpha, and red long-dashed for 512^2 alpha. We see that the system is near equipartition and that the alpha model runs closely reproduce the time evolution of the energy. This was previously shown in [55] as was the lack of agreement between DNS and an under-resolved MHD simulation.

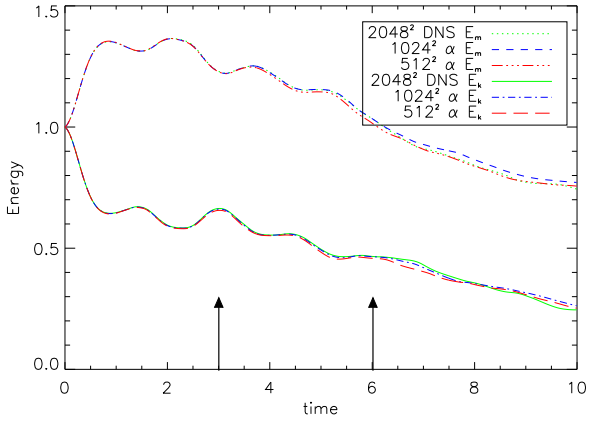

Figure 4.4: Magnetic, $E_M(t)$, and kinetic, $E_K(t)$, energies for freely decaying runs (a-c). $E_M(t)$ for 2048^2 MHD is the green dotted line, for 1024^2 LAMHD$-\alpha$ is the blue dashed line, and for 512^2 LAMHD$-\alpha$ is the red dash-triple-dotted line. $E_K(t)$ for 2048^2 MHD is the green solid line, for 1024^2 α is the blue dash-dot line, and for 512^2 α is the red long-dashes line. Note that the different solutions depart after the enstrophies have reached their peak (see Figure 4.5).

In Figure 4.5, the time evolution of the total square current, $\langle j^2 \rangle \sim \Omega_M$, and total square-vorticity, $\langle w^2 \rangle \sim \Omega$, are shown. It is seen that the alpha model reproduces both the time of maximum dissipation and the order of magnitude of the dissipation. Next, we compare averaged spectra from $t = 3$ up to $t = 6$, the time for which the energies are oscillating and prior to maximum dissipation (see Figure 4.5). We note that for large wavelength component behavior, up to $\approx k_\alpha$, both resolutions of the alpha model accurately reproduce the omni-directional spectra for the magnetic and kinetic energies as expected [55][6] (see Figure 4.6). An inertial range can be identified for all simulations

[6] Reference [55] also finds that under-resolved MHD simulations have inaccurate spectra.

with an extent of approximately one decade in Fourier space, from $k \approx 3$ up to $k \approx 30$. As [55] we also find that the spectral details at small scales are not accurate. Note that $k_\alpha \equiv \frac{1}{\alpha} \approx 171$ for the 1024^2 run and $k_\alpha \approx 85$ for the 512^2 run. These wavenumbers are indicated with vertical lines in the figures. Hereafter we use the following conventions for line plots. The solid green line represents the DNS (MHD) run, the dotted blue and the dashed red lines represent the LAMHD$-\alpha$ runs at 1/2 and 1/4 resolution, respectively. As previously mentioned, for $k > k_\alpha$ a steeper energy spectrum is predicted [22] and it is this very aspect of the alpha model that makes lower resolution simulations possible. Note, however, a marked better agreement with the MHD run for the kinetic energy spectrum.

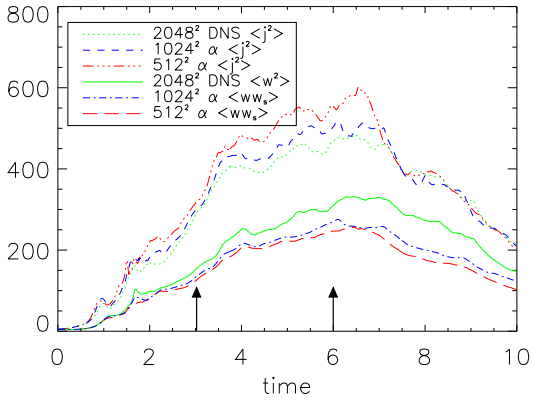

Figure 4.5: Average square-current, $\langle j^2 \rangle$, and average square-vorticity, $\langle w^2 \rangle$, for freely decaying runs (a-c). $\langle j^2 \rangle$ for 2048^2 MHD is the green dotted line, for 1024^2 LAMHD$-\alpha$ is the blue dashed line, and for 512^2 LAMHD$-\alpha$ is the red dash-triple-dotted line. $\langle w^2 \rangle$ for 2048^2 MHD is the green solid line, for 1024^2 α is the blue dash-dot line, and for 512^2 α is the red long-dashes line.

In the induction equation for the smoothed magnetic field (3.44b) the Ohmic dissipation term is $\eta \nabla^2 \boldsymbol{b} = \eta \nabla^2 \boldsymbol{b}_s - \eta \alpha^2 \nabla^4 \boldsymbol{b}_s$ and thus is hyper-viscosity-like. This explains the faster drop in the magnetic energy spectrum. For this spectrum we note that for the 512^2 run, the spectrum is indistinguishable from DNS up to $k\alpha \approx 0.7$ and

for 1024^2 up to ≈ 0.6. As the smoothing is proportional to the square of $k\alpha$, neither of these values is surprising. For the kinetic spectrum on the other hand, the 512^2 remains indistinguishable beyond $k\alpha = 1$ and the 1024^2 run only begins to deviate at $k\alpha \approx 0.8$. Both LAMHD$-\alpha$ spectra for kinetic and magnetic energy behave as expected and reproduce the large-scale spectra accurately.

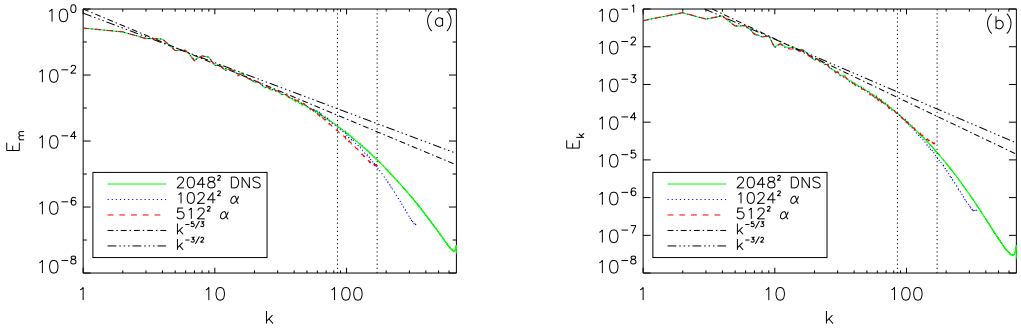

Figure 4.6: Spectra averaged from $t = 3$ up to $t = 6$ for freely decaying turbulence (runs a-c). 2048^2 MHD is the solid green line, 1024^2 LAMHD$-\alpha$ is the dotted blue line, 512^2 LAMHD$-\alpha$ is the dashed red line, $k^{-\frac{5}{3}}$ (K41) is the dash-dot-dashed line, and $k^{-\frac{3}{2}}$ (IK) is the dash-triple-dotted line. The K41 and IK slopes are shown as a reference. Vertical lines indicate the wavenumbers corresponding to the lenghts α for the 1024^2 and 512^2 simulations. Panel **(a)** is magnetic energy, E_m, versus k and panel **(b)** is kinetic energy, E_k, versus k.

Similarly, plots of the stream function, ψ, and vector potential, a_z, for $t = 4.5$ (shown in Figure 4.7), illustrate that the over-all structure of the MHD flow is preserved by LAMHD$-\alpha$. In these plots bright yellow represents positive vector potential (or stream function) and counter-clockwise rotation of the magnetic field (velocity) while light pink represents negative values and clockwise rotations. Upon close enough inspection, you might convince yourself that there are some small-scale differences in the alpha model simulations. The current (and hence the Ohmic dissipation) as well as the vorticity are shown in Figure 4.8. Here pink and white pixels indicate current (vorticity) coming out of the page while black and green pixels indicate current (vorticity) going into the page. The main feature of these plots are the (mostly pink) current sheets. The

color scale masks all but the most strong negative current sheets. Small-scale differences are more easily observed in these plots as they more emphasize the small-scale features of the flow.

4.4.3.2 Forced Turbulence

As previously described, we consider forced turbulence with $\nu = \eta = 1.6 \cdot 10^{-4}$ in three simulations: DNS (MHD) with 1024^2 grid points and two LAMHD$-\alpha$ simulations with 512^2 grid points and $\alpha_K = \alpha_M = 6/512$ and 256^2 grid points and $\alpha_K = \alpha_M = 6/256$. Both the momentum and the vector potential equations were forced. The expression of the external forces were loaded in the Fourier region between $k = 1$ and $k = 2$ and the phases were changed randomly with a correlation time $\Delta\tau = 5 \cdot 10^{-2}$. Averaged over space, the amplitudes of the external forces were held constant to $\mathcal{F}_M = 0.2$ in the vector potential equation and $\mathcal{F}_K = 0.45$ in the momentum equation. The time evolution of the fields is shown in Figure 4.9. Here the solid green line is for the 1024^2 DNS and the dotted blue and dashed green lines are for the 512^2 and 256^2 LAMHD-α, respectively. The alpha models track well the DNS energies up to $t \approx 70$. It is not surprising both because of sensitive dependence on initial conditions (a property of chaotic dynamics) and because of the alpha model's loss of the location of specific features that under the influence of external forcing the LAMHD$-\alpha$ simulations do not continue to track the DNS solution for all times. It is rather the statistical features of the flow that we wish to compare. The turbulent quasi-steady-state $\Omega \approx \varepsilon$ considered from $t = [50, 150]$ endures for 20 turnover times, $\tau \sim 5$. See Figure 4.10 where $\frac{dE}{dt} = \varepsilon - \nu\langle w^2\rangle - \eta\langle j^2\rangle$ has the average $\langle|\langle\frac{dE}{dt}\rangle_{\Delta t=5}|\rangle \approx 0.004$ for the MHD and 512^2 alpha run and an average of about 0.003 for the 256^2 LAMHD$-\alpha$ run in the range $t = [50, 150]$. This imbalance is nearly twice as much before $t = 50$ and after $t = 150$. Over this approximate steady state, 20 snap shots of the field were taken. Average omni-directional spectra for magnetic and kinetic energies over these snapshots are shown

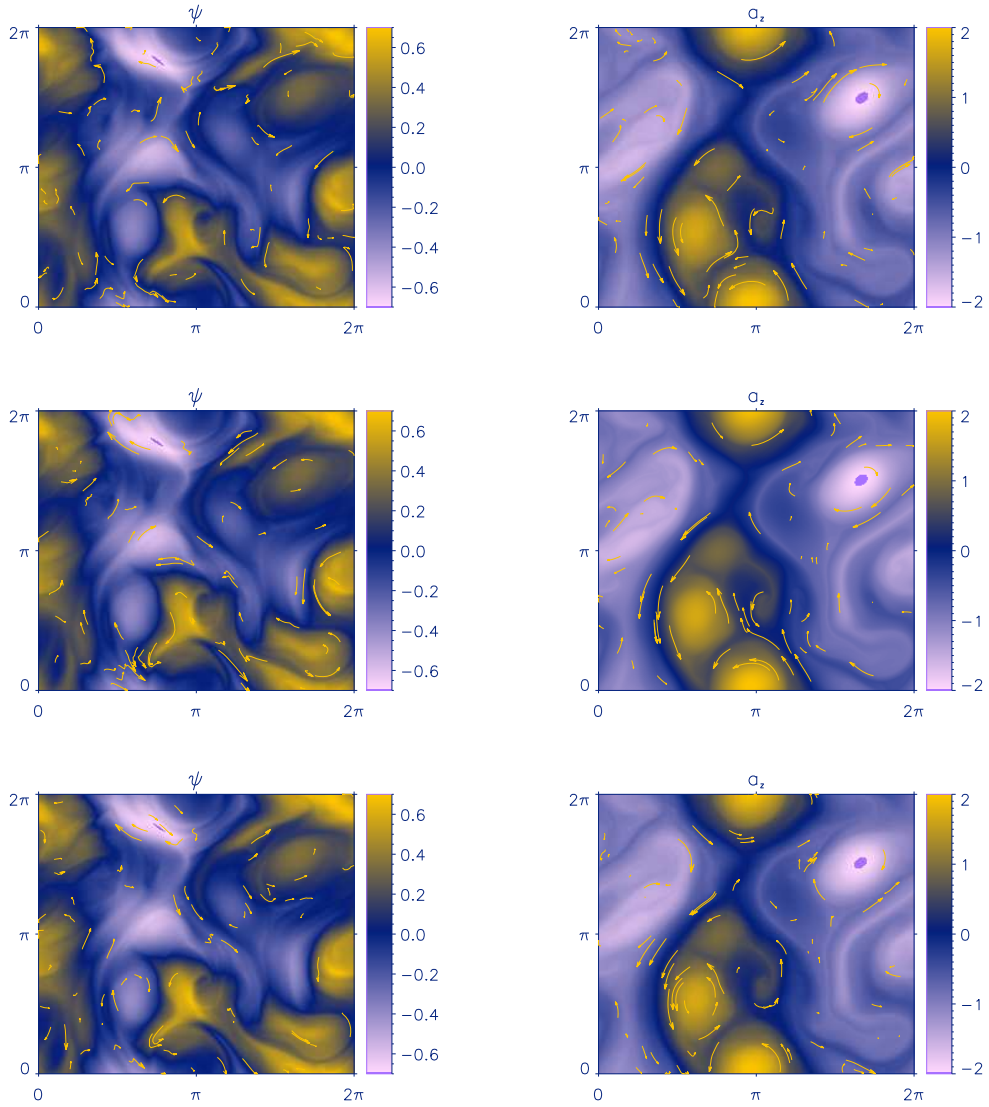

Figure 4.7: Stream function, ψ, and vector potential, a_z for freely decaying turbulence (runs a-c). Stream function is shown in the left column (super-imposed arrows show some velocity vectors). Vector potential is shown in the right column (super-imposed arrows show some magnetic field vectors). Snapshot is for $t = 4.5$. Yellow indicates positive vector potential (stream function) and counter-clockwise magnetic field (velocity) while light pink indicates negative values and clockwise flow. Top row is the 2048^2 DNS (MHD) run while the second and third rows are 1024^2 and 512^2 LAMHD$-\alpha$, respectively.

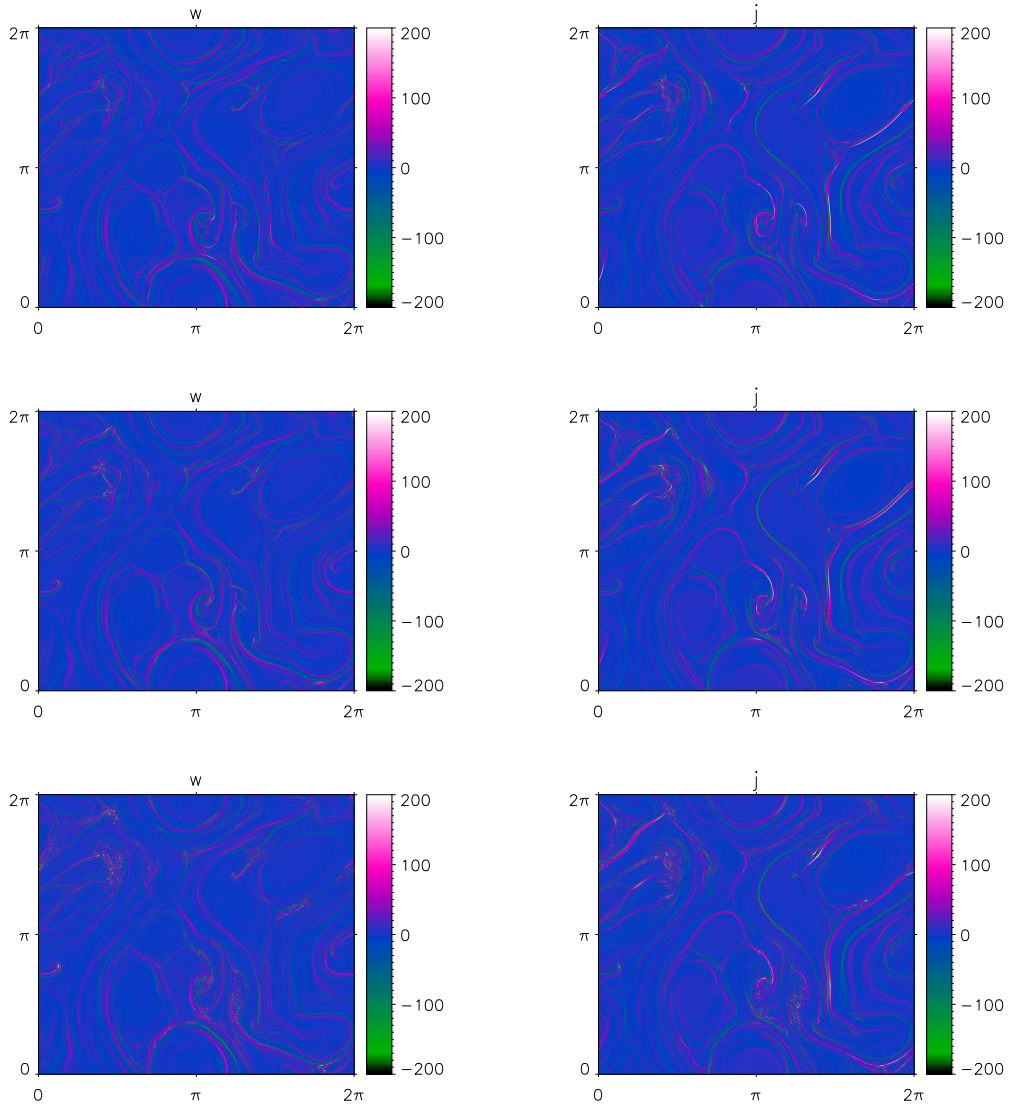

Figure 4.8: Electric current, j, and voriticity, w, for freely decaying turbulence (runs a-c). Vorticity is shown in the left column and current is shown in the right column. Snapshot is for $t = 4.5$. Pink/white indicates current/vorticity coming out of the page and green/black, into the page. Top row is the 2048^2 DNS (MHD) run while the second and third rows are 1024^2 and 512^2 LAMHD$-\alpha$, respectively.

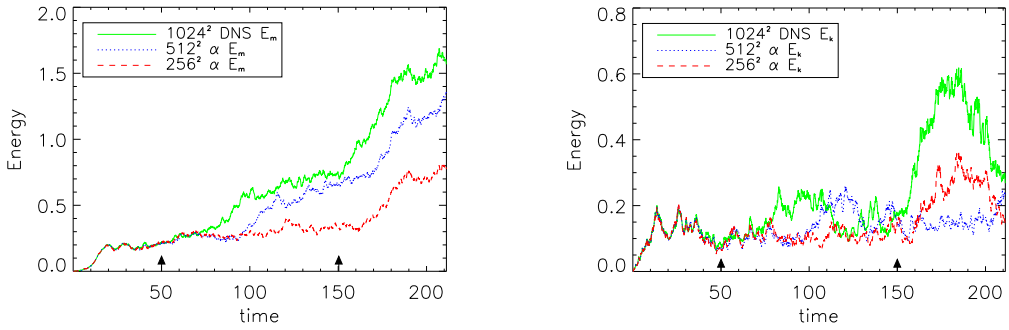

Figure 4.9: Left: Magnetic energy, $E_M(t)$, and Right: kinetic energy, $E_K(t)$, for forced turbulence (runs d-f). 1024^2 DNS is the solid green line, for 512^2 LAMHD$-\alpha$ is the dotted blue line, and for 256^2 LAMHD$-\alpha$ is the dashed red line. Eddy turnover time, $\tau \sim 5$.

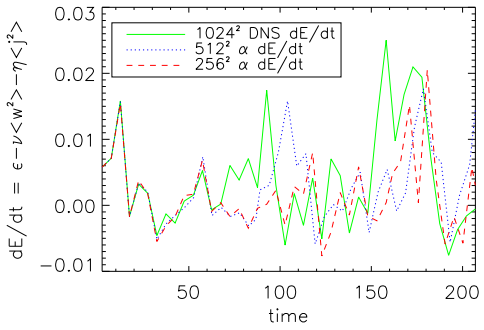

Figure 4.10: Energy rate of change for forced turbulence (runs d-f), $\frac{dE}{dt} = \varepsilon - \nu\langle w^2\rangle - \eta\langle j^2\rangle$. As the correlation time for the forcing, $\Delta\tau = 5 \cdot 10^{-2}$, is very short, ε is highly varying, and averages over time increments of $\Delta t = 5$ are taken before plotting. Labels are as in Figure 4.9.

in Fig. 4.11. Spectra for the kinetic energies are normalized to the average kinetic energy of the DNS run. The alpha model reproduces the feature of MHD turbulence that the magnetic excitations become concentrated at the largest scale allowed by the boundary conditions ($k_{min} = 1$),[7] but there is a small disagreement in the values at $k = 1$.[55] This, unfortunately, makes normalization of the magnetic energy spectrum problematic. Instead, the magnetic spectra are presented "as is." For the kinetic energy spectra, we have excellent agreement up to $k\alpha \approx 1$ and for the magnetic energy spectra up to perhaps $k\alpha \approx \frac{1}{2}$. These results, then, differ little from the freely decaying case and confirm that LAMHD$-\alpha$ reproduces the large-wavelength component behavior of turbulent MHD.

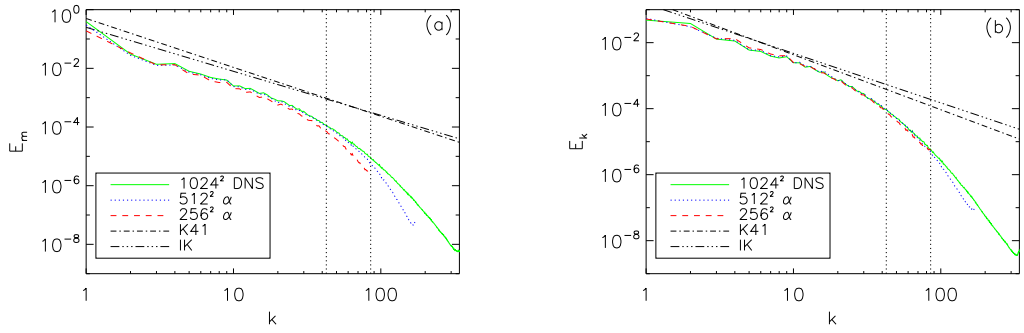

Figure 4.11: Averaged spectra from $t = 50$ up to $t = 150$ for forced turbulence (runs d-f). Energy labels are as in Figure 4.9. $k^{-\frac{5}{3}}$ (K41) is the dash-dot-dashed line, and $k^{-\frac{3}{2}}$ (IK) is the dash-dot-dot-dot-dashed line. The K41 and IK slopes are shown as reference. The vertical lines indicate the wavenumber corresponding to the lengths α for the LAMHD$-\alpha$ simulations. Panel **(a)** is magnetic energy, E_m, versus k and panel **(b)** is kinetic energy, E_k, normalized to average kinetic energy of the MHD run versus k.

[7] Because of the inverse cascade of vector potential, we observe a sharp maximum in the magnetic energy spectrum at $k = 1$.

Chapter 5

Analysis of Intermittency

The alpha model has been studied extensively for the Navier-Stokes case (see §3.4 for an introduction and references) but very little for MHD in the non-dissipative case [36] and in the turbulent case [55, 54, 69]. While the results of [55] suggest intermittency for 2D LAMHD-α, until now there has been no direct study of intermittency in high order statistical moments of the velocity and magnetic fields, such as the structure functions. Intermittency is associated with strong events occurring more often than for Gaussian statistics (see §3.3). From a theoretical standpoint, intermittency can be considered the essential element of turbulence [56]. It is a phenomenon that is highly localized both in space and time. It therefore requires that any numerical simulation used to study it to possess high resolution. It is for this reason, as shown in §4, we have chosen 2D MHD simulations as our test-bed for the alpha model's ability to capture the intermittent aspect of turbulence.

The intermittency of large eddy simulation (LES) methods has been studied for 3D non-conductive fluids [13] with a Taylor Reynolds number, $R_\lambda = 150$. They find the intermittency of the unresolved subgrid scale dissipation to be slightly more than the intermittency measured by the longitudinal velocity structure functions. They also determine that their Reynolds number is insufficient for a determination of third-order scaling and so resolve to measure relative exponents for the subgrid scale dissipation. For these, they find that the Smagorinsky model, the volume-averaged dynamic model,

and the similarity model perform fairly well (*e.g.* the error in the exponent for $p = 7$ is less than 7%). The constant eddy-viscosity and spectral eddy-viscosity models underestimate intermittency beyond $p = 4$ (compared to DNS) while the local and clipped dynamic Smagorinsky models strongly overestimate the intermittency beyond $p = 4$. Reference [52] also studies 3D Navier-Stokes turbulence (for $R_\lambda = 130$) with an eddy-viscosity LES designed to enforce the same k^{-3} energy spectrum as the alpha model [18, 22] but beyond the inflection point, k_c of the energy flux. They also find that the scaling is well reproduced.

Our 2D MHD tests are able to exhibit a substantially larger Reynolds number ($R_\lambda \sim 1500$). We utilize a freely decaying turbulent direct numerical simulation (DNS) of the MHD equations (linear resolution, N=2048, $\nu = \eta = 10^{-4}$) as well as LAMHD$-\alpha$ runs at 1/2 (N=1024, $\alpha_K = \alpha_M = 6/1024$) and 1/4 (N=512, $\alpha_K = \alpha_M = 6/512$) resolutions. Note that due to dealiasing in the simulations, the maximum resolved wavenumber is $k_{max} = N/3$. Identical initial conditions, dissipation, and time stepping are used in all three runs. We also study a forced turbulent DNS (MHD) simulation (N=1024, $\nu = \eta = 1.6 \cdot 10^{-4}$) and LAMHD$-\alpha$ runs at 1/2 (N=512, $\alpha_K = \alpha_M = 6/512$) and 1/4 (N=256, $\alpha_K = \alpha_M = 6/256$) resolutions. Here also, identical forcing, dissipation, and time stepping are employed for all three runs. In §4.4.3 we presented the energy evolution of all six experiments, average spectra, and a few snapshots of the fields. As [55], we concluded that LAMHD$-\alpha$ reproduces the large-wavelength component behavior of turbulent MHD. In §3.3, we introduced the structure functions over the inertial range as a measure of intermittency. In this chapter we present our final results of intermittency in the alpha model studied through the structure functions.

5.1 Finding the Inertial Range

We must start by determining the inertial range as discussed in §3.2. It is there that the scaling of the structure functions will give a measure of intermittency.

5.1.1 Freely Decaying

There are two energy spectra considered for 2D MHD. One is based on the phenomenology developed by Kolmogorov [46, 47, 48], $E(k) \sim k^{-5/3}$, (hereafter K41) and the other by Iroshnikov [45] and Kraichnan [50], $E(k) \sim k^{-3/2}$, (hereafter IK).[1] The principle difference being that IK takes into account the non-local (in Fourier space) interactions due to Alfvén waves. This work does not aim to be part of the ongoing debate concerning what is the actual inertial range spectrum for 2D MHD. Rather, we compensate our spectra by multiplication both with $k^{5/3}$ and $k^{3/2}$ in Figure 5.1 and note that for the correct compensation, we expect a flat spectrum in the inertial range. A power law of $E(k) \sim k^{-5/3}$ is then observed for $k \approx [5, 30]$. One can also identify an inertial range assuming the IK spectrum, albeit for a shorter interval.

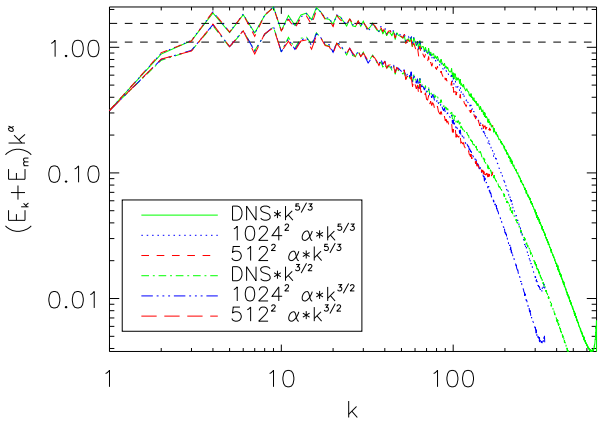

Figure 5.1: Compensated spectra averaged from t=3 up to t=6 for freely decaying turbulence (runs a-c). Upper set of lines are compensated by $k^{5/3}$ for 2048^2 MHD (green solid), 1024^2 LAMHD$-\alpha$ (blue dotted), and 512^2 LAMHD$-\alpha$ (red dashed). A power law is observed for $k \approx [5, 30]$. Lower set of lines are compensated by $k^{3/2}$ for 2048^2 MHD (green dash-dotted), 1024^2 LAMHD$-\alpha$ (blue dash-triple-dotted), and 512^2 LAMHD$-\alpha$ (red long-dashed). A power law is observed for $k \approx [5, 20)$. Horizontal dashed lines are shown for reference.

Following the extended self-similarity hypothesis of [4, 5], references [66, 68] sug-

[1] Recall from §3.2, that k is the wavenumber and $E(k)$ is the spectral energy density.

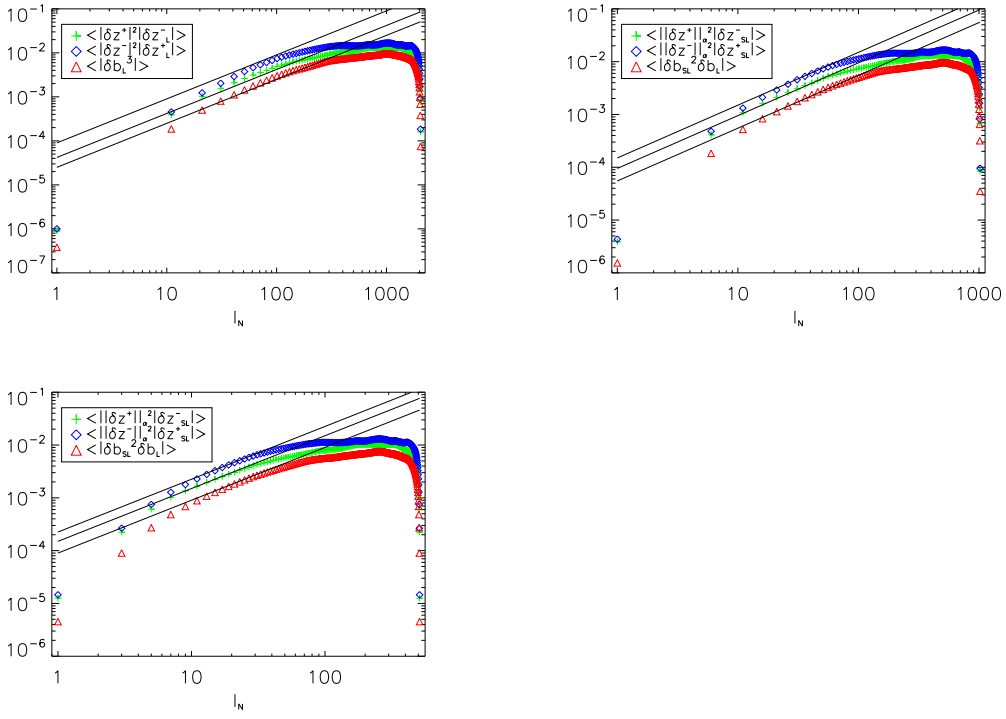

Figure 5.2: Extended self similarity range for freely decaying turbulence at $t = 4$ (runs a-c). Upper left plot is for the 2048^2 MHD (run a). $L^+(l) \equiv \langle|\delta z^-_L||\delta z^+|^2\rangle$ is shown with green pluses, $L^-(l)$ with blue diamonds, and $\langle|\delta b_L|^3\rangle$ with red triangles. The upper right and lower plots are for the 1024^2 and the 512^2 LAMHD$-\alpha$ (runs b and c), respectively. Here, $L^\pm_s(l) \equiv \langle|\delta z^\mp_{s_L}|||\delta z^\pm||^2_\alpha\rangle$ and $\langle|\delta b^2_{s_L}\delta b_L|\rangle$ are used instead, corresponding to the von Kármán-Howarth theorem for LAMHD-α. In all cases for the better behaved of $L^\pm$, we observe linear scaling for $l = 2\pi l_N/N \approx [0.1, 0.3]$ or $k \approx [20, 70]$.

gest that the third-order structure functions may provide a better independent variable (opposed to length) against which to determine the scaling exponents of high-order structure functions for MHD. This extended power-law-range analysis instead of using the wave-number range where $E(k) \propto k^{\alpha}$ is valid, utilizes the longer range where the third-order structure function is proportional to length. In [66],

$$\langle \left(\delta z_L^{\pm}(\boldsymbol{l})\right)^2 \delta z_L^{\mp}(\boldsymbol{l})\rangle - 2\langle z_L^{\pm}(\boldsymbol{x}) z_L^{\pm}(\boldsymbol{x}) z_L^{\mp}(\boldsymbol{x}')\rangle = -C_d \varepsilon^{\pm} l \tag{5.1}$$

is derived similar to the von Kármán-Howarth theorem but for an incompressible, non-helical MHD flow under the assumptions of full isotropy, homogeneity, and incompressibility. Here $\boldsymbol{z}^{\pm} = \boldsymbol{u} \pm \boldsymbol{b}$ are the Elsässer fields for which the MHD equations (2.27) take the symmetric form

$$\begin{aligned} \partial_t \boldsymbol{z}^{\pm} + \boldsymbol{z}^{\mp} \cdot \boldsymbol{\nabla} \boldsymbol{z}^{\pm} &= -\boldsymbol{\nabla} p_* + \nu_+ \nabla^2 \boldsymbol{z}^{\pm} + \nu_- \nabla^2 \boldsymbol{z}^{\mp} \\ \boldsymbol{\nabla} \cdot \boldsymbol{z}^{\pm} &= 0, \end{aligned} \tag{5.2}$$

where $p_* = p + b^2/2$ is the total pressure, $\nu_{\pm} = (\nu \pm \eta)/2$, ν is the viscosity, and η is the magnetic diffusivity. As introduced in §3.3, the increment of a field $\boldsymbol{f}$ is defined as $\boldsymbol{\delta f}(\boldsymbol{l}) = \boldsymbol{f}(\boldsymbol{x} + \boldsymbol{l}) - \boldsymbol{f}(\boldsymbol{x})$, $\boldsymbol{x}' \equiv \boldsymbol{x} + \boldsymbol{l}$, and the longitudinal component of the increment is $\delta f_L(\boldsymbol{l}) = \boldsymbol{\delta f}(\boldsymbol{l}) \cdot \boldsymbol{l}/l$. Likewise $z_L^+(\boldsymbol{x})$ would be the longitudinal component of $\boldsymbol{z}^+$ evaluated at $\boldsymbol{x}$, $z_L^+(\boldsymbol{x}) = \boldsymbol{z}^+(\boldsymbol{x}) \cdot \boldsymbol{l}/l$. The energy dissipation rates are ε^+ and ε^- for $\frac{1}{2}(z^+)^2$ and $\frac{1}{2}(z^-)^2$, respectively. Finally, C_d is a constant and angle brackets indicate spatial averages. Under the assumption of equipartition, the two-point third-order correlation tensor disappears simplifying (5.1) to

$$\langle \left(\delta z_L^{\pm}(\boldsymbol{l})\right)^2 \delta z_L^{\mp}(\boldsymbol{l})\rangle = -C_d \varepsilon^{\pm} l, \tag{5.3}$$

or, for a magnetically dominated flow,

$$\langle \delta {b_L}^3(\boldsymbol{l})\rangle = \frac{4}{5} \varepsilon_C l, \tag{5.4}$$

where ε_C is the dissipation rate of the cross-helicity. In the hydrodynamic limit ($b \to 0$) the Kolmogorov four-fifths law (3.20) is recovered. Simpler scaling laws than for the third-order longitudinal structure functions can be derived under the assumption of a unit magnetic Prandtl number, $\nu = \eta$,[2] instead of assuming equipartition [68]

$$\langle \delta z_L^{\mp} |\delta z^{\pm}|^2 \rangle = -\frac{4}{d}\varepsilon^{\pm} l, \tag{5.5}$$

where $|\delta z^{\pm}|^2 = (\delta z_L^{\pm})^2 + (\delta z_T^{\pm})^2$, $\delta z_T^{\pm}$ is the transverse increment, and d is the space dimension. Or, for a magnetically dominated flow,

$$\langle \delta b_L |\delta b|^2 \rangle \propto l. \tag{5.6}$$

Here we have removed the implicit $\boldsymbol{l}$ dependence from our notation for simplicity. These results for the third-order structure functions are exact and can be used to compute more accurate anomalous scaling exponents of structure functions of higher order. Due to the cancellation problems with having limited statistics, we employ instead absolute values

$$L^{\pm}(l) \equiv \langle |\delta z_L^{\mp}||\delta z^{\pm}|^2 \rangle \propto l, \tag{5.7}$$

which in practice is also found to hold true. A longer scaling range is observed for these quantities as seen in Figure 5.2. Here $L^+(l)$ is shown with green pluses, $L^-(l)$ with blue diamonds, and $\langle |\delta b_L|^3 \rangle$ with red triangles. For the LAMHD$-\alpha$ runs, $L_s^{\pm}(l) \equiv \langle |\delta z_{s_L}^{\mp}|||\delta z^{\pm}||_{\alpha}^2 \rangle$, where $||\delta z^{+}||_{\alpha}^2 \equiv |\delta {z_L}^{+} \delta z_{s_L}^{+}| + |\delta {z_T}^{+} \delta z_{s_T}^{+}|$, and $\langle |\delta b_{s_L}^2 \delta b_L| \rangle$ are plotted instead. This corresponds to the von Kármán-Howarth theorem for LAMHD$-\alpha$ as derived in [56] which contains two smoothed and one unsmoothed field. In general, second-order quantities in LAMHD$-\alpha$ involve one smoothed and one unsmoothed field and third-order quantities involve two smoothed and one unsmoothed. The longest range of linear-in-length scaling is found for $L^+(l)$ ($L_s^+(l)$) corresponding to $l = 2\pi l_N/N \approx [0.1, 0.3]$ or $k \approx [20, 70]$. The scaling versus L^+ in this range will give much better statistics than for the scaling versus l in the inertial range as demonstrated in computing the fourth-order

[2] This is the case for our experiments.

scaling exponent for $\boldsymbol{z}^-$ from $S_4^- \equiv \langle|\delta z^-(l)|^4\rangle$ (see Figure 5.3). Here we plot S_4^- versus l and versus L^+ for all length scales for the freely-decaying 2048^2 DNS run at $t = 4$. Just outside the inertial range $S_4^-(l)$ has pronounced "wiggles" away from the power-law. These increase the error in the computation of the scaling exponent, $S_4^- \sim l^{\zeta_4^-}$, $\zeta_4^- = 0.69 \pm 0.11$, a feature that will be also observed for higher order moments. Deviation from the power-law, $S_4^- \sim (L^+)^{\xi_4^-}$ just outside the extended self-similarity range is more gradual allowing for a more accurate estimation, $\xi_4^- = 1.24 \pm 0.07$. Both estimates, however, are made for a single snapshot of the field (only $4 \cdot 10^6$ data values). For LAMHD$-\alpha$ the statistics are even more limited ($\approx 3 \cdot 10^5$ data values for 512^2). This situation can be improved by analyzing instead a forced turbulent run where we can average over several snapshots during a quasi steady-state.

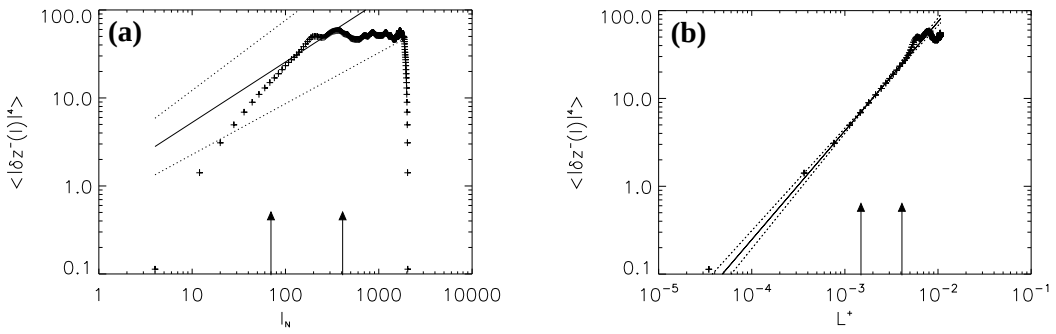

Figure 5.3: Determination of scaling exponent of S_4^- in the inertial range and in the extended self-similarity hypothesis for run a at $t = 4$ (both ranges indicated by arrows). Left, for inertial range $k = [5, 30]$, $S_4^- \equiv \langle|\delta z^-(l)|^4\rangle \sim l^{\zeta_4^-}$. ζ_4^- is 0.69 ± 0.11. Right, for extended self-similarity hypothesis $k = [20, 70]$ $S_4^- \equiv \langle|\delta z^-(l)|^4\rangle \sim L^{+\xi_4^-}$. ξ_4^- is 1.24 ± 0.07. Solid lines indicate least-squares fits in the selected intervals and the dotted lines indicate uncertainties in the slopes. The two exponents should be the same, but it is obvious from **(a)** that no scaling is apparent.

5.1.2 Forced

Compensated spectra for the forced runs averaged over $t = [50, 150]$ are shown in Figure 5.4. A power law is observed for $k \approx [4, 20]$ for the DNS and both LAMHD$-\alpha$ runs. An extended self-similarity analysis (Figure 5.5) indicates a range $k \approx [3, 20]$. Due to the inverse cascade of square vector potential in 2D MHD, however, magnetic energy piles up at the longest wavelengths, $k = 1, 2, 3 \ldots$. This can be seen clearly by comparison of Figures 5.1 and 5.4. The proximity (in Fourier space) of both this affect and the forcing band can adversely affect the estimation of the scaling exponents. Therefore, a more conservative range, $k = [10, 20]$, is employed. As we concluded in §4.4.3.2, both because of sensitive dependence on initial conditions and because of the alpha model's loss of the location of specific features, LAMHD$-\alpha$ forced simulations do not track the time evolution of the energy (see Figure 4.9). For this reason, each experiment might have the onset of large-scale self organization of the magnetic field by the inverse cascade of square vector potential (and, hence, the end of the quasi steady-state) or an event at a different times. To take this into account, we take apart the time domain for all three experiments and choose for each a time range as quasi-steady-state.

The scaling exponents, ξ_p^+ where $S_p^+ \equiv \langle |\delta z^+(l)|^p \rangle \sim L^{+\xi_p^+}$, versus p for various time intervals are plotted in Figure 5.6. The analysis of such plots is postponed until the next section. At early times, the system is still dominated by the injection of energy and is not turbulent. Later, due to the inverse cascade of vector potential, the time histories of total and magnetic energy show bursts where the magnetic energy at $k = 1$ (and as a result the total energy) suddenly increases. The growth of the $k = 1$ mode is only limited by the large scale diffusion time ($\tau \sim l^2/\eta \sim \pi^2/\eta \sim 15,000$). During these events the scaling is changed (as also the spectrum is transiently changed), and it takes a lot of statistics to compensate. Ideally, we should wait for a time of the order τ to reach a steady state at all scales. Since we are interested, however, in the statistics in

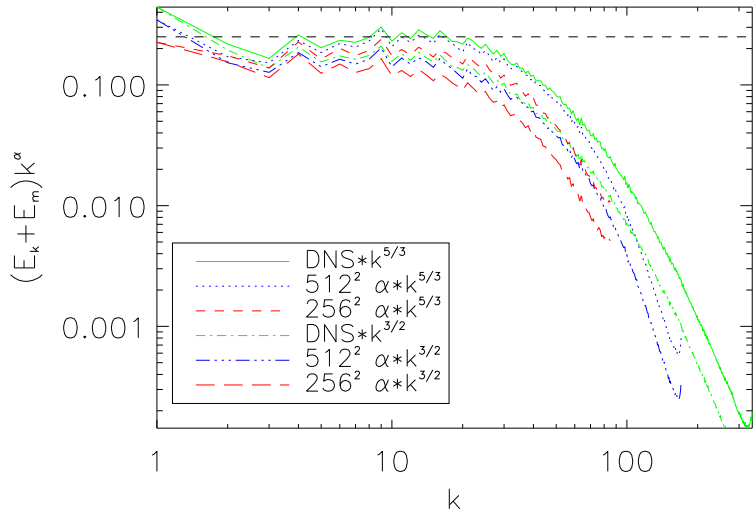

Figure 5.4: Compensated averaged spectra from $t = 50$ up to $t = 150$ for forced turbulence(runs d-f). Upper set of lines are compensated by $k^{5/3}$ for 1024^2 MHD (green solid), 512^2 LAMHD$-\alpha$ (blue dotted), and 256^2 LAMHD$-\alpha$ (red dashed). A power law is observed for $k \approx [4, 20]$. Lower set of lines are compensated by $k^{3/2}$ for 1024^2 MHD (green dash-dotted), 512^2 LAMHD$-\alpha$ (blue dash-triple-dotted), and 256^2 LAMHD$-\alpha$ (red long-dashed). A power law is observed for $k \approx [5, 20)$. A horizontal dashed line is shown for reference.

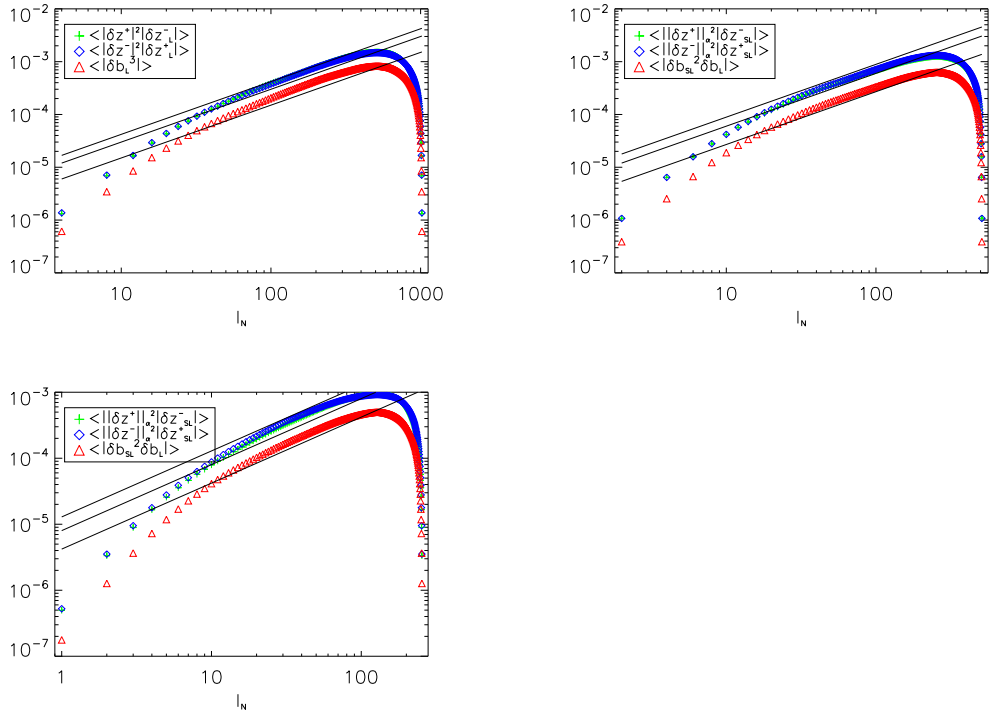

Figure 5.5: Extended self similarity range for forced turbulence for $t = [50, 150]$ (runs d-f). Upper left plot is for the 1024^2 MHD (run d). $L^+(l)$ is shown with green pluses, $L^-(l)$ with blue diamonds, and $\langle|\delta b_L|^3\rangle$ with red triangles. The upper right and lower plots are for the 512^2 and the 256^2 LAMHD$-\alpha$ (runs e and f), respectively. Here, $L^\pm_s(l) \equiv \langle|\delta z^\mp_{s_L}|||\delta z^\pm||^2_\alpha\rangle$ and $\langle|\delta b^2_{s_L}\delta b_L|\rangle$ are used instead corresponding to the von Kármán-Howarth theorem for LAMHD-α. In all cases 5 we observe linear scaling for $l = 2\pi l_N/N \approx [0.3, 2]$ or $k \approx [3, 20]$.

the inertial range, we will carry our analysis in one of the intermediate pseudo-steady states where the energy is approximately constant. When an interval of time where the energy at $k = 1$ grows is included, the system is evolving and not in a steady state, and the scaling is changed. This can be observed in the figure for the earliest and latest times plotted. For this reason, we choose to analyze the 1024^2 DNS run for $t = [50, 150]$ in the following section. A similar analysis indicates $t = [50, 180]$ for the 512^2 LAMHD$-\alpha$ and $t = [50, 150]$ for the 256^2 run.

5.2 Anomalous Scaling

One way of viewing self-similarity is that the eddy cascade is space-filling as it transfers energy from larger to smaller scales [24]. If this is not so, there are gaps between the eddies, some parts of the flow at a given time are extremely active while others are relatively motionless, and the flow is intermittent. Turbulent scales are not self-similar but become increasingly intermittent as the scale size decreases. As motivated in §3.3, from the increment of a vector field $\boldsymbol{f}$ we define the structure function of order p as $S_p^f(l) \equiv \langle |\delta f|^p \rangle$. If the field is self-similar, $\delta f(l \cdot x) = l^h \delta f(x)$ (in one dimension) for some scaling exponent h. As previously shown, we find $S_p^f \sim l^{\zeta_p^f}$ where $\zeta_p^f = h \cdot p$. It is this linear behavior of the scaling exponent that is the hallmark of self-similarity. Conversely, nonlinear dependence on p of the scaling exponents is the signature of intermittency. The more intermittent the turbulence, the greater the deviation from a straight line. From the von Kármán-Howarth theorem for Navier-Stokes, Kolmogorov [46] derives his semi-famous four-fifths law,

$$\langle (\delta u_L(l))^3 \rangle = -\frac{4}{5} \varepsilon l, \tag{5.8}$$

for the third-order longitudinal structure function of the velocity, the energy dissipation rate ε, and length l in the inertial range. This sets the value of h at $1/3$ and hence, assuming self-similarity, we arrive at $\zeta_p^u = \frac{p}{3}$ (hereafter K41). The Elsässer fields,

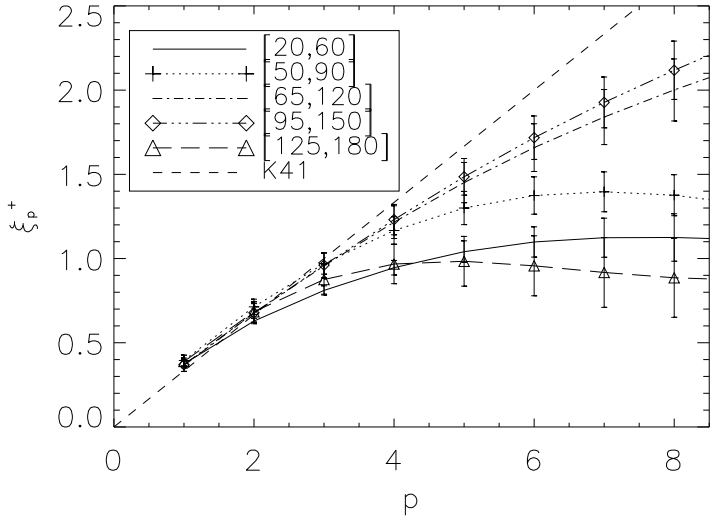

Figure 5.6: Scaling exponents for forced turbulence (run d). Scaling exponents, ξ_p^+ where $S_p^+ \equiv \langle |\delta z^+(l)|^p \rangle \sim L^{+\xi_p^+}$, versus p for $t = [20, 60]$ (solid line), $t = [50, 90]$ (pluses/dotted line), $t = [65, 120]$ (dash-dotted line), $t = [95, 150]$ (diamonds/dash-triple-dotted line), and $t = [125, 180]$ (triangles/long-dashed line). All plots are for the 1024^2 DNS run. The $\xi_p^v = p/3$ K41 line is shown for reference only. See Figure 4.3 for plots of temporal data.

$\boldsymbol{z}^{\pm}$, are the basic dynamical quantities of incompressible MHD. Taking into account that Elsässer field eddies travel in opposite directions along a quasi-background magnetic field, there is a reduced transfer of energy to small scales and Iroshnikov [45] and Kraichnan [50] conclude $\zeta_p^{\pm} = \frac{p}{4}$ (hereafter IK).

As follows from the von-Kármán-Howarth equation for LAMHD$-\alpha$ [56] and the invariants for both MHD and LAMHD$-\alpha$ (see §4.2), when making comparisons we substitute the H^1_α norm, $\langle ||u||^2_\alpha \rangle = \langle |\boldsymbol{u}\cdot\boldsymbol{u}_s| \rangle$ [38, 39], for the regular L^2 norm, $\langle |u|^2 \rangle = \langle |\boldsymbol{u}\cdot\boldsymbol{u}| \rangle$, whenever we consider quantities for the alpha model. Accordingly we determine the scaling exponents by using the exact relation (5.7) for the mixed, third-order structure function, $L^+(l) = \langle |\delta z^-_L||\delta z^+|^2 \rangle$ for MHD and $L^+_s(l) = \langle |\delta z^-_{s_L}|||\delta z^+||^2_\alpha \rangle$ for LAMHD-α. As previously mentioned, from the extended self-similarity hypothesis [4, 5, 66, 68] we expect a better determination of the scaling exponents of the structure functions in this way. Therefore, we determine the relative scaling exponents ξ^f_p from

$$S^f_p(l) \sim [L^+(l)]^{\xi^f_p}. \tag{5.9}$$

In Figure 5.7 L^+ and L^+_s are plotted versus l in log-log. We find distinct from [7] that (5.7) has a range of validity as can be seen in the figure by comparison with the solid line denoting a slope of one. The large scale behavior is accurately preserved. For the LAMHD$-\alpha$ 512^2 solution, $\alpha \approx 7 \cdot 10^{-2}$ and for the LAMHD$-\alpha$ 1024^2 solution, $\alpha \approx 4 \cdot 10^{-2}$. It is only below this length scale that the alpha model departs in behavior from the MHD solution. The 512^2 LAMHD$-\alpha$ results are also linear down to length α. Note that the different multiplicative constant is only due to differing energies between the runs.

For 3D non-conductive flows the Kolmogorov revised similarity hypothesis [49] predicts $\zeta^v_p = \frac{p}{3} + \tau_{p/3}$ where $\tau_{p/3}$ is the so-called anomalous scaling exponent. She and Lévêque [72] have developed a successful turbulence model predicting the values of the anomalous scaling exponents. This model has been extended by IK theory to the MHD

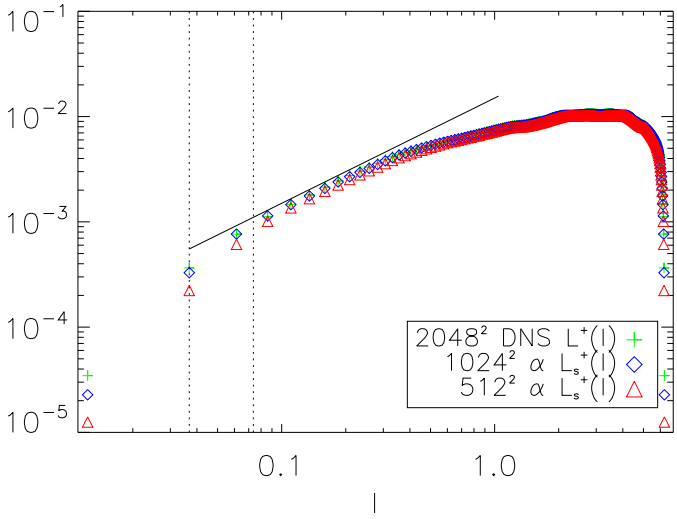

Figure 5.7: Mixed, third-order structure function, $L^+(l)$, versus l, $t = 4$ (runs a-c). 2048^2 DNS are the green pluses, 1024^2 LAMHD$-\alpha$ are the blue diamonds, 512^2 LAMHD$-\alpha$ are red triangles, and a slope of one is the solid line. Vertical lines indicate the lengths α for the 1024^2 and 512^2 simulations.

case by [65, 29] who predict

$$\frac{\xi_p}{\xi_4} = \frac{p}{8} + 1 - \left(\frac{1}{2}\right)^{p/4} \tag{5.10}$$

as the "standard" model from their two-parameter model (hereafter SL). The anomalous scaling results for $\boldsymbol{z}^-$, ξ_p^-, for the freely-decaying runs are shown in Figure 5.8 along with the K41 prediction, $\xi_p = p/3$, the IK prediction, $\xi_p = p/4$, and the SL prediction (5.10). Both alpha model runs preserve the scaling of the MHD simulation up to $p = 6$. For higher orders, the alpha model is observed to be more intermittent than direct solutions, in the sense that they depart more from a self-similar straight line than the DNS. Note that in the LAMHD$-\alpha$ simulations, the amount of statistics is inherently smaller since the spatial resolution is lower (we have $\sim 3 \cdot 10^5$ data values for 512^2 as opposed to $\sim 4 \cdot 10^6$ for 2048^2). In the forced runs, we will find a better fit to (5.10) due to the increased statistics.

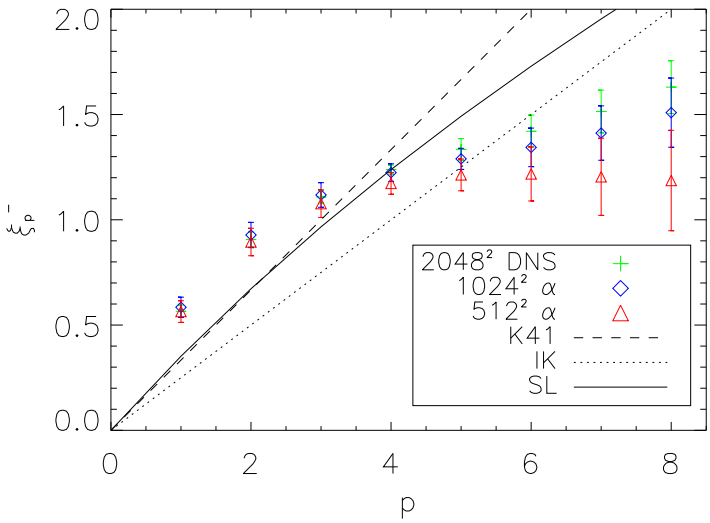

Figure 5.8: Structure function scaling exponents for $\boldsymbol{z}^-$: ξ_p^- versus p at $t = 4$ (runs a-c). Labels are as in Figure 5.7. The K41 prediction is the dashed line, the IK prediction is the dotted line, and SL is the solid line.

For the forced runs, Figure 5.9 shows the mixed, third-order structure functions

L^+ and L_s^+ as functions of l. The solid line indicates the relation $L^+(l) \sim l$. Note that, although the resolution of the forced simulations is smaller than in the previous subsection, the scaling is better due to the larger amount of statistics considered in the forced runs ($\sim 2 \cdot 10^7$ data values for DNS down to $\sim 10^6$ data values for 256^2). The LAMHD$-\alpha$ runs display the same scaling as the MHD simulation, and a departure can be only observed for scales smaller than α (for 256^2, $\alpha \approx .15$ and for 512^2, $\alpha \approx .07$). Note that the results have been scaled by $\langle u^2 b^2 \rangle^{3/4}$. As the average energies of the runs are disparate, this improves the ease of comparison.

The scaling of the fourth-order structure function S_4^- versus L^+ for the Elsässer variable $\boldsymbol{z}^-$ is shown in Figure 5.10. The three simulations show a similar scaling. A line indicates the best fit to the DNS data, $\xi_4^- = 0.98 \pm 0.12$. The anomalous scaling results for the forced run for $\boldsymbol{z}^+$ are shown in Figure 5.11. A good agreement between (5.10) and the results from the DNS can be observed. This differs from the results of [67], whose results for $\xi_p^{\pm}$ do not correspond to the "standard" She and Lévêque model. We note that our results for ξ_p^+ are less intermittent than theirs and that there appears to be a 7% discrepancy between the SL of [67] and (5.10). Furthermore, we find $\xi_4^- \sim 1$ but $\xi_3^+ \sim 1$. This latter result is in opposition to the findings of [67]. Finally, we note their forcing was tailored to maintain at a constant level all Fourier modes with $k = 1$ while our forcing is random with a constant amplitude between $k = 1$ and $k = 2$. The alpha model runs are again observed to be more intermittent for higher orders (above $p = 4$). However, as will be shown in the next figures, the highest order properly captured by the alpha model depends slightly on the quantity studied. It should also be emphasized that at lower resolutions, the statistics of the highest-order structure functions can be insufficient. This can be seen in Figure 5.12 where we down-sampled the resolution of the DNS run to 256^2 and employed the H^1_α norm.[3] Here we see both a reduction in

[3] Comparing scaling exponents by down-sampling and filtering the DNS results is common practice in LES comparisons.

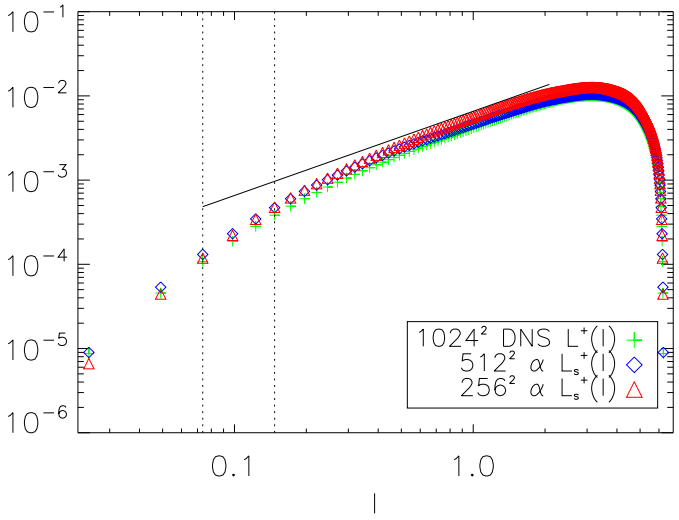

Figure 5.9: Third-order structure function, $L^+(l)$, versus l, for forced turbulence from $t = 50$ up to $t = 150$ (runs d-f). Results are scaled by $\langle u^2 b^2 \rangle^{3/4}$ for easier comparison. 1024^2 MHD solution are the green pluses, 512^2 LAMHD$-\alpha$ are the blue diamonds, 256^2 LAMHD$-\alpha$ are red triangles, and a slope of one is indicated by the solid line. Vertical lines indicate the lengths α for the 512^2 and 256^2 simulations.

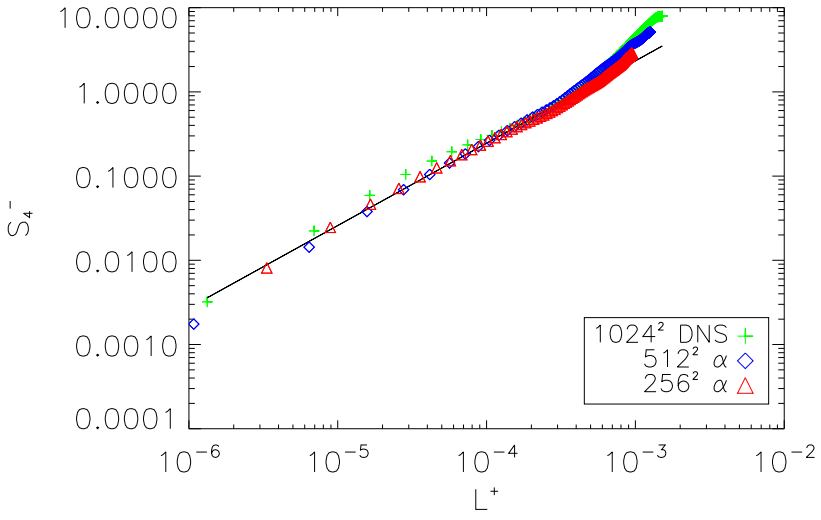

Figure 5.10: Fourth-order structure functions for $\boldsymbol{z}^-$: S_4^- versus L^+, computed from $t = 50$ up to $t = 150$ (runs d-f). Labels are as in Fig. 5.9. The solid line corresponds to the best fit $S_4^- = (L^+)^{\xi_4^-}$, with $\xi_4^- = 0.98 \pm 0.12$.

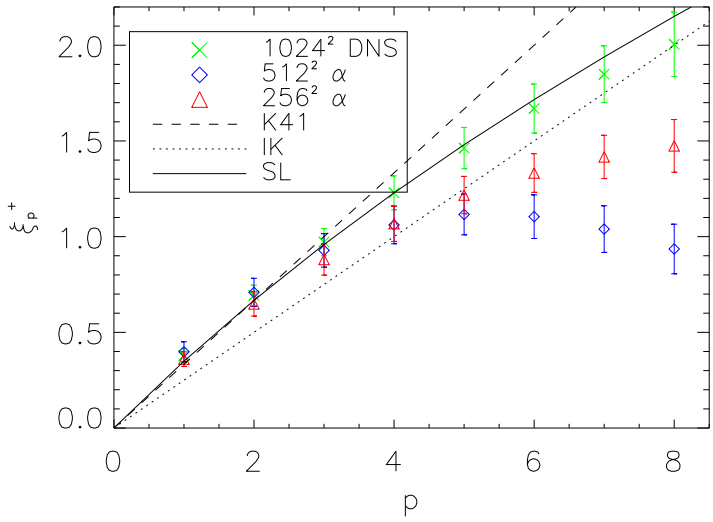

Figure 5.11: Structure function scaling exponent: ξ_p^+ versus p, computed from $t = 50$ up to $t = 150$ for $\boldsymbol{z}^+$ (runs d-f). 1024^2 DNS are the green X's, 512^2 LAMHD$-\alpha$ are the blue diamonds, 256^2 LAMHD$-\alpha$ are the red triangles, and the prediction line labels are as in Figure 5.8.

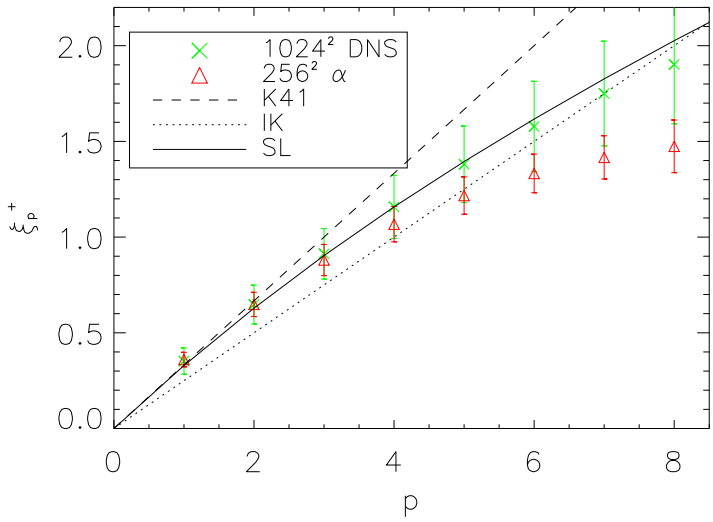

Figure 5.12: Down-sampled-structure-function scaling exponent: ξ_p^+ versus p, computed from $t = 50$ up to $t = 150$ for $\boldsymbol{z}^+$ (runs d and f). Labels are as in Figure 5.11. Here the DNS results were calculated after being down-sampled to a resolution of 256^2 and the H^1_α norm was employed.

the estimates of the highest-order scaling exponents of almost 5% as well as an increase in the uncertainty of the estimate. This suggests that LAMHD$-\alpha$ reproduces MHD intermittency to within the accuracy of the statistics we have gathered. Figure 5.13 shows the scaling exponents for the velocity and magnetic fields. For the DNS the velocity field is more intermittent than the magnetic field. Note that the forcing for the velocity field is greater by design (see §4.4.3.2). The anomalous scaling for the velocity field is matched by LAMHD$-\alpha$ up to and including eighth-order. For the magnetic field, however, the LAMHD$-\alpha$ results are more intermittent above $p = 5$. This result is reminiscent of the results of §4.4.3 where we observed the kinetic energy spectra to be better reproduced than the magnetic. It was suggested that this may be a byproduct of the hyper-viscosity in the LAMHD$-\alpha$ induction equation for the smoothed magnetic field (3.44b). One approach might be to not employ the alpha model for the magnetic field ($\alpha_M = 0$) and another might be to employ another alpha model with a different dissipation term. It must still agree, however, with the more rigorous non-dissipative derivation of [36]. If we remove from the derivation, as shown in §3.4.1, the substitution of a current term for a magnetic term (3.42) prior to our approximations $\boldsymbol{u} \approx \boldsymbol{u}_s$ and $\boldsymbol{b} \approx \boldsymbol{b}_s$ in the induction equation,

$$\partial_t(\boldsymbol{b}_s + \boldsymbol{\delta b}) = \boldsymbol{\nabla} \times ((\boldsymbol{u}_s + \boldsymbol{\delta u}) \times (\boldsymbol{b}_s + \boldsymbol{\delta b})) + \eta\nabla^2(\boldsymbol{b}_s + \boldsymbol{\delta b}). \tag{5.11}$$

This will provide for the LAMHD$-\alpha$ induction equation

$$\partial_t \boldsymbol{b}_s + \boldsymbol{u}_s \cdot \boldsymbol{\nabla} \boldsymbol{b}_s = \boldsymbol{b}_s \cdot \boldsymbol{\nabla} \boldsymbol{u}_s + \eta\nabla^2 \boldsymbol{b}_s \tag{5.12}$$

which does not include a hyper-viscosity and agrees with [36]. This approach would seem plausible as the dissipative term is added to the alpha model *ad hoc* and we should have some freedom in its choice. However, this derivation is a modification of a simplified rederivation which was valid only because it obtained the same result as the full derivation of the alpha model. As such, this new dissipation should first be considered in that framework.

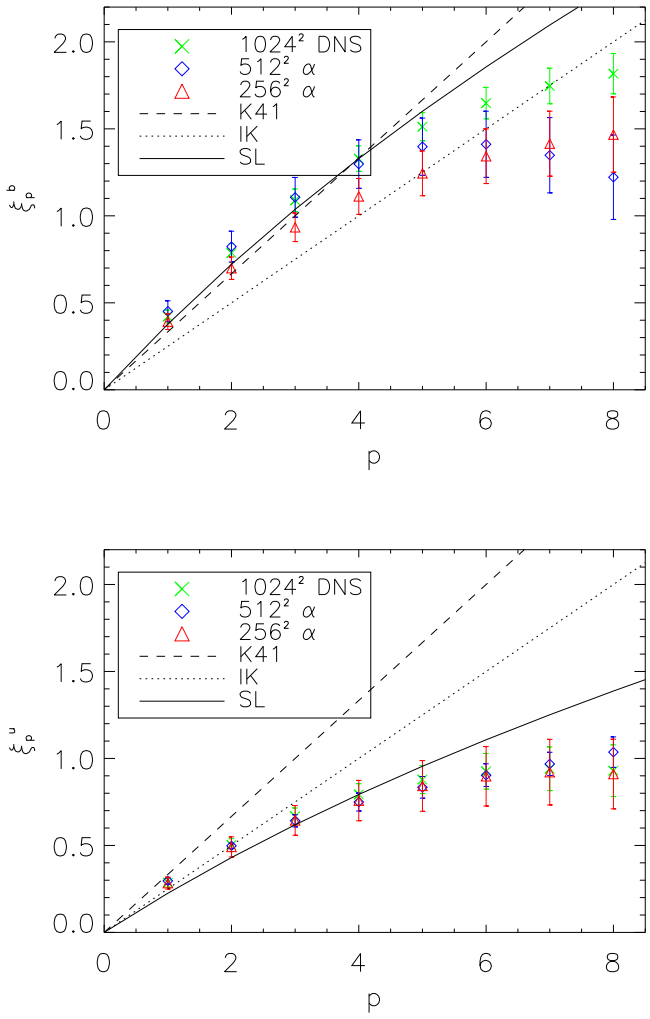

Figure 5.13: Structure function scaling exponents: ξ_p versus p, computed from $t = 50$ up to $t = 150$ (runs d-f). Labels are as in Figure 5.11. Upper panel is for $\boldsymbol{b}$, and lower panel is for $\boldsymbol{u}$.

Chapter 6

Summary, Conclusion, and Outlook

Due to the excitation of small scale fluctuations in fluids by large scale variations, sufficient resolution for high Reynolds number flows can be beyond technological limits. A closure like the Lagrangian-averaged alpha model (*a.k.a.* the alpha model) can reduce the computational burden by reducing the resolution requirements. A review was made of the tests already applied to this model for non-conductive fluids and the evaluation of its intermittency (an essential element of turbulence that signifies a departure from self-similarity) was notably missing. Relying on the fact that, contrary to fluids, the two-dimensional (2D) case in magnetohydrodynamics (MHD) leads to a direct cascade of energy to small scales, the case for studying intermittency of the alpha model with 2D MHD was presented. Finally, numerical simulations were made both for freely decaying and for forced MHD turbulence both at a resolution sufficient to model the dissipation and employing the alpha model at 1/2 and 1/4 resolution.

Any closure should accurately model the effects on the resolved scales of the smaller, unresolved scales. The alpha model does accurately reproduce the large scale-spectra even at 1/4 the resolution of a fully-resolved MHD simulation. For freely decaying MHD turbulence, it also reproduces the time evolution of the total energies and the large-wavelength components of the fields. These results were previously known [55]. We found, however, the magnetic energy spectra to be accurate only for scales larger than $\sim 2\alpha$ while the kinetic energy spectra were accurate for scales larger than $\sim \alpha$.

Comparisons between the alpha model and LES methods for non-conductive flows were reviewed in §3.4. In all cases, the alpha model results were comparable with the best of standard LES models.

We have averaged statistics over 20 turn-over times (and up to $\sim 2 \cdot 10^7$ data values) of a quasi-steady-state to test if the alpha model reproduces intermittent turbulent behavior. The scaling of the third-order structure function is tested and linear scaling with length (down to length α) is observed as predicted by an exact law [66, 68]. We also capture the high-order statistics (up to order 5 or 6)[1] with a gain in speed close to a factor of 16. For non-conductive flows, higher-order statistics for LES models have been tested [13]. Therein, all models tested were highly accurate up to order 4 while the best models had less than 7% error at order 7.[2] For the velocity field, compared to an appropriately down-sampled DNS data set, the alpha model has less than 1.3% error at order 7, but for the magnetic field the error at order 7 can be greater than 20%.

This suggests that, for non-conductive flows at least, the alpha model is comparable to the best of standard LES models for reproducing intermittency as well. For conductive flows, results are quite good if not as encouraging. Large-scale spectra (wavenumbers less than $\frac{1}{2\alpha}$), large-wavelength components of the field, and (in the absence of forcing) time evolution of the energies are well reproduced. Intermittency is reproduced as represented by the high-order statistics (up to order 5 or 6). Two suggestions for further improvements are: (1) not to employ the alpha model for the magnetic field and (2) to alter the derivation of the induction equation for the alpha model. The first suggestion is only useful if the magnetic Prandtl number, $P_M = \frac{\nu}{\eta}$, is much less than one and the magnetic Reynolds number, $R_M = \frac{u_o l_o}{\eta}$, is small as is the case in the laboratory using liquid metals (mercury, sodium, gallium), in the liquid core of the earth, or in the solar convection zone.

[1] Improved statistics (more data) are required to more accurately determine the higher-order statistics.

[2] Note that these tests utilized the statistics from up to $\sim 2 \cdot 10^8$ data values.

Bibliography

[1] D. G. Andrews and M. E. McIntyre. An exact theory of nonlinear waves on a Lagrangian-mean flow. J. Fluid Mech., 89:609–646, 1978.

[2] Gregory L. Baker and Jerry P. Gollub. Chaotic Dynamics: an introduction. Cambridge University Press, Cambridge, 1990.

[3] G. K. Batchelor. An Introduction to Fluid Dynamics. Cambridge University Press, Cambridge, 1967.

[4] R. Benzi, S. Ciliberto, C. Baudet, G. Ruiz Chavarria, and R. Tripiccione. Extended self-similarity in the dissipation range of fully developed turbulence. Europhysics Letters, 24:275–+, November 1993.

[5] R. Benzi, S. Ciliberto, R. Tripiccione, C. Baudet, F. Massaioli, and S. Succi. Extended self-similarity in turbulent flows. "Phys. Rev. E", 48:29–+, July 1993.

[6] H. S. Bhat, R. C. Fetecau, J. E. Marsden, and K. Mohseni. Lagrangian Averaging for Compressible Fluids. 2003. arXiv:physics/0311086.

[7] D. Biskamp and E. Schwarz. On two-dimensional magnetohydrodynamic turbulence. Physics of Plasmas, 8(7):3282–3292, 2001.

[8] Mary L. Boas. Mathematical Methods in the Physical Sciences. John Wiley & Sons, New York, 2nd edition, 1983.

[9] J. W. Brault and O. R. White. The Analysis and Restoration of Astronomical Data via the Fast Fourier Transform. Astron. & Astrophys., 13:169–+, July 1971.

[10] J. M. Burgers. A mathematical model illustrating the theory of turbulence. Advances in Applied Mechanics, 1:171–199, 1948.

[11] Roberto Camassa and Darryl D. Holm. An Integrable Shallow Water Equation with Peaked Solutions. Physical Review Letters, 71(11):1661–1664, 1993.

[12] Claudio Canuto, M. Yousuff Hussaini, Alfio Quarteroni, and Thomas A. Zang. Spectral Methods in Fluid Dynamics. Springer-Verlag, New York, 1988.

[13] S. Cerutti and C. Meneveau. Intermittency and relative scaling of subgrid-scale energy dissipation in isotropic turbulence. Physics of Fluids, 10:928–937, April 1998.

[14] S. Chandrasekhar. The Theory of Axisymmetric Turbulence. Philosophical Transactions of the Royal Society of London. Series A, Mathematical and Physical Sciences, 242(855):557–577, 1950.

[15] S. Chen, C. Foias, D. D. Holm, E. Olson, E. S. Titi, and S. Wynne. Camassa-Holm Equations as a Closure Model for Turbulent Channel and Pipe Flow. Physical Review Letters, 81:5338–5341, December 1998.

[16] S. Chen, C. Foias, D. D. Holm, E. Olson, E. S. Titi, and S. Wynne. A connection between the Camassa-Holm equations and turbulent flows in channels and pipes. Physics of Fluids, 11:2343–2353, August 1999.

[17] S. Chen, C. Foias, D. D. Holm, E. Olson, E. S. Titi, and S. Wynne. The Camassa-Holm equations and turbulence. Physica D Nonlinear Phenomena, 133:49–65, 1999.

[18] S. Chen, D. D. Holm, L. G. Margolin, and R. Zhang. Direct numerical simulations of the Navier-Stokes alpha model. Physica D Nonlinear Phenomena, 133:66–83, 1999.

[19] A. Cheskidov. Turbulent Boundary Layer Equations. C.R. Acad. Ser. I, 334:423, 2002.

[20] Robert Ecke. The Turbulence Problem: An Experimentalist's Perspective. Los Alamos Science, (29):124–141, 2005.

[21] B. R. Fabijonas and D. D. Holm. Mean Effects of Turbulence on Elliptic Instability in Fluids. Physical Review Letters, 90(12):124501–+, March 2003.

[22] C. Foias, D. D. Holm, and E. S. Titi. The Navier-Stokes-alpha model of fluid turbulence. Physica D Nonlinear Phenomena, 152:505–519, May 2001.

[23] Matteo Frigo and Steven G. Johnson. FFTW: An adaptive software architecture for the FFT. In Proc. 1998 IEEE Intl. Conf. Acoustics Speech and Signal Processing, volume 3, pages 1381–1384. IEEE, 1998.

[24] Uriel Frisch. Turbulence, The Legacy of A. N. Kolmogorov. Cambridge University Press, Cambridge, UK, 1995.

[25] D. O. Gómez, P. D. Mininni, and P. Dmitruk. Parallel Simulations in Turbulent MHD". Physica Scripta, 2005.

[26] B. J. Geurts and D. D. Holm. Alpha-Modeling Strategy for LES of Turbulent Mixing. In D. Drikakis and B. J. Geurts, editors, Turbulent Flow Computation, pages 237+, London, 2002. Kluwer Academic Publishers.

[27] B. J. Geurts and D. D. Holm. Leray Simulation of Turbulent Shear Layers. In J. P. Castro and P. E. Hancock, editors, Advances in Turbulence IX: Proceedings of the Ninth European Turbulence Conference, pages 337+, Barcelona, 2002. CIMNE.

[28] David Gottlieb and Steven A. Orszag. Numerical Analysis of Spectral Methods: Theory and Applications. J.W. Arrowsmith Ltd., Bristol, UK, 1977.

[29] R. Grauer, J. Krug, and C. Marliani. Scaling of high-order structure functions in magnetohydrodynamic turbulence. Physics Letters A, 195:335–338, December 1994.

[30] R. J. Greatbatch and B. T. Nadiga. Four Gyre Circulation in a Barotropic Model with Double Gyre Wind Forcing. J. Phys. Oceanogr., 30:1461, 2000.

[31] Ronald B. Guenther and John W. Lee. Partial Differential Equations of Mathematical Physics and Integral Equations. Dover Publications, Inc., New York, 1996.

[32] Stephen Hawking, editor. Stephen Hawking's A brief history of time : a reader's companion. Bantam Books, New York, 1992.

[33] D. D. Holm. Fluctuation Effects on 3D Lagrangian Mean and Eulerian Mean Fluid Motion. Physica D Nonlinear Phenomena, 133:215+, 1999.

[34] D. D. Holm. Averaged Lagrangians and the mean effects of fluctuations in ideal fluid dynamics. Physica D Nonlinear Phenomena, 170:253–286, September 2002.

[35] D. D. Holm. Kármán Howarth theorem for the Lagrangian-averaged Navier Stokes alpha model of turbulence. Journal of Fluid Mechanics, 467:205–214, September 2002.

[36] D. D. Holm. Lagrangian averages, averaged Lagrangians, and the mean effects of fluctuations in fluid dynamics. Chaos, 12:518–530, 2002.

[37] D. D. Holm and R. Kerr. Transient Vortex Events in the Initial Value Problem for Turbulence. Physical Review Letters, 88(24):244501–+, June 2002.

[38] D. D. Holm, J. E. Marsden, and T. S. Ratiu. Euler-Poincaré Models of Ideal Fluids with Nonlinear Dispersion. Physical Review Letters, 80:4173–4176, May 1998.

[39] D. D. Holm, J. E. Marsden, and T. S. Ratiu. The Euler-Poincaré Equations and Semidirect Products with Applications to Continuum Theories. Adv. in Math., 137:1–81, 1998.

[40] D. D. Holm and B. Nadiga. Modeling Mesoscale Turbulence in the Barotropic Double Gyre Circulation. J. Phys. Oceanogr., 33:2355, 2003.

[41] D. D. Holm, V. Putkaradze, P. D. Weidman, and B. A. Wingate. Boundary Effects on Exact Solutions of the Lagrangian-Averaged Navier-Stokes-α Equations. J. Stat. Phys., 113:841, 2003.

[42] D. D. Holm and B. A. Wingate. Baroclinic Instability for LANS-Alpha Models. J. Phys. Oceanogr., 2004. to appear.

[43] Darryl D. Holm. Taylor's Hypothesis, Hamilton's Principle, and the LANS-α Model for Computing Turbulence. Los Alamos Science, (29):172–180, 2005.

[44] Darryl D. Holm, Chris Jeffery, Susan Kurien, Daniel Livescu, Mark A. Taylor, and Beth A. Wingate. The LANS-α Model for Computing Turbulence: Origins, Results, and Open Problems. Los Alamos Science, (29):152–171, 2005.

[45] P. S. Iroshnikov. Turbulence of a Conducting Fluid in a Strong Magnetic Field. Soviet Astronomy, 7:566–+, February 1964.

[46] A. N. Kolmogorov. Dissipation of energy in locally isotropic turbulence. Dokl. Akad. Nauk SSSR, 32:16–18, 1941.

[47] A. N. Kolmogorov. On degeneration (decay) of isotropic turbulence in an incompressible viscous liquid. Dokl. Akad. Nauk SSSR, 31:538–540, 1941.

[48] A. N. Kolmogorov. The local structure of turbulence in incompressible viscous fluid for very large Reynolds number. Dokl. Akad. Nauk SSSR, 30:9–13, 1941.

[49] A. N. Kolmogorov. A refinement of previous hypotheses concerning the local structure of turbulence in a viscous incompressible fluid at high Reynolds number. Journal of Fluid Mechanics, 13:82–85, 1962.

[50] R. H. Kraichnan. Inertial-range spectrum of hydromagnetic turbulence. Physics of Fluids, 8:1385–1387, 1965.

[51] Susan Kurien and Mark A. Taylor. Direct Numerical Simulations of Turbulence: Data Generation and Statistical Analysis. Los Alamos Science, (29):142–151, 2005.

[52] E. Lévêque and C. R. Koudella. Finite-Mode Spectral Model of Homogeneous and Isotropic Navier-Stokes Turbulence: A Rapidly Depleted Energy Cascade. Physical Review Letters, 86:4033–4036, April 2001.

[53] Marcel Lesieur. Turbulence in Fluids. Kluwer Academic Publishers, Dordrecht, 3rd edition, 2000.

[54] P. D. Mininni, D. C. Montgomery, and A. Pouquet. Numerical solutions of the three-dimensional magnetohydrodynamic α model. "Phys. Rev. E", 71(4):046304–+, April 2005.

[55] P. D. Mininni, D. C. Montgomery, and A. G. Pouquet. A numerical study of the alpha model for two-dimensional magnetohydrodynamic turbulent flows. Physics of Fluids, 17:5112–+, March 2005.

[56] P. D. Mininni, J. D. Pietarila Graham, D. D. Holm, and A. Pouquet. Inertial Range Scaling, Kármán-Howarth Theorem and Intermittency for Forced and Decaying Lagrangian Averaged MHD in 2D. 2005. in preparation.

[57] K. Mohseni, B. Kosović, S. Shkoller, and J. E. Marsden. Numerical simulations of the Lagrangian averaged Navier-Stokes equations for homogeneous isotropic turbulence. Physics of Fluids, 15:524–544, February 2003.

[58] K. Mohseni, S. Shkoller, B. Kosovic, and J. Marsden. Numerical simulations of the Lagrangian Averaged Navier-Stokes (LANS) equations for forced isotropic homogeneous turbulence. In Proceedings of the 15th AIAA Computational Fluid Dynamics Conference, Anaheim, CA, June 2001. AAIA paper 2001-2645.

[59] K. Mohseni, S. Shkoller, B. Kosovic, J. Marsden, D. Carati, A. Wray, and B. Rogallo. Numerical simulations of homogeneous turbulence using Lagrangian averaged Navier-Stokes equations. In Proceedings of the 2000 Summer Program, pages 271–283. NASA Ames/Stanford University, 2000.

[60] D. C. Montgomery and A. Pouquet. An alternative interpretation for the Holm "alpha model". Physics of Fluids, 14(9):3365–3366, 2002.

[61] Gordon E. Moore. Cramming more components into integrated circuits. Electronics, 38(8), 1965.

[62] R. H. Morf, S. A. Orszag, and U. Frisch. Spontaneous singularity in three-dimensional, inviscid, incompressible flow. Physical Review Letters, 44:572–575, March 1980.

[63] Hans L. Pécseli. Selected Topics in Plasma Physics. Universitetet i Oslo, compendium for course, 2003.

[64] Jonathan D. Pietarila Graham, Pablo D. Mininni, and Annick Pouquet. Cancellation exponent and multifractal structure in Lagrangian averaged magnetohydrodynamics. 2005. in preparation.

[65] H. Politano and A. Pouquet. Model of intermittency in magnetohydrodynamic turbulence. "Phys. Rev. E", 52:636–641, July 1995.

[66] H. Politano and A. Pouquet. von Kármán-Howarth equation for magnetohydrodynamics and its consequences on third-order longitudinal structure and correlation functions. Physical Review E, 57(1):R21–R24, 1998.

[67] H. Politano, A. Pouquet, and V. Carbone. Determination of anomalous exponents of structure functions in two-dimensional magnetohydrodynamic turbulence. Europhysics Letters, 43:516–521, September 1998.

[68] Hélène Politano and Annick Pouquet. Dynamical length scales for turbulent magnetized flows. Geophysical Research Letters, 25(3):273–276, 1998.

[69] Y. Ponty, P. D. Mininni, D. C. Montgomery, J.-F. Pinton, H. Politano, and A. Pouquet. Numerical Study of Dynamo Action at Low Magnetic Prandtl Numbers. Physical Review Letters, 94(16):164502–+, April 2005.

[70] V. Putkaradze and P. Weidman. Turbulent wake solutions of the Prandtl α equations. "Phys. Rev. E", 67(3):036304–+, March 2003.

[71] Lewis Fry Richardson. Weather prediction by numerical process. Dover Publications, Inc., New York, 1965. out of print.

[72] Z. She and E. Leveque. Universal scaling laws in fully developed turbulence. Physical Review Letters, 72:336–339, January 1994.

[73] J. C. Sprott. Simplest dissipative chaotic flow. Physics Letters A, 228:271–274, February 1997.

[74] James Stewart. Calculus. Brooks/Cole Publishing Company, Pacific Grove, California, 1987.

[75] P. Tabeling and O. Cardoso, editors. Turbulence, A Tentative Dictionary, volume 341 of B, New York, 1994. NATO ASI, Plenum Press.

[76] G. I. Taylor. The Spectrum of Turbulence. In Proceedings of the Royal Society of London, volume A164, 1938.

[77] G. I. Taylor and A. E. Green. Mechanism of the Production of Small Eddies from Large Ones. In Proceedings of the Royal Society of London, volume A158, 1937.

[78] Jans Trulsen. Radiation. Universitetet i Oslo, compendium for course, 2003.

[79] Hongwu Zhao and Kamran Mohseni. A Dynamic model for the Lagrangian Averaged Navier-Stokes-α Equations. 2004. arXiv:physics/0408113.

Appendix A

Derivations

A.1 Navier-Stokes

A.1.1 Derivation of the Vorticity Equation

The Navier-Stokes equations are given by:

$$\partial_t \boldsymbol{u} + \boldsymbol{u} \cdot \boldsymbol{\nabla} \boldsymbol{u} = -\boldsymbol{\nabla} p + \mathcal{F} + \nu \nabla^2 \boldsymbol{u} \tag{A.1}$$

$$\boldsymbol{\nabla} \cdot \boldsymbol{u} = 0. \tag{A.2}$$

Now, defining the vorticity with

$$\boldsymbol{w} \equiv \boldsymbol{\nabla} \times \boldsymbol{u} \tag{A.3}$$

and taking the curl of (A.1) will give us the vorticity equation. The curl is a linear operator:

$$\boldsymbol{\nabla} \times \partial_t \boldsymbol{u} + \boldsymbol{\nabla} \times (\boldsymbol{u} \cdot \boldsymbol{\nabla} \boldsymbol{u}) = -\boldsymbol{\nabla} \times \boldsymbol{\nabla} p + \boldsymbol{\nabla} \times \mathcal{F} + \boldsymbol{\nabla} \times \nu \nabla^2 \boldsymbol{u} \tag{A.4}$$

For sufficiently continuous velocity fields,

$$\boldsymbol{\nabla} \times \partial_t \boldsymbol{u} = \partial_t \boldsymbol{\nabla} \times \boldsymbol{u} = \partial_t \boldsymbol{w} \tag{A.5}$$

and

$$\boldsymbol{\nabla} \times \nabla^2 \boldsymbol{u} = \nabla^2 \boldsymbol{\nabla} \times \boldsymbol{u} = \nabla^2 \boldsymbol{w}. \tag{A.6}$$

And, the curl of a gradient is zero,

$$\boldsymbol{\nabla} \times \boldsymbol{\nabla} p = 0, \tag{A.7}$$

which, through a familiar identity, can be intuitively understood as the statement that the up-hill direction of a scalar field cannot circle around any point. Start at any point close by and circle the first point back to where you started. If there was a positive (or negative) curl, after going full circle the scalar field should have a higher (or lower) value than you began with. This violates the assumption of single-valuedness.

This leaves us with the curl of the nonlinear term. Using the velocity cross vorticity identity, $\boldsymbol{u} \times (\boldsymbol{\nabla} \times \boldsymbol{u}) = \frac{1}{2}\boldsymbol{\nabla} u^2 - \boldsymbol{u} \cdot \boldsymbol{\nabla}\boldsymbol{u}$:

$$\boldsymbol{\nabla}\times(\boldsymbol{u}\cdot\boldsymbol{\nabla}\boldsymbol{u}) = \boldsymbol{\nabla}\times(\frac{1}{2}\boldsymbol{\nabla}u^2-\boldsymbol{u}\times\boldsymbol{w}) = -\boldsymbol{\nabla}\times\boldsymbol{u}\times\boldsymbol{w} = -(\boldsymbol{w}\cdot\boldsymbol{\nabla})\boldsymbol{u}+\boldsymbol{w}\boldsymbol{\nabla}\cdot\boldsymbol{u}-\boldsymbol{u}\boldsymbol{\nabla}\cdot\boldsymbol{w}+(\boldsymbol{u}\cdot\boldsymbol{\nabla})\boldsymbol{w}. \tag{A.8}$$

Here we used again that the curl of a gradient is zero and a familiar vector identity for the curl of a cross product. Now using that the flow is incompressible (A.2) and that the divergence of a curl is zero, which holds for sufficiently continuous functions,[1] we find

$$\boldsymbol{\nabla} \times (\boldsymbol{u} \cdot \boldsymbol{\nabla}\boldsymbol{u}) = -(\boldsymbol{w} \cdot \boldsymbol{\nabla})\boldsymbol{u} + (\boldsymbol{u} \cdot \boldsymbol{\nabla})\boldsymbol{w}. \tag{A.9}$$

Finally, we obtain the vorticity equation by combining (A.4 - A.7) and (A.9):

$$\partial_t \boldsymbol{w} + \boldsymbol{u} \cdot \boldsymbol{\nabla}\boldsymbol{w} = \boldsymbol{w} \cdot \boldsymbol{\nabla}\boldsymbol{u} + \boldsymbol{\nabla} \times \mathcal{F} + \nu\nabla^2\boldsymbol{w}. \tag{A.10}$$

A.1.2 Elimination of the Pressure Term

This derivation is from [24]. Only explanations between the steps have been added.

Rewriting the Navier-Stokes equations (A.1) and (A.2) in summation notation:

$$\partial_t u_i + u_j\partial_j u_i = -\partial_i p + \nu\partial_{jj} u_i \tag{A.11}$$

$$\partial_i u_i = 0. \tag{A.12}$$

[1] For an infinitesimal cube, the rotation of the vector field at the top and the bottom (or from opposite sides) must be the same, but the normal vectors are anti-parallel and the contributions to the divergence cancel.

Now, taking the divergence of (A.11);

$$\partial_i \partial_t u_i + \partial_i (u_j \partial_j u_i) = -\partial_{ii} p + \nu \partial_i \partial_{jj} u_i. \tag{A.13}$$

For sufficiently continuous velocity fields,

$$\partial_i \partial_t u_i = \partial_t \partial_i u_i = \partial_t 0 = 0, \tag{A.14}$$

$$\nu \partial_i \partial_{jj} u_i = \nu \partial_{jj} \partial_i u_i = \nu \partial_{jj} 0 = 0, \tag{A.15}$$

and

$$\partial_{ij}(u_i u_j) = \partial_i (u_i \partial_j u_j + u_j \partial_j u_i) = \partial_i (u_i \cdot 0 + u_j \partial_j u_i) = \partial_i (u_j \partial_j u_i) \tag{A.16}$$

where we have made repeated use of the incompressibility condition (A.12). Combining (A.13 - A.16) we find that

$$\nabla^2 p = \sigma \equiv -\partial_{ij}(u_i u_j). \tag{A.17}$$

This is a Poisson equation and its solution is physically non-local which we express with the non-local operator ∇^{-2}:

$$p = \nabla^{-2} \sigma. \tag{A.18}$$

Substituting (A.18) back into Navier-Stokes (A.11), we find

$$\partial_t u_i + u_j \partial_j u_i - \partial_i \nabla^{-2} \partial_{lj}(u_j u_l) = \nu \nabla^2 u_i \tag{A.19}$$

and, as ∇^{-2} and ∂_l commute (at least in Fourier space), we find:

$$\partial_t u_i + \partial_j (u_j u_i) - \partial_{il} \nabla^{-2} \partial_j (u_j u_l) = \nu \nabla^2 u_i \tag{A.20}$$

where we used a portion of (A.16). Finally, with a judicious use of the δ-function, we arrive at the result of [24]:

$$\partial_t u_i + (\delta_{il} - \partial_{il} \nabla^{-2}) \partial_j (u_j u_l) = \nu \nabla^2 u_i. \tag{A.21}$$

A.2 Burgers Equation

A.2.1 Calculation of Dissipation Rate

Burgers equation is given by

$$\partial_t u + u\partial_y u = \nu \partial^2_{yy} u. \tag{A.22}$$

After multiplying by u and integrating with respect to y we have

$$\int u\partial_t u dy + \int u^2 \partial_y u dy = \nu \int u \partial^2_{yy} u dy. \tag{A.23}$$

Realizing that $\frac{1}{2}\partial_t(u^2) = u\partial_t u$, we find the time rate of change of the total energy in the system,

$$\int u\partial_t u dy = \int \frac{1}{2}\partial_t(u^2) dy = \frac{d}{dt}\int \frac{1}{2} u^2 dy. \tag{A.24}$$

Using integration by parts, *a.k.a* the product rule,

$$\partial_x(uv) = u\partial_x v + v\partial_x u \rightarrow u\partial_x v = \partial_x(uv) - v\partial_x u, \tag{A.25}$$

we find

$$u^2\partial_y u = \partial_y(u^3) - u\partial_y(u^2) = \partial_y(u^3) - 2u^2\partial_y u, \tag{A.26}$$

or

$$u^2\partial_y u = \frac{1}{3}\partial_y(u^3). \tag{A.27}$$

Therefore,

$$\int_a^b u^2\partial_y u dy = \int_a^b \frac{1}{3}\partial_y(u^3) dy = \frac{1}{3}u^3|_a^b. \tag{A.28}$$

For three circumstances of interest, this term will go to zero:

(1) periodic boundary conditions ($u^3(b) = u^3(a)$)

(2) for an infinite domain with $lim_{x\rightarrow\pm\infty} u = 0$

(3) for $u = 0$ on the boundaries.

Using integration by parts again we have

$$u\partial_{yy}^2 u = u\partial_y(\partial_y u) = \partial_y(u\partial_y u) - (\partial_y u)(\partial_y u). \tag{A.29}$$

Then,

$$\nu \int u\partial_{yy}^2 u dy = \nu \int \partial_y(u\partial_y u)dy - \nu \int (\partial_y u)^2 dy = \nu u\partial_y u|_a^b - \nu \int (\partial_y u)^2 dy. \tag{A.30}$$

For the same three circumstances as $u^3|_a^b$, $u\partial_y u|_a^b$ will go to zero. Finally, we calculate the dissipation rate of kinetic energy by substituting (A.24), (A.28), and (A.30) into (A.23) to find

$$\frac{d}{dt}\int \frac{1}{2}u^2 dy = -\nu \int (\partial_y u)^2 dy. \tag{A.31}$$

A.2.2 Uniqueness Proof

Let $v(y,t)$ and $w(y,t)$ each be twice-differentiable-in-y solutions of

- Burgers equation: (A.22)
- with periodic boundary conditions: $u(0,t) = u(L,t)$
- $u(y,0) = U(y)\ \forall\ 0 \le y \le L$.

Then, $v(y,t) \equiv w(y,t)\ \forall\ 0 \le y \le L,\ t > 0$.

Proof.

Define $\sigma(y,t) \equiv v(y,t) - w(y,t)$. Then,

- $\partial_t \sigma + \sigma\partial_y \sigma = \nu\partial_{yy}^2 \sigma$
- $\sigma(0,t) = \sigma(L,t)$
- $\sigma(y,0) = 0\ \forall\ 0 \le y \le L$.

Define $E(t) = \int_0^L \frac{1}{2}\sigma^2 dy$ and note that

- $E(t) \ge 0$

- $E(0) = 0$.

From the dissipation rate (A.31) we have

$$\frac{dE}{dt} = -\nu \int_0^L (\partial_y u)^2 dy \leq 0. \tag{A.32}$$

Therefore, $E(t)$ is a non-negative decreasing function of time that started at zero and $E(t) = 0 \; \forall \; t \geq 0$ is the only solution.

$$\int_0^L \frac{1}{2} u^2 dy = 0 \; \forall \; t \geq 0 \tag{A.33}$$

Now prove $\sigma(y,t) \equiv 0$.

Proof.

(1) Assume not: $\exists \; (y^*, t^*) \ni \; \sigma(y^*, t^*) > 0$

- negative would work similarly

(2) since σ is twice differentiable in y, σ is continuous:

$\exists \; \epsilon \ni \sigma(y, t^*) > \frac{\sigma(y^*,t^*)}{2} \; \forall \; |y - y^*| < \epsilon$

(3) $E(t^*) = 0 = \int_0^L \frac{1}{2}\sigma^2 dy$

$= \int_0^{y^*-\epsilon} \frac{1}{2}\sigma^2 dy + \int_{y^*-\epsilon}^{y^*+\epsilon} \frac{1}{2}\sigma^2 dy + \int_{y^*+\epsilon}^{L} \frac{1}{2}\sigma^2 dy \geq \int_{y^*-\epsilon}^{y^*+\epsilon} \frac{1}{2}\sigma^2 dy$

$\geq (2\epsilon) \left(\frac{\sigma(y^*,t^*)}{2} \right)^2 > 0$

(4) Contradiction. Therefore, $\sigma \equiv 0 \; \forall \; 0 \leq y \leq L, \; t > 0$.

□

Finally, $v(y,t) \equiv w(y,t) \; \forall \; 0 \leq y \leq L, \; t > 0$. □

A.3 Parseval's Theorem

We take the Fourier transform to be[2]

$$\mathcal{F}[f(x)] \equiv \hat{f}(k) = \int_{-\infty}^{\infty} f(x)e^{-ikx}dx$$

and the inverse Fourier transform to be

$$\mathcal{F}^{-1}[\hat{f}(k)] = \frac{1}{2\pi}\int_{-\infty}^{\infty} \hat{f}(k)e^{ikx}dk.$$

Then, Parseval's theorem states that if $f(x)$ and $g(x)$ are continuous, real-valued functions satisfying either the conditions of the Riemann-Lebesque lemma or of the Dirichlet theorem, then

$$\int_{-\infty}^{\infty} f(x)g(x)dx = \frac{1}{2\pi}\int_{-\infty}^{\infty} \hat{f}(k)\hat{g}^*(k)dk. \tag{A.34}$$

Proof.

$$f(x)g(x) = \frac{1}{2\pi}\int_{-\infty}^{\infty} \hat{f}(k)e^{ikx}dk \cdot \frac{1}{2\pi}\int_{-\infty}^{\infty} \hat{g}(k')e^{ik'x}dk'$$

$$\int_{-\infty}^{\infty} f(x)g(x)dx = \int_{-\infty}^{\infty} \frac{1}{2\pi}\int_{-\infty}^{\infty} \hat{f}(k)e^{ikx}dk \cdot \frac{1}{2\pi}\int_{-\infty}^{\infty} \hat{g}(k')e^{ik'x}dk'dx$$

But,

$$\frac{1}{2\pi}\int_{-\infty}^{\infty} e^{i(k+k')x}dx = \delta(k+k')$$

and

$$\int_{-\infty}^{\infty} f(x)g(x)dx = \frac{1}{2\pi}\int_{-\infty}^{\infty} dk \int_{-\infty}^{\infty} dk' \hat{f}(k)\hat{g}(k')\delta(k+k')$$
$$= \frac{1}{2\pi}\int_{-\infty}^{\infty} \hat{f}(k)\hat{g}(-k)dk.$$

Since, $g(x)$ is a real-valued function, $\hat{g}(-k) = \hat{g}^*(k)$. (A.34) follows. □

If, in addition to the above conditions, we have $f(x) = g(x)$, we find that

$$\int_{-\infty}^{\infty} f^2dx = \frac{1}{2\pi}\int_{0}^{\infty} \hat{f}\hat{f}^*dk + \frac{1}{2\pi}\int_{0}^{\infty} \hat{f}^*\hat{f}dk$$
$$\int_{-\infty}^{\infty} f^2dx = \frac{1}{\pi}\int_{0}^{\infty} \hat{f}^*\hat{f}dk. \tag{A.35}$$

[2] Other normalizations are possible.

Appendix B

Summary of Notations

In tensor notation, repeated subscript denotes summation and a single subscript represents a vector. So, the dot product can be represented by

$$\boldsymbol{a} \cdot \boldsymbol{b} = a_1 b_1 + a_2 b_2 + a_3 b_3 = \sum_{i=1}^{3} a_i b_i = a_i b_i, \tag{B.1}$$

and the gradient by

$$\boldsymbol{\nabla}\phi = \partial_i \phi. \tag{B.2}$$

The Kronecker delta is defined as usual;

$$\delta_{ij} \equiv \begin{cases} 0, & i \neq j \\ 1, & i = j. \end{cases} \tag{B.3}$$

A useful function is:

$$\epsilon_{ijl} \equiv \begin{cases} 1, & (i,j,l)\ cyclic \\ -1, & not\ cyclic \\ 0, & if\ any\ two\ indices\ are\ equal. \end{cases} \tag{B.4}$$

We can use this to represent the cross product and the curl,

$$(\boldsymbol{a} \times \boldsymbol{b})_i = \epsilon_{ijl} a_j b_l, \tag{B.5}$$

$$(\boldsymbol{\nabla} \times \boldsymbol{u})_i = \epsilon_{ijl} \partial_j u_l. \tag{B.6}$$

One last useful identity is

$$\epsilon_{ijl}\epsilon_{imn} = \delta_{jm}\delta_{ln} - \delta_{jn}\delta_{lm}. \tag{B.7}$$